Novel nanoarchitectures for electrochemical biosensing

Author: Michelle M. Archibald

Boston College

The Graduate School of Arts and Sciences

Department of Biology

NOVEL NANOARCHITECTURES FOR ELECTROCHEMICAL BIOSENSING

A Dissertation

by

MICHELLE M. ARCHIBALD

submitted in partial fulfillment of the requirements

for the degree of

Doctor of Philosophy

May 2016

Novel Nanoarchitectures for Electrochemical Biosensing

Michelle M. Archibald

Advisor: Thomas C. Chiles, Ph.D.

Abstract

Sensitive, real-time detection of biomarkers is of critical importance for rapid and accurate diagnosis of disease for point-of-care (POC) technologies. Current methods, while sensitive, do not adequately allow for POC applications due to several limitations, including complex instrumentation, high reagent consumption, and cost. We have investigated two novel nanoarchitectures, the nanocoax and the nanodendrite, as electrochemical biosensors towards the POC detection of infectious disease biomarkers to overcome these limitations. The nanocoax architecture is composed of vertically-oriented, nanoscale coaxial electrodes, with coax cores and shields serving as integrated working and counter electrodes, respectively. The dendritic structure consists of metallic nanocrystals extending from the working electrode, increasing sensor surface area.

Nanocoaxial- and nanodendritic-based electrochemical sensors were fabricated and developed for the detection of bacterial toxins using an electrochemical enzyme-linked immunosorbent assay (ELISA) and differential pulse voltammetry (DPV). Proof-of-concept was demonstrated for the detection of cholera toxin (CT). Both nanoarchitectures exhibited levels of sensitivity that are comparable to the standard optical ELISA used widely in clinical applications. In addition to matching the detection profile of the standard ELISA, these electrochemical nanosensors provide a simple electrochemical readout and a miniaturized platform with

multiplexing capabilities toward POC implementation. Further development as suggested in this thesis may lead to increases in sensitivity, enhancing the attractiveness of the architectures for future POC devices.

Acknowledgments

First, I would like to thank my advisor Dr. Thomas C. Chiles for his support and guidance over the past years, and for giving me freedom and independence in my research projects. I would also like to thank my collaborator and committee member Dr. Michael J. Naughton who has provided much guidance over the past years. Thank you to my other committee members Dr. Thomas Seyfried, Dr. John Christianson, and Dr. Welkin Johnson.

Thank you to all of the Chiles' lab members, past and present, for your help and support. I would like to especially thank Shannon Heyse. Although our projects were in completely different fields, she always listened about failed experiments and gave me continual encouragement. Thank you to all of the Naughton lab members, past and present. I would especially like to thank Dr. Binod Rizal with whom I did a majority of my work and who fabricated many samples for me. I would also like to thank Nathan Nesbitt for his help with dendrite fabrication.

I'd like to thank Steve Shepherd for all of his help in the clean room; Steve was always generous with his time and was a huge help. I would like to thank Peter Marino whose genuine help constantly extended beyond the academic realm. I cannot thank him enough. Boston College is lucky to have him.

I would like to thank my friends that I have met during my time at Boston College, especially Kimberly Regna Miller who was a great support and a great friend through the ups and downs of graduate school. Thank you to my non-BC friends - I must especially

thank Catie Crampton who always had a listening ear and treated me to amazing home-cooked meals after bad days.

Most importantly, I want to thank my family: my mom Roxanne, my faja Peter, and my brother Seann. I couldn't have done this without you.

This dissertation is dedicated to my parents:

Roxanne and Peter Archibald

Abbreviations

Ab	antibody
ALD	atomic layer deposition
ALP	alkaline phosphatase
4-AP	4-aminophenol
BSA	bovine serum albumin
C_{dl}	double layer capacitance
CE	counter electrode
CEA	carcinoembryonic antigen
CNT	carbon nanotube
CT	cholera toxin
DENA	directed electrochemical nanowire assembly
DPV	differential pulse voltammetry
ECC	extended core coax
EDTA	ethylenediaminetetraacetic acid
ELISA	enzyme-linked immunosorbent assay
FCA	ferrocenecarboxylic acid
FDTS	1H,1H,2H,2H-perfluorodecyltrichlorosilane
FIB	focused ion beam
FITC	fluorescein isothiocyanate
$HAuCl_4$	chloroauric acid
HBV	hepatitis B virus
HCV	hepatitis C virus

HDMS	hexamethyldisilazane
HRP	horse radish peroxidase
I_p	peak current
IL-2	interleukin-2
IL-6	interleukin-6
IPA	isopropanol
J	current density
LC-MS	liquid chromatography-mass spectrometry
LFA	lateral flow assay
LOD	limit of detection
NIL	nanoimprint lithography
pAPP	p-aminophenylphosphate
PCR	polymerase chain reaction
PBS	phosphate buffered saline
PBST	phosphate buffered saline with tween-20
PDMS	polydimethylsiloxane
POC	point-of-care
PSA	prostate-specific antigen
QD	quantum dot
R1	replicate 1
R2	replicate 2
RE	reference electrode
R_s	solution resistance

SDS	sodium dodecyl sulfate
SiNP	silicon nanopillar
SEM	scanning electron microscopy
SWCNT	single-walled carbon nanotube
SWV	square wave voltammetry
TBS	tris buffered saline
TBST	tris buffered saline with tween-20
UME	ultramicroelectrode
VOC	volatile organic compound
WE	working electrode

Table of Contents

List of Figures

Chapter 1 Introduction

Chapter 2 Material and Methods

Chapter 3 Nanocoax

Appendix I Molecular imprint

List of Tables

Chapter 4 Dendrites

Chapter 1.

Introduction

1.1 Point-of-care diagnostics for infectious disease

Highly specific and sensitive diagnostic tools for clinically relevant disease biomarkers are critical in enabling accurate disease detection and monitoring. In spite of significant efforts, there currently remains an unmet need for such diagnostic tools in the form of point-of-care (POC) technologies, which would allow for on-site, real-time patient testing and diagnosis. The importance of such POC diagnostic development is highlighted by a recent rise in several global epidemics. Emerging and re-emerging infectious diseases constitute some of the most significant public health challenges facing the global community. For example, cholera continues to inflict high rates of mortality in resource limited areas[1,2], and Ebola outbreaks with extremely high instances of fatality present a challenge to even the most sophisticated medical establishments[3]. In addition, malaria, tuberculosis, and HIV constitute the majority of infectious-disease burdens, which disproportionately afflict the developing world[4]. Due to globalization and international travel, there is now an additional increased threat of an accelerated epidemic-to-pandemic transition of these communicable diseases[5,6]. Therefore, accurate and timely confirmation of disease is essential in the implementation of preventative and protective public health measures. Robust POC technologies would facilitate better prevention and earlier response, enabling accurate diagnosis and proper subsequent treatment.

Conventional "gold standard" techniques in clinical infectious disease diagnostics include enzyme-linked immunosorbent assays (ELISA) and polymerase chain reaction (PCR)[7–9] Briefly, these diagnostic methods detect a target disease biomarker, specifically any molecule (e.g. protein, DNA, RNA, whole virus, toxin) whose expression level or

presence is indicative of disease state. The ELISA is the most commonly-used method for clinical protein detection for a host of human diseases, including cancer biomarker detection and bacterial toxin detection[10–12]. However, cost and the need for complex optical instrumentation required for an ELISA measurement limit its potential for deployment in POC settings. Microarrays and liquid chromatography-mass spectrometry based (LC-MS-based) proteomics provide alternative platforms to ELISA-based methods. While both technologies are highly sensitive and allow for multiplexing, they also require complex instrumentation, specialized consumables, and a high skill set for users[13–16]. Recently, PCR has been adapted for infectious disease detection[17,18]. While PCR is a highly sensitive technique and can differentiate between multiple pathogens, the requirement of skilled technicians, risk of contamination, and prolonged analysis times prevents its use in POC settings.

The aforementioned diagnostic assays fail to provide critically-needed capabilities required for POC technologies, such as real-time, cost-effective detection of infectious disease markers, and device portability. Rapid turnaround time from test to diagnosis would allow for on-site treatment of the patient and is crucial in the prevention of disease outbreak[19]. In order to be a viable option in low resource settings, POC devices must be low-cost and easily portable to a potentially laboratory-free test site[20,21]. As mentioned above, many conventional diagnostics require complex instrumentation and sophisticated reagents; a portable POC device would not be able to accommodate such equipment. A lack of trained staff as well as poor laboratory infrastructure in these areas emphasize the need for a simple, transportable POC device that can be utilized without extensive

specialized training[22–24]. In addition, a POC platform should allow for facile multiplexing for the simultaneous detection of multiple biomarkers. Many infectious diseases exhibit the same symptoms[25]; multiplexing tests for several diseases in parallel on the same device, thereby increasing accurate diagnosis and proper subsequent treatment.

Presently, the majority of infectious disease POC diagnostics available for use in resource limited settings are microscopy, agglutination tests, and lateral flow assays (LFA)[26–28]. Microscopy provides an economical, specific diagnostic platform for detection of live infections when performed with clean equipment and an appropriately trained staff[29,30]. However, procurement of quality slides and microscopes presents a major challenge, and many rural facilities suffer from staffing constraints and untrained personnel. Agglutination tests provide a simple visual readout by eye based on the aggregation of latex beads in the presence of a specific pathogen (Fig 1.1.1a)[31–33]. Presently, agglutination tests for infectious diseases are utilized primarily for the detection of HIV[34,35], as well as several other sexually transmitted infections such as hepatitis C virus (HCV) and syphilis[36]. Although cost-effective, agglutination assays are only semi-quantitative at best and the reagents have a limited shelf-life in non-refrigerated POC settings. LFAs (commonly termed "dipsticks") are the most successful POC diagnostic format commercially available, providing the platform for the at-home pregnancy test. LFAs are also currently used for POC detection of infectious diseases such as malaria[37,38] and HIV[39,40]. Detection is based on visual readout; a colored strip appears when a sufficient quantity of the analyte of interest is present in the sample tested (Fig 1.1.1b)[41–

[43]. LFAs for POC detection of infectious disease are relatively inexpensive and require low sample volume. In addition, LFAs provide a quicker turnaround time (~15 min) and are often more sensitive than their agglutination assay counterpart[44,45]. However, similar to agglutination tests, LFAs are not quantitative and reagent stability under harsh conditions remains a challenge[46,47]. Moreover, while a major advantage of agglutination tests and LFAs is ease of portability, both assays tend not to meet the sensitivity and specificity criteria required for rapid test approval in most developed countries (>99% sensitivity and ≥98% specificity)[48]. Agglutination tests and LFAs may be adequate for certain "present/not present"-type diagnostic purposes, however further improvement of these devices and new innovative approaches must be taken to develop sensitive and quantitative POC detection systems for infectious disease.

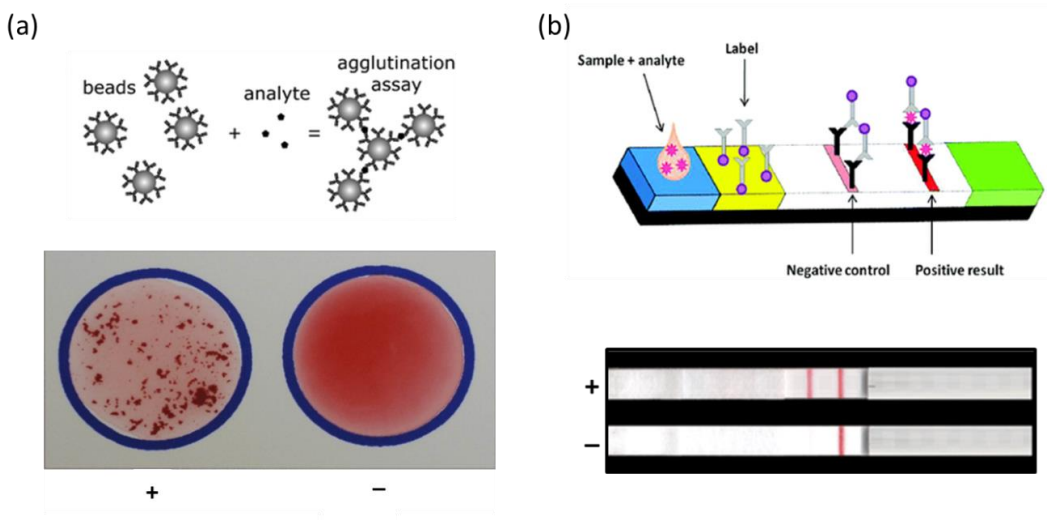

Figure 1.1.1. Current infectious disease POC diagnostics. (a) Agglutination assays consist of beads with capture antibodies that, when mixed with sample containing the target analyte, result in bead aggregation. A positive result (+) produces aggregation that is discernible by eye from the colloidal solution (-) where the analyte is absent. Images adapted from reference 49 and reference 50. (b) Typical LFA format. Sample is applied to the end of the dipstick; target analyte present in the sample binds to the antibody-conjugated label. Analyte-antibody complexes bind to the test line to return a positive result (+) of two red strips (test line and control line). If the analyte is absent, the label binds to the control line only, generating a negative result (-) of one red strip. Images adapted from reference 51.

One step to improve current POC technologies is the integration of microfluidics onto these existing detection platforms. Microfluidics utilizes microfabricated channels, commonly composed of elastomers such as polydimethylsiloxane (PDMS), to enclose and manipulate small volumes of fluid, allowing for lab-on-chip devices (i.e. micrototal analysis systems)[52–54]. A critical application of lab-on-chip devices is the automation of sample preparation, enabling steps such as purification, mixing, and extraction without any user interference (Figure 1.1.2)[55,56]. Sample preparation in low resource settings poses a difficult task due to staffing constraints and limited reagent shelf life in harsh conditions; integration of microfluidics to produce a lab-on-chip device could greatly reduce the need for trained staff, and improve reagent lifetime via enclosed, on-chip reagent storage. In addition, microfluidic platforms composed of polymers such as PDMS are manufacturable by methods that allow high production at very low cost-per-part[57]. Therefore, incorporation of microfluidics onto POC platforms could greatly advance diagnostics in resource limited areas, while feasibly allowing these lab-on-chip devices to be cost-effective.

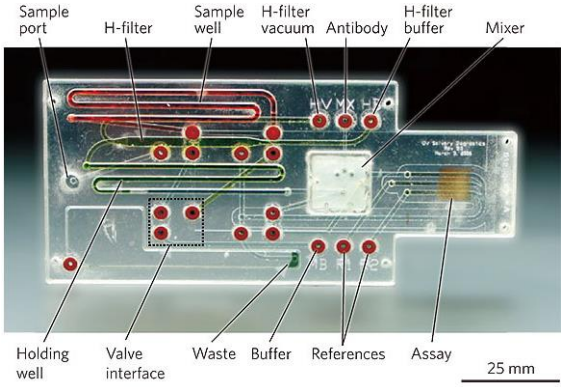

Figure 1.1.2. Example of a microfluidic device composed of PDMS for automated sample preparation. Image adapted from reference 58.

A multitude of current POC diagnostic platforms have been integrated with microfluidics in an attempt towards developing prospective next-generation POC devices[58–60]. Several LFA-based platforms have been integrated with microfluidics[61–64]. A major pitfall of LFAs is the lack of flow rate control which results in non-uniform dispersion and mixing of sample over the strip and as a consequence, variability in batch-to-batch reproducibility. The addition of microfluidics allows for controlled sample delivery and reagent mixing, thereby generating more reproducible and more quantitative results[65,66]. However, many of these adapted assays require external bulky bench-top pumps or involve microfluidics that are too complex to be cost-effective[58]. Despite improving sensitivity, the added complexity of these LFA-based platforms takes away from desired POC qualities.

1.2 Nanoscale-based detection platforms

Over the past few decades, nanotechnology has emerged as a rapidly growing, inter-disciplinary field with high expectations to lead to major advancements in the development of biosensors. Briefly, the field of nanotechnology involves the study, fabrication, and use of structures with dimensions typically smaller than 1 μm. At the sub-micron scale, materials exhibit unique optical, electrical, and structural behaviors that significantly differ from their bulk, macroscopic properties[67–69]. One such effect is seen optically with nanoparticles, which can emit different frequencies of visible light based on their size. For example, bulk gold exhibits the 'golden' yellow color with which we are familiar; however, gold nanoparticles can appear anywhere from red to blue depending on their size (Fig 1.2.1a)[70]. Similarly, quantum dots (QDs) are semiconductor nanoparticles whose fluorescence emission wavelength is size dependent (Fig 1.2.1b). These color-tunable particles provide a sharp, detailed spectrum and do not exhibit photobleaching, unlike commonly used organic fluorescent dyes[71]. In addition, nanoscaled dimensions exhibit unique structural and electrical properties due to an increased surface area to volume ratio. This places a majority of the atoms at the structure surface, allowing atoms to be more readily accessible for chemical reactions, biofunctionalization, and signal detection[72].

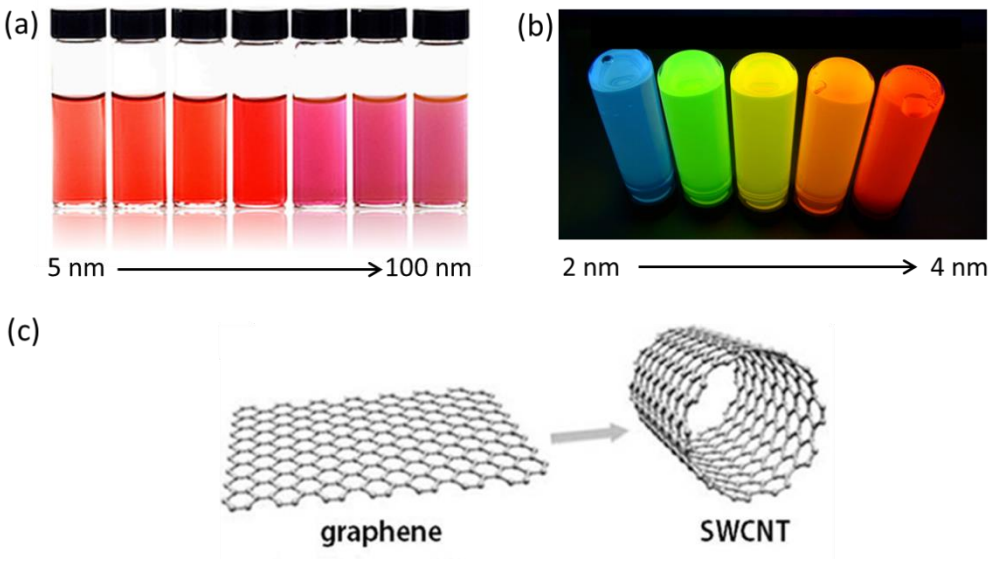

Figure 1.2.1. Nanoscale materials and their properties. Size-dependent spectrum of (a) gold nanoparticles and (b) CdSe semiconductor quantum dots. (c) Structure of a single-walled carbon nanotube (SWCNT) which is composed solely of surface atoms. Image credit (a) reference 73 (b) reference 74 (c) reference 75.

The unique properties of nanoscale materials - such as nanotubes[76], nanowires[77,78] and nanoparticles[79]– have been manipulated for the development of sensitive biosensors. Carbon nanotubes (CNTs) are an exemplary, well-studied nanomaterial whose structure resembles a cylindrical graphene sheet (Fig 1.2.1c)[80–83]. The unique structure of CNTs consists exclusively of surface atoms; thus, small changes in the surrounding environment can cause drastic changes in their electrical and optical properties. In addition, their diameters are comparable to the size of single molecules (~1-3 nm), making CNTs very sensitive to the adsorption or binding of biomolecules. In this fashion, CNTs can function as sensitive, label-free biosensors upon binding of a target molecule[84–86]. For example, a CNT-based immunosensor demonstrated detection of

disease-specific autoantibodies from human serum, with sensitivity and specificity that was significantly greater than established ELISA and microarray methods[87]. In the same manner, silicon nanowires have been used for ultrasensitive biomolecule detection. Patolsky *et al.* demonstrated selective, electrical detection of a single virus molecule using a silicon nanowire field effect transistor, exhibiting the extraordinary potential of nanotechnology to detect viral threats at the single molecule level[88].

Nanoparticles have also received much attention in their wide variety of applications towards advancing biosensor technology[89,90]. Nanoparticles can be biocompatible and exhibit high surface area, enabling biomolecule immobilization and subsequent signal amplification. In this manner, nanoparticles have been labeled with reporter molecules (e.g. enzyme, redox species) to enhance signal and increase detection sensitivity[91]. Liu *et al.* demonstrated highly sensitive protein detection using enzyme-labeled gold nanoparticles[92]. Labeled gold nanoparticles detected the cancer biomarker carcinoembryonic antigen (CEA) with a 130-fold increase in sensitivity over the conventional ELISA, with a detection limit of 12 ng/L.

Nanotechnology research has predominately focused on biomedical applications, specifically on advancing drug delivery, therapeutics, and imaging in oncologic disease[93–96]. Due to the inability of most drugs to efficiently reach the target tissue, much effort has been put into improving drug delivery. Because of their small size, nanoparticles loaded with drug can penetrate through small capillaries and several biological barriers (such as the blood brain barrier), which allows for efficient drug accumulation at the

target site[97,98]. In addition, drugs used for chemotherapy indiscriminately damage malignant and normal cells, resulting in the adverse side effects associated with treatment. Targeted drug delivery to the cancer cells utilizing labeled nanoparticles would selectively target the tumor cells and lessen the negative side effects of chemotherapy[99]. Furthermore, magnetic nanoparticles can be delivered to the tumor site and allow for improved, site-directed thermal ablation therapeutics in the removal of malignant cells[100,101]. Nanoparticles are also being exploited to improve tumor imaging where current techniques face the disadvantage of fluorescence photobleaching; QDs are resistant to photobleaching and, like other nanoparticles, can be labeled to directly target the site of interest for imaging[102].

Although much of the aforementioned research has primarily focused on oncologic disease applications in a clinical setting, significant attention has shifted towards infectious disease applications due to a recent rise in antibiotic resistance paralleled with globalization[7,103,104]. The need for sensitive and robust diagnostics to monitor and detect infectious disease has become essential as the threat of a pandemic has become increasingly real. Several studies have been performed on improving LFAs and agglutination tests with the addition of nanomaterials[105,106]. LFAs for malaria[107] and HIV[108] detection have been improved using gold nanoparticles as the contrast agent. Gold nanoparticles have a high affinity for biomolecule labeling and remain stable in colloidal solution for long periods of time, producing more sensitive LFAs compared to the traditional dyed-latex counterpart[109]. Gold nanoparticles have also been adapted to improve agglutination assays[110,111]. The inertness and stability of colloidal gold

decreases innate particle aggregation seen with latex beads, allowing for true signal to be easily discernable from background aggregation and thereby increasing sensitivity[112]. In addition, the incorporation of nanoparticles has allowed for quantification due to the occurrence of plasmon coupling in aggregated metallic nanoparticles. For example, Halas *et al.* detected immunoglobulin from whole blood with a sensitivity range comparable to the standard ELISA[113]. However in order to make the assay quantitative, a spectrophotometer was required, introducing complex instrumentation that may not be amenable for POC applications. Interfacing nanomaterials with previous POC platforms improves the performance and stability of these existing technologies; however in order to fully realize a truly POC diagnostic for infectious diseases, multiplexed devices must be developed.

The ability to simultaneously screen for multiple pathogens would provide a critical tool in preventing outbreaks and disease spread. Many diseases share similar symptoms and so diagnosis may be near impossible without a panel of disease markers with which to screen against[114]. In addition, pathogens such as the *Plasmodium* parasites and HIV are present in multiple strains, and correct strain identification could improve the efficiency of treatment[115,116]. Therefore, major focus has been placed on the development of multiplexed assay systems that can detect a host of infectious disease biomarkers (e.g. molecules, whole viruses, bacteria) simultaneously. Quantum dot barcode assays are one approach that has been well developed as a nanotechnology-based multiplexed assay[117–119]. In such an assay, QDs of a unique color are labeled respectively to a specific target

biomarker of interest; therefore, multiple targets can be probed for simultaneously, with each target corresponding to its own unique color, or "barcode" (Figure 1.2.2).

Multiplexed barcode assays have been developed for infectious diseases such as HIV, malaria, syphilis, HCV, and hepatitis B virus (HBV)[120–122]. These barcode assays rapidly detected multiple infectious pathogens simultaneously from low sample volumes (~100 μl) and demonstrated sensitivities that exceeded the standard ELISA detection method. For example, Klostranec *et al.* observed a 50-fold improvement in the multiplexed detection of HIV, HBV, and HCV compared to FDA-approved ELISA kits[120]. However, these assays require considerable laboratory equipment (e.g. spectrophotometers) in order to detect and quantify barcode signal, proving it difficult to adapt these assays to POC applications. Recently, a quantum dot barcode assay was integrated with a handheld smartphone optical device[123], demonstrating rapid, multiplexed detection of HIV and hepatitis from real patient samples. While this handheld device holds potential for portability of a barcode assay, the sensitivity was lacking (1000 viral copies/ml) compared to standard PCR diagnostics, whose detection limits can reach as low as 40 viral copies/ml[124]. Further development in the sensitivity and portability of such handheld devices must be explored before optical readout assays could be considered for POC diagnostics.

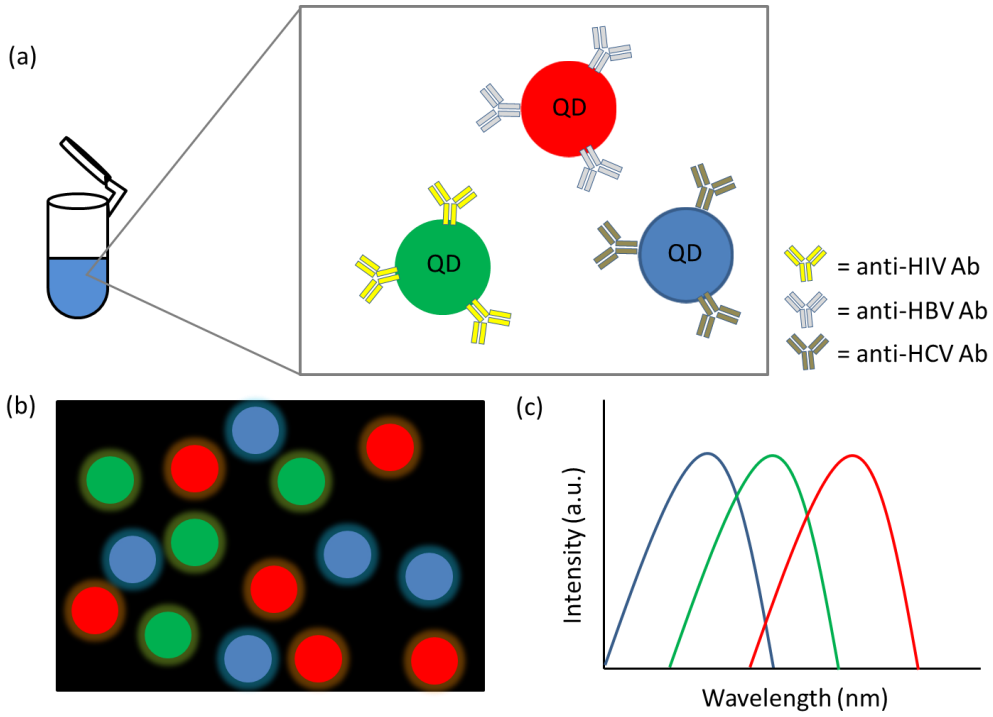

Figure 1.2.2. Barcode assay schematic. (a) Sample is added to solution containing labeled QDs of varying fluorescent color. Each unique QD color, or "barcode", is labeled with antibody against a specific target biomarker. In this case, green fluorescing QDs are labeled with anti-HIV Ab, red fluorescing QDs are labeled with anti-HBV Ab, and blue-fluorescing QDs are labeled with anti-HCV Ab. After incubation with sample, a capture assay is performed to isolate only QDs that have target analyte bound to them. (b) Presence of target analyte is observed with fluorescence imaging of captured QDs. (c) Signal intensity is determined for each QD barcode in order to quantify analyte.

1.3 Electrochemical sensors for point-of-care platforms

In the studies previously described (e.g. LFAs, agglutination, barcode assays), the majority of the POC platforms is based on optical readout. While optical detection methods have proven sensitive and reliable in clinical settings, the need for expensive and bulky instrumentation inhibits their use for POC needs. Electrochemical detection offers several advantages over optical methods for such POC applications[125–130]. Platforms for electrochemical detection are easily amenable to miniaturization, allowing for facile multiplexing and integration with microfluidic systems. Optical systems are often still too difficult to miniaturize while maintaining sensitivity, and therefore require larger reagent volumes and longer analysis time. In addition, electrochemical techniques do not require the optical instrumentation (Fig 1.3.1a) that impedes the portability of optical readout devices. Instead, electrochemical signals are measured by a potentiostat. Potentiostats operate by controlling voltage to a constant value and recording change in current due to an electrochemical event[131]. Miniaturized handheld potentiostats are commercially available (Fig 1.3.1b) and allow for portability of electrochemical devices, an essential POC factor that restricts many technologies from becoming POC.

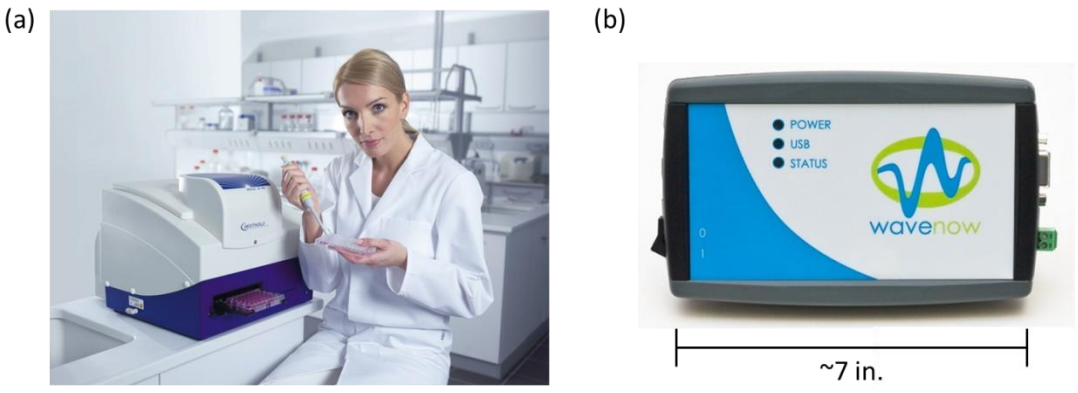

Figure 1.3.1. Instrumentation required for optical and electrochemical readout. (a) For optical detection, a standard spectrophotometer is used to measure a 96-well plate for conventional ELISA reactions. Image taken from reference 132. (b) Handheld potentiostats are used for portable, sensitive electrochemical detection, an option not readily available for the pictured spectrophotometer. Image adapted from reference 133.

Electrochemical detection offers the ability to achieve sensitive and specific detection of biomarkers at low cost and in real-time, utilizing simple instrumentation[134–136]. The development and commercial success of electrochemical glucose sensor strips for blood sugar monitoring in diabetic patients demonstrates the low-cost and portability of such an electrochemical-based POC technology[137]. However as mentioned, many POC technologies have predominately been based on optical readout. Previously, electrochemical sensors suffered from a lack of electrode surface architectures that would allow for high sensitivity comparable to optical methods[138,139]. Additionally, while the success of the glucose sensor is compelling for electrochemical POC devices, the detection scheme is based on an inherent redox reaction linked to the oxidation of glucose

by glucose oxidase (Figure 1.3.2)[140]. Therefore, detection of other analytes (e.g. non-redox active molecules) would require further development of electrochemical-based detection strategies.

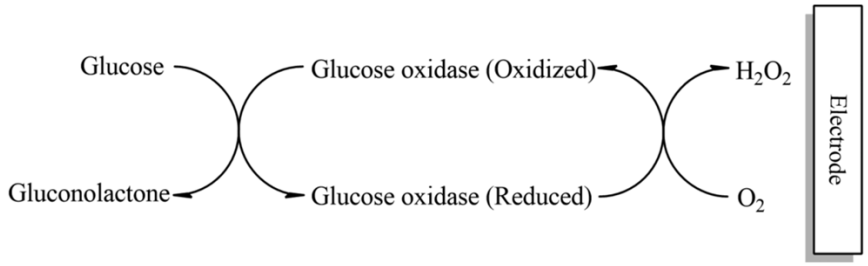

Figure 1.3.2. Basic mechanism of glucose sensor detection scheme. Image taken from reference 141.

Focus has shifted to electrochemical means in the past decade with the explosion of nanotechnology coinciding with the development of numerous electrochemical-based detection strategies. With this rapid growth of nanotechnology, there has been a surge of novel nanoarchitectures that, by shrinking sensor dimensions and thereby enhancing electrode surface area, have increased electrochemical signal-to-noise ratios compared to their macroscopic counterparts[142–144]. The high surface areas of these electrodes significantly improve sensitivity, placing electrochemical methods on a competitive level with optical technologies. Furthermore, countless electrochemical detection strategies have been developed to monitor analytes with high sensitivity that are not inherently redox active, including proteins[145,146], DNA[147,148], microRNAs[149], metabolites[150,151], drugs[152], and enzymatic activity[153]. Several well-established approaches include sandwich-type assays to deliver electrochemically active groups[154–156], electrochemically

adapted barcode assays[157,158], and non-covalent redox reporter systems[159,160]. Moreover, using these electrochemical detection strategies in conjunction with nanostructured electrode surfaces – such as carbon nanotubes [161], nanowires[162], and metallic nanoparticles[163]– exhibit increased sensitivity for biomarker detection over conventional techniques. For example, Zhang *et al.* achieved femtomolar detection levels of DNA using a nanoparticle-based platform combined with a non-covalent redox reporter system[164]. In addition, the assay exhibited excellent selectivity against base pair mismatch and a rapid analysis time, two components lacking in the standard PCR technique.

Many of these developed electrochemical strategies employed in conjunction with nanostructures have been characterized for the detection of oncologic disease[165,166]. The development of highly sensitive, cost-effective detection and monitoring strategies of cancer biomarkers is critical due to the disease's prevalence and high rate of mortality at late stage diagnosis. Ultrasensitive detection of cancer biomarkers with electrochemical-based platforms has been achieved, reaching attomolar detection limits for multiple biomarker types, including protein[167], DNA[168], and microRNA[169]. For example, Tang *et al.* developed an ultrasensitive immunosensor for the detection of cancer biomarker interleukin-6 (IL-6) using an electrochemical enzyme-labeled sandwich assay (Figure 1.3.3)[170]. The detection limit was remarkably low at 10 fg/ml (~390 aM) with a dynamic range extending to 1300 fg/ml. Many cancer biomarkers have threshold levels (*i.e.* concentrations correlating to disease state) in the pg/ml range; therefore these ultralow

detection limits demonstrated with electrochemical platforms could facilitate early detection and proper monitoring of disease progression[171–173].

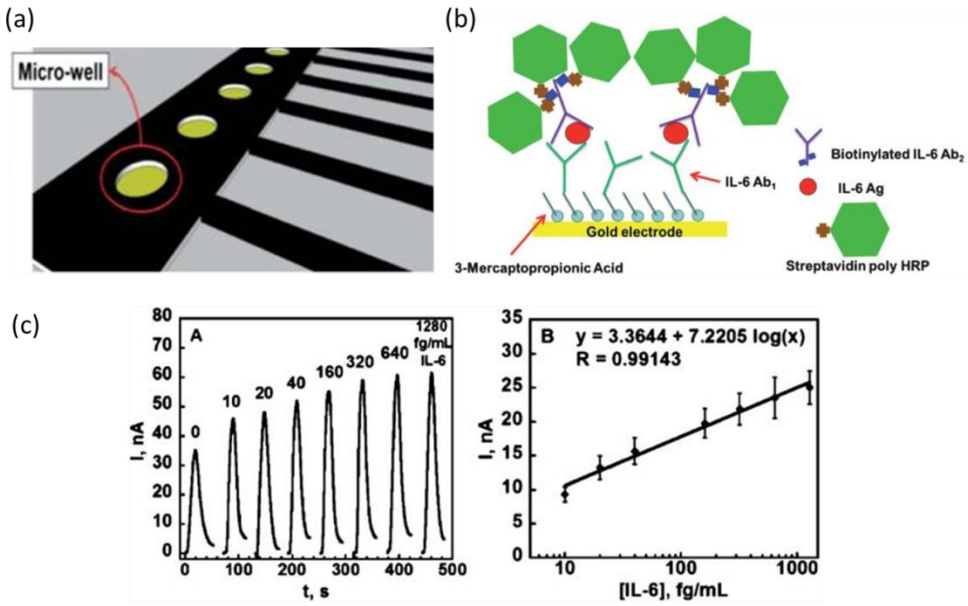

Figure 1.3.3. Detection of cancer biomarker via electrochemical sandwich assay. (a) Device composed of 8 individually addressable electrodes, each with 0.45 mm^2 area. (b) Schematic of electrochemical sandwich assay to detect cancer biomarker IL-6, using horse radish peroxidase (HRP) as the amplification tag. (c) Amperometric response after exposure to diluted serum containing IL-6 and HRP-labeled secondary antibody (left); dynamic range of sensor for IL-6 detection (right). [Image from reference 170]

Impressively, nano-based electrochemical techniques allow some of these detection methods to be label-free, achieving sensitive and specific detection of cancer biomarkers without signal enhancement via an enzyme or redox reporter system[174–176]. As previously mentioned, nanostructured electrodes (notably CNTs and nanowires) are very sensitive to the adsorption or binding of biomolecules due to the size comparability of a single

molecule to the nanostructured aspect of the electrode. For example, Lieber *et al.* demonstrated sensitive label-free, multiplexed electrical detection of cancer biomarkers from serum utilizing a silicon nanowire sensor array (Figure 1.3.4)[177]. They achieved a detection limit of 0.9 pg/ml prostate-specific antigen (PSA), surpassing the detection limit of the conventional ELISA (3 pg/ml). Additionally, carbon nanotube based platforms are easily amenable for label-free electrochemical detection, as demonstrated by Tran *et al*. Their CNT-based immunosensor detected the prostate cancer microRNA biomarker miR-141 with a very low detection limit of 8 fM, significantly below the typical sub-pM threshold level of many microRNA biomarkers[178].

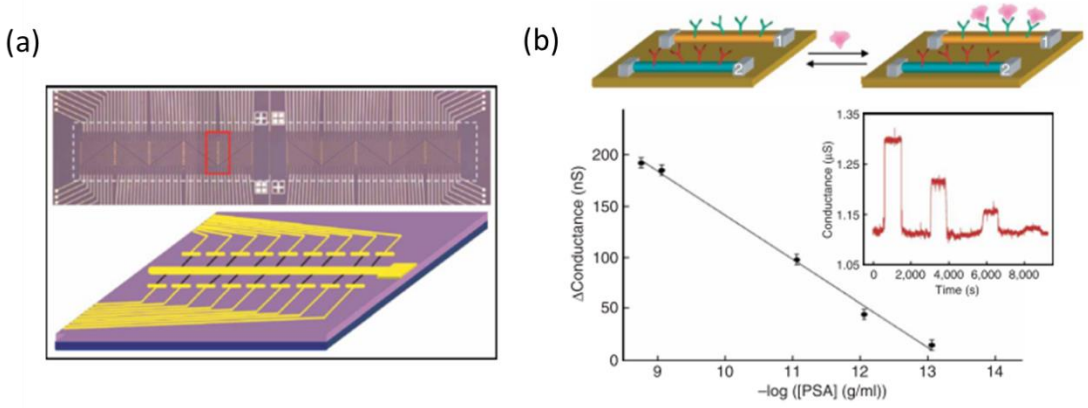

Figure 1.3.4. Detection of cancer biomarkers with nanowire arrays. (a) Arrays were fabricated with ~200 individually addressable nanowires. Top image: full nanowire array, 8 mm x 1.2 mm in size. Bottom image: view inside the red rectangle; black lines denote individual silicon nanowires. (b) Top: schematic of nanowires conjugated with anti-PSA antibody. Below: detection and sensitivity range for nanowire capture of PSA denoted by conductance change vs. log scale of PSA concentration. Image from reference 177.

While these electrochemical-based nanosensors offer highly sensitive tools for potential oncologic disease monitoring and diagnosis, there remain several challenges for continued development towards POC biosensors. A predominant issue is the lack of clinically validated cancer biomarkers; only nine cancer biomarkers are currently FDA-approved despite an extensive list of candidate biomarkers[179]. The low numbers of validated biomarkers (~3% of all candidate biomarkers) is largely attributed to the inability of current technologies to identify biomarkers with high specificity for a particular disease[180]. Even the nine clinically approved biomarkers are neither specific nor sensitive enough to diagnose the correct disease on their own. Therefore, biomarker discovery and clinical verification must continue in order to develop multiplexed panels of validated biomarkers for sensitive and specific disease diagnosis[181,182]. In addition, a significant challenge for a majority of electrochemical biomarker sensors is biofouling and contamination of the electrode surface with complex biological samples such as whole serum[183]; this prevents clinical validation of the sensors with real sample testing. The integration of microfluidics onto these electrochemical-based platforms could greatly advance these tools for clinical diagnostics by integrating sample pre-treatment (*e.g.* extraction, purification, mixing) of complex biological materials[184–186]. However, the addition of complex microfluidics negates the cost-effectiveness of electrochemical platforms; therefore there remains a need to affordably integrate microfluidics onto these systems.

While emphasis has previously been placed on electrochemical strategies for oncologic disease, electrochemical-based platforms for infectious disease detection remain an

unchartered territory in comparison. However, focus and funding has recently shifted to infectious disease applications due to a rapid rise in antibiotic resistance alongside growing threats of an epidemic-to-pandemic potential. Electrochemical sensing schemes are being adapted and developed for the detection of infectious disease biomarkers; sensitive and specific detection of infectious diseases such as HBV[187,188], HCV[189,190], HIV[191–193], and influenza viruses[194,195] have been demonstrated utilizing viral nucleic acids or viral peptides as the targeted biomarkers. For example, Chen *et al.* exhibited ultrasensitive electrochemical detection of HIV DNA from complex biological samples. Viral DNA was captured onto the electrode surface by complementary probe DNA and subsequently detected by a non-covalent redox reporter system, with a detection limit of 5 aM[196]. Although the use of electrochemical sensors towards infectious disease is still novel and limited at this time, further development of these technologies will provide an attractive option for robust, sensitive POC devices.

Electrochemical nanosensors provide a potential means for sensitive, specific, cost-effective detection of infectious disease biomarkers with rapid analysis times. They provide a miniaturized platform amenable to multiplexing for the detection of multiple infectious disease markers on one device, while maintaining portability and ease of deployment in resource limited areas. With the integration of microfluidics and the hand held potentiostat, electrochemical-based sensors present an optimal means of detection in the development of infectious disease POC diagnostics. While their application in infectious disease POC is limited at this time, electrochemical-based sensors present an

untapped resource to exponentially advance diagnostics in resource limited areas and fill the void in infectious disease detection.

1.4 Aims of study

The research presented in this dissertation involves the evaluation of two novel nanoarchitectures as electrochemical sensors and their development into biosensors for infectious disease detection. This work was completed in collaboration with the physics laboratory of Dr. Michael J. Naughton, where the nanostructures were designed and fabricated.

Two nanostructures, the nanocoax and dendrites, were each developed and characterized as electrochemical sensors for the detection of cholera toxin (CT). Fabrication of each structure was first investigated and optimized; the structures were then evaluated on their electrochemical performance and compared to the standard method of biomarker detection (the optical ELISA) using CT as the target biomarker. Alkaline phosphatase titrations and electrochemical ELISAs were the two main determinants of electrochemical performance. CT was used as the benchmark biomarker due to its clinical relevance in infectious disease, however the electrochemical ELISA is universal and can be utilized for other infectious disease biomarkers whose antibodies are commercially available.

References

1. Http://www.who.int/mediacentre/factsheets/fs107/en/. *WHO Cholera*. (2012).
2. Harris, J. B., LaRocque, R. C., Qadri, F., Ryan, E. T. & Calderwood, S. B. Cholera. *Lancet* **379,** 2466–76 (2012).
3. Dick, M. H., Guillerm, M., Moussy, F. & Chaignat, C.-L. Review of two decades of cholera diagnostics--how far have we really come? *PLoS Negl. Trop. Dis.* **6,** e1845 (2012).
4. Issadore, D. & Westervelt, R. *Point-of-care Diagnostics on a Chip*. 5 (2013).
5. Tibayrenc, M. *Encyclopedia of infectious diseases: modern methodologies*. xxix–xxiv (2007).
6. Neumann, G., Noda, T. & Kawaoka, Y. Emergence and pandemic potential of swine-origin H1N1 influenza virus. *Nature* **459,** 931–9 (2009).
7. Hauck, T. S., Giri, S., Gao, Y. & Chan, W. C. W. Nanotechnology diagnostics for infectious diseases prevalent in developing countries. *Adv. Drug Deliv. Rev.* **62,** 438–48 (2010).
8. Yang, S. & Rothman, R. E. PCR-based diagnostics for infectious diseases : uses, limitations, and future applications in acute-care settings. *Lancet Infect. Dis.* **4,** 337–348 (2004).
9. Gan, S. D. & Patel, K. R. Enzyme immunoassay and enzyme-linked immunosorbent assay. *J. Invest. Dermatol.* **133,** e12 (2013).
10. Lequin, R. M. Enzyme immunoassay (EIA)/Enzyme-linked immunosorbent assay (ELISA). *Clin. Chem.* **51,** 2415–8 (2005).

11. Wulfkuhle, J. D., Liotta, L. & Petricoin, E. F. Proteomic applications for the early detection of cancer. *Nat. Rev. Cancer* **3,** 267–75 (2003).

12. Pimbley, D. & Patel, P. A review of analytical methods for the detection of bacterial toxins. *J. Appl. Microbiol.* 98–109 (1998).

13. Berrade, L., Garcia, A. & Camarero, J. Protein microarrays: novel developments and applications. *Pharm. Res.* **28,** 1480–1499 (2011).

14. Lee, H., Wark, A. & Corn, R. Microarray methods for protein biomarker detection. *Analyst* **133,** 975–983 (2008).

15. Aebersold, R. & Mann, M. Mass spectrometry-based proteomics. *Nature* **422,** 198–207 (2003).

16. Hawkridge, A. M. & Muddiman, D. C. Mass spectrometry-based biomarker discovery: toward a global proteome index of individuality. *Annu. Rev. Anal. Chem.* **2,** 265–277 (2009).

17. Mackay, I. M. Real-time PCR in the microbiology laboratory. *Clin. Microbiol. Infect.* **10,** 190–212 (2004).

18. Lanciotti, R. & Kerst, A. Rapid detection of West Nile virus from human clinical specimens, field-collected mosquitoes, and avian samples by a TaqMan reverse transcriptase-PCR assay. *J. Clin. Microbiol.* **38,** 4066–4071 (2000).

19. Peeling, R. W., Holmes, K. K., Mabey, D. & Ronald, A. Rapid tests for sexually transmitted infections (STIs): the way forward. *Sex. Transm. Infect.* **82,** v1–v6 (2006).

20. Kettler, H., White, K. & Hawkes, S. Mapping the landscape of diagnostics for sexually transmitted infections. 2004 WHO. *TDR Publ.* (2004).

21. Olmsted, S., Derose, K. & Beighley, C. Determining access to care and user requirements for diagnostic tests in developing countries. *RAND* **8,** WR–423–HLTH (2006).

22. Ridderhof, J. & Deun, A. Van. Roles of laboratories and laboratory systems in effective tuberculosis programmes. *Bull. World Health Organ.* **039081,** (2007).

23. Cohen, G. Access to diagnostics in support of HIV/AIDS and tuberculosis treatment in developing countries. *Aids* **21,** S81–7 (2007).

24. Petti, C. & Polage, C. Laboratory medicine in Africa: a barrier to effective health care. *Clin. Infect. Dis.* **42,** 377–382 (2006).

25. Mabey, D., Peeling, R. W., Ustianowski, A. & Perkins, M. D. Diagnostics for the developing world. *Nat. Rev. Microbiol.* **2,** 231–40 (2004).

26. Yager, P., Domingo, G. J. & Gerdes, J. Point-of-care diagnostics for global health. *Annu. Rev. Biomed. Eng.* **10,** 107–44 (2008).

27. World Health Organization. *Diagnosis, Prevention and Management of Cryptococcal Disease in HIV-infected Adults, Adolescents and Children*. 1–16 (2011).

28. Reid, M. J. & Shah, N. S. Approaches to tuberculosis screening and diagnosis in people with HIV in resource-limited settings. *Lancet. Infect. Dis.* **9,** 173–84 (2009).

29. Wongsrichanalai, C., Barcus, M. J., Muth, S., Sutamihardja, A. & Wernsdorfer, W. H. A review of malaria diagnostic tools: microscopy and rapid diagnostic test (RDT). *Am. J. Trop. Med. Hyg.* **77,** 119–127 (2007).

30. Nicastri, E. & Bevilacqua, N. Accuracy of malaria diagnosis by microscopy, rapid diagnostic test, and PCR methods and evidence of antimalarial overprescription in non-severe febrile patients in two tanzanian hospitals. *Am. J. Trop. Med. Hyg.* **80,** 712–717 (2009).

31. Harith, A. & Kolk, A. A simple and economical direct agglutination test for serodiagnosis and sero-epidemiological studies of visceral leishmaniasis. *Trans. R. Soc. Trop. Med. Hyg.* **80,** 583–36 (1986).

32. Attar, Z., Chance, M., El-Safi, S. & Carney, J. Latex agglutination test for the detection of urinary antigens in visceral leishmaniasis. *Acta Trop.* **78,** 11–16 (2001).

33. Riggin, C., Beltz, G. & Hung, C. Detection of antibodies to human immunodeficiency virus by latex agglutination with recombinant antigen. *J. Clin. Microbiol.* **25,** 1772–1773 (1987).

34. Peeling, R. & Mabey, D. Point-of-care tests for diagnosing infections in the developing world. *Clin. Microbiol. Infect.* 1062–1069 (2010).

35. Ramalingam, S. Rapid particle agglutination test for human immunodeficiency virus: hospital-based evaluation. *J. Clin. Microbiol.* **40,** 1553–1554 (2002).

36. Hess, K. L., Fisher, D. G. & Reynolds, G. L. Sensitivity and specificity of point-of-care rapid combination syphilis-HIV-HCV tests. *PLoS One* **9,** e112190 (2014).

37. Bell, D., Wongsrichanalai, C. & Barnwell, J. W. Ensuring quality and access for malaria diagnosis: how can it be achieved? *Nat. Rev. Microbiol.* **4,** 682–95 (2006).

38. Murray, C. K., Gasser, R., Magill, A. J. & Miller, R. S. Update on rapid diagnostic testing for malaria. *Clin. Microbiol. Rev.* **21,** 97–110 (2008).

39. Stürenburg, E. & Junker, R. Point-of-care testing in microbiology: the advantages and disadvantages of immunochromatographic test strips. *Dtsch. Arztebl. Int.* **106,** 48–54 (2009).

40. Branson, B. M. State of the art for diagnosis of HIV infection. *Clin. Infect. Dis.* **45,** S221–5 (2007).

41. Sajid, M., Kawde, A.-N. & Daud, M. Designs, formats and applications of lateral flow assay: A literature review. *J. Saudi Chem. Soc.* (2014).

42. Smits, H. & Eapen, C. Lateral-flow assay for rapid serodiagnosis of human leptospirosis. *Clin. Diagn. Lab. Immunol.* **8,** 166–169 (2001).

43. Posthuma-Trumpie, G., Korf, J. & van Amerongen, A. Lateral flow (immuno)assay: its strengths, weaknesses, opportunities and threats. A literature survey. *Anal. Bioanal. Chem.* **393,** 569–82 (2009).

44. Kozel, T. & Bauman, S. CrAg lateral flow assay for cryptococcosis. *Expert Opin. Med. diagnosis* **6,** 775–784 (2012).

45. Hospenthal, D. & Rinaldi, M. *Diagnosis and Treatment of Fungal Infections*. 182 (2015).

46. Jorgensen, P. & Chanthap, L. Malaria rapid diagnostic tests in tropical climates: the need for a cool chain. *Am. Soc. Trop. Med.* **74,** 750–754 (2006).

47. Chiodini, P. & Bowers, K. The heat stability of Plasmodium lactate dehydrogenase-based and histidine-rich protein 2-based malaria rapid diagnostic tests. *Trans. R. Soc. Trop. Med. Hyg.* **101,** 331–337 (2007).

48. Lee, H. & Allain, J. Improving blood safety in resource poor settings. *Vox Sang.* **87,** 176–179 (2004).

49. Wiklund, M. & Hertz, H. M. Ultrasonic enhancement of bead-based bioaffinity assays. *Lab Chip* **6,** 1279–92 (2006).

50. ELITech Group. <www.elitechgroup.com>

51. Wilson, R. The use of gold nanoparticles in diagnostics and detection. *Chem. Soc. Rev.* **37,** 2028–45 (2008).

52. Dittrich, P., Tachikawa, K. & Manz, A. Micro total analysis systems. Latest advancements and trends. *Anal. Chem.* **78,** 3887–3908 (2006).

53. Reyes, D., Iossifidis, D., Auroux, P. & Manz, A. Micro total analysis systems: Introduction, theory, and technology. *Anal. Chem.* **74,** 2623–2636 (2002).

54. Whitesides, G. M. The origins and the future of microfluidics. *Nature* **442,** 368–73 (2006).

55. Liu, R., Yang, J. & Lenigk, R. Self-contained, fully integrated biochip for sample preparation, polymerase chain reaction amplification, and DNA microarray detection. *Anal. Chem.* **76,** 1824–1831 (2004).

56. Paegel, B. M., Blazej, R. G. & Mathies, R. Microfluidic devices for DNA sequencing: sample preparation and electrophoretic analysis. *Curr. Opin. Biotechnol.* **14,** 42–50 (2003).

57. Sollier, E., Murray, C., Maoddi, P. & Di Carlo, D. Rapid prototyping polymers for microfluidic devices and high pressure injections. *Lab Chip* **11,** 3752–65 (2011).

58. Yager, P. *et al.* Microfluidic diagnostic technologies for global public health. *Nature* **442,** 412–8 (2006).

59. Gervais, L., de Rooij, N. & Delamarche, E. Microfluidic chips for point-of-care immunodiagnostics. *Adv. Mater.* **23,** H151–76 (2011).

60. Chin, C. D., Linder, V. & Sia, S. K. Commercialization of microfluidic point-of-care diagnostic devices. *Lab Chip* **12,** 2118–34 (2012).

61. Yetisen, A. K., Akram, M. S. & Lowe, C. R. Paper-based microfluidic point-of-care diagnostic devices. *Lab Chip* **13,** 2210–51 (2013).

62. Gervais, L. & Delamarche, E. Toward one-step point-of-care immunodiagnostics using capillary-driven microfluidics and PDMS substrates. *Lab Chip* **9,** 3330–7 (2009).

63. Chen, Z. *et al.* A microfluidic system for saliva-based detection of infectious diseases. *Ann. N. Y. Acad. Sci.* **1098,** 429–36 (2007).

64. Dudek, M., Lindahl, T. & Killard, A. Development of a point of care lateral flow device for measuring human plasma fibrinogen. *Anal. Chem.* **82,** 2029–2035 (2010).

65. Jönsson, C. *et al.* Silane-dextran chemistry on lateral flow polymer chips for immunoassays. *Lab Chip* **8,** 1191–7 (2008).

66. Stevens, D. Y. *et al.* Enabling a microfluidic immunoassay for the developing world by integration of on-card dry reagent storage. *Lab Chip* **8,** 2038–45 (2008).

67. Klostranec, J. M. & Chan, W. C. W. Quantum dots in biological and biomedical research: recent progress and present challenges. *Adv. Mater.* **18,** 1953–1964 (2006).

68. Daniel, M. & Astruc, D. Gold nanoparticles: assembly, supramolecular chemistry, quantum-size-related properties, and applications toward biology, catalysis, and nanotechnology. *Chem. Rev.* **104,** 293−346 (2004).

69. Rosi, N. & Mirkin, C. Nanostructures in biodiagnostics. *Chem. Rev.* **105,** 1547−1562 (2005).

70. He, Y. Q., Liu, S. P., Kong, L. & Liu, Z. F. A study on the sizes and concentrations of gold nanoparticles by spectra of absorption, resonance Rayleigh scattering and resonance non-linear scattering. *Spectrochim. Acta. A. Mol. Biomol. Spectrosc.* **61,** 2861–6 (2005).

71. Chan, W. & Nie, S. Quantum dot bioconjugates for ultrasensitive nonisotopic detection. *Science* **281,** 2016–2018 (1998).

72. NanoInk. *Introduction to nanoscale science and technology*. (2010).

73. nanoComposix. <www.nanocomposix.com>

74. AZoNano. <www.azonano.com>

75. Vidu, R. *et al.* Nanostructures: a platform for brain repair and augmentation. *Front. Syst. Neurosci.* **8,** 1–24 (2014).

76. Bandaru, P. R. Electrical properties and applications of carbon nanotube structures. *J. Nanosci. Nanotechnol.* **7,** 1239–1267 (2007).

77. Bergin, S. M. *et al.* The effect of nanowire length and diameter on the properties of transparent, conducting nanowire films. *Nanoscale* **4,** 1996–2004 (2012).

78. Wu, Y., Yan, H. & Huang, M. Inorganic semiconductor nanowires: rational growth, assembly, and novel properties. *Chem. A Eur. J.* **8,** 1260–1268 (2002).

79. Coronado, E., Encina, E. R. & Stefani, F. D. Optical properties of metallic nanoparticles: manipulating light, heat and forces at the nanoscale. *Nanoscale* **3,** 4042–59 (2011).

80. Balasubramanian, K. & Burghard, M. Chemically functionalized carbon nanotubes. *Small* **1,** 180–92 (2005).

81. Thostenson, E., Ren, Z. & Chou, T. Advances in the science and technology of carbon nanotubes and their composites: a review. *Compos. Sci. Technol.* **61,** 1899–1912 (2001).

82. Volder, M. De, Tawfick, S., Baughman, R. & Hart, A. Carbon nanotubes: present and future commercial applications. *Science* **339,** 535–539 (2013).

83. Terrones, M. Science and technology of the twenty-first century: synthesis, properties, and applications of carbon nanotubes. *Annu. Rev. Mater. Res.* **33,** 419–501 (2003).

84. Byon, H. & Choi, H. Network single-walled carbon nanotube-field effect transistors (SWNT-FETs) with increased Schottky contact area for highly sensitive biosensor applications. *J. Am. Chem. Soc.* **128,** 2188–2189 (2006).

85. Tam, P. D., Van Hieu, N., Chien, N. D., Le, A.-T. & Anh Tuan, M. DNA sensor development based on multi-wall carbon nanotubes for label-free influenza virus (type A) detection. *J. Immunol. Methods* **350,** 118–24 (2009).

86. Maehashi, K. & Matsumoto, K. Label-free electrical detection using carbon nanotube-based biosensors. *Sensors* **9,** 5368–78 (2009).

87. Drouvalakis, K. *et al.* Peptide-coated nanotube-based biosensor for the detection of disease-specific autoantibodies in human serum. *Biosens. Bioelectron.* **23,** 1413–21 (2008).

88. Patolsky, F. & Zheng, G. Electrical detection of single viruses. *Proc. Natl. Acad. Sci.* **101,** 1–6 (2004).

89. Shipway, A., Katz, E. & Willner, I. Nanoparticle arrays on surfaces for electronic, optical, and sensor applications. *ChemPhysChem* 18–52 (2000).

90. Penn, S. Nanoparticles for bioanalysis. *Curr. Opin. Chem. Biol.* **7,** 609–615 (2003).

91. Cao, X., Ye, Y. & Liu, S. Gold nanoparticle-based signal amplification for biosensing. *Anal. Biochem.* **417,** 1–16 (2011).

92. Liu, M. *et al.* Highly sensitive protein detection using enzyme-labeled gold nanoparticle probes. *Analyst* **135,** 327–31 (2010).

93. Sahoo, S. K., Parveen, S. & Panda, J. J. The present and future of nanotechnology in human health care. *Nanomedicine* **3,** 20–31 (2007).

94. Sahoo, S. & Labhasetwar, V. Nanotech approaches to drug delivery and imaging. *Drug Discov. Today* **8,** 1112–1120 (2003).

95. Silva, G. Introduction to nanotechnology and its applications to medicine. *Surg. Neurol.* **61,** 216–20 (2004).

96. Cai, W. & Chen, X. Nanoplatforms for targeted molecular imaging in living subjects. *Small* **3,** 1840–54 (2007).

97. Panyam, J., Sahoo, S. K., Prabha, S., Bargar, T. & Labhasetwar, V. Fluorescence and electron microscopy probes for cellular and tissue uptake of poly(d,l-lactide-co-glycolide) nanoparticles. *Int. J. Pharm.* **262,** 1–11 (2003).

98. Kreuter, J. *et al.* Apolipoprotein-mediated transport of nanoparticle-bound drugs across the blood-brain barrier. *J. Drug Target.* **10,** 317–25 (2002).

99. Moghimi, S., Hunter, A. & Murray, J. Long-circulating and target-specific nanoparticles: theory to practice. *Pharmacol. Rev.* **53,** 283–318 (2001).

100. Hirsch, L. & Stafford, R. Nanoshell-mediated near-infrared thermal therapy of tumors under magnetic resonance guidance. *Proc. Natl. Acad. Sci.* **100,** 13549–13554 (2003).

101. Huang, X. & El-Sayed, I. Cancer cell imaging and photothermal therapy in the near-infrared region by using gold nanorods. *J. Am. Chem. Soc.* **128,** 2115–2120 (2006).

102. Åkerman, M. Nanocrystal targeting in vivo. *Proc. Natl. Acad. Sci.* **99,** 1840–54 (2002).

103. Blecher, K., Nasir, A. & Friedman, A. The growing role of nanotechnology in combating infectious disease. *Virulence* **2,** 395–401 (2011).

104. Abraham, A., Kannangai, R. & Sridharan, G. Nanotechnology: a new frontier in virus detection in clinical practice. *Indian J. Med. Microbiol.* **26,** 297–301 (2008).

105. Glynou, K., Ioannou, P. C., Christopoulos, T. K. & Syriopoulou, V. Oligonucleotide-functionalized gold nanoparticles as probes in a dry-reagent strip biosensor for DNA analysis by hybridization. *Anal. Chem.* **75,** 4155–4160 (2003).

106. Nagatani, N. *et al.* Gold nanoparticle-based novel enhancement method for the development of highly sensitive immunochromatographic test strips. *Sci. Technol. Adv. Mater.* **7,** 270–275 (2006).

107. Ratsimbasoa, A. Which malaria rapid test for Madagascar? Field and laboratory evaluation of three tests and expert microscopy of samples from suspected malaria patients in Madagascar. *Am. J. Trop. Med. Hyg.* **76,** 481–485 (2007).

108. Rohrman, B., Leautaud, V., Molyneux, E. & Richards-Kortum, R. R. A lateral flow assay for quantitative detection of amplified HIV-1 RNA. *PLoS One* **7,** e45611 (2012).

109. Goryacheva, I. Y., Lenain, P. & De Saeger, S. Nanosized labels for rapid immunotests. *Trends Anal. Chem.* **46,** 30–43 (2013).

110. Thanh, N. & Rosenzweig, Z. Development of an aggregation-based immunoassay for anti-protein A using gold nanoparticles. *Anal. Chem.* **74,** 1624–1628 (2002).

111. Wang, H. *et al.* A piezoelectric immunoagglutination assay for Toxoplasma gondii antibodies using gold nanoparticles. *Biosens. Bioelectron.* **19,** 701–709 (2004).

112. Gasparyan, V. Gold and silver nanoparticles in bioassay, cell visualization and therapy. *Curr. Clin. Pharmacol.* **4,** 159–163 (2009).

113. Hirsch, L., Jackson, J. & Lee, A. A whole blood immunoassay using gold nanoshells. *Anal. Chem.* **1892,** 888–892 (2003).

114. Clark, I. & Alleva, L. Pathogenesis of malaria and clinically similar conditions. *Clin. Microbiol. Rev.* **17,** 509–539 (2004).

115. Kyabayinze, D. & Karamagi, C. Multiplicity of Plasmodium falciparum infection predicts antimalarial treatment outcome in Ugandan children. *Afr. Health Sci.* **8,** 8–13 (2009).

116. Parkin, N. & Schapiro, J. Antiretroviral drug resistance in non-subtype B HIV-1, HIV-2 and SIV. *Antivir. Ther.* **9,** 3–12 (2004).

117. Wilson, R., Cossins, A. R. & Spiller, D. G. Encoded microcarriers for high-throughput multiplexed detection. *Angew. Chemie* **45,** 6104–17 (2006).

118. Han, M., Gao, X., Su, J. & Nie, S. Quantum-dot-tagged microbeads for multiplexed optical coding of biomolecules. *Nat. Biotechnol.* **19,** 6104–17 (2001).

119. Fournier-Bidoz, S. *et al.* Facile and rapid one-step mass preparation of quantum-dot barcodes. *Angew. Chemie* **47,** 5577–81 (2008).

120. Klostranec, J., Xiang, Q., Farcas, G. & Lee, J. Convergence of quantum dot barcodes with microfluidics and signal processing for multiplexed high-throughput infectious disease diagnostics. *Nano Lett.* **7,** 2812–2818 (2007).

121. Giri, S., Sykes, E., Jennings, T. & Chan, W. Rapid screening of genetic biomarkers of infectious agents using quantum dot barcodes. *ACS Nano* **5,** 1580–1587 (2011).

122. Gao, Y., Lam, A. & Chan, W. Automating quantum dot barcode assays using microfluidics and magnetism for the development of a point-of-care device. *ACS Appl. Mater. Interfaces* **5,** 2853−2860 (2013).

123. Ming, K., Kim, J., Biondi, M., Syed, A. & Chen, K. Integrated quantum dot barcode smartphone optical device for wireless multiplexed diagnosis of infected patients. *ACS Nano* **9,** 3060–3074 (2015).

124. Amendola, A. *et al.* Ability of two commercially available assays (Abbott RealTime HIV-1 and Roche Cobas AmpliPrep/Cobas TaqMan HIV-1 Version 2.0) to quantify low HIV-1 RNA Levels (<1,000 copies/milliliter): comparison with clinical samples and NIBSC working reagent for nucle. *J. Clin. Microbiol.* **52,** 2019–26 (2014).

125. Wang, J., Liu, G. & Jan, M. Ultrasensitive electrical biosensing of proteins and DNA: carbon-nanotube derived amplification of the recognition and transduction events. *J. Am. Chem. Soc.* **126,** 3010–3011 (2004).

126. Fanjul-Bolado, P., González-García, M. B. & Costa-García, A. Flow screen-printed amperometric detection of p-nitrophenol in alkaline phosphatase-based assays. *Anal. Bioanal. Chem.* **385,** 1202–8 (2006).

127. Haque, A., Park, H., Sung, D. & Jon, S. An electrochemically reduced graphene oxide-based electrochemical immunosensing platform for ultrasensitive antigen detection. *Anal. Chem.* **84,** 1871−1878 (2012).

128. Malhotra, R., Patel, V., Vaqué, J. P., Gutkind, J. S. & Rusling, J. F. Ultrasensitive electrochemical immunosensor for oral cancer biomarker IL-6 using carbon nanotube forest electrodes and multilabel amplification. *Anal. Chem.* **82,** 3118–23 (2010).

129. Akanda, M., Aziz, M. & Jo, K. Optimization of phosphatase-and redox cycling-based immunosensors and its application to ultrasensitive detection of troponin I. *Anal. Chem.* **83,** 3926–3933 (2011).

130. Hu, C., Yang, D., Xu, K., Cao, H. & Wu, B. Ag@ BSA core/shell microspheres as an electrochemical interface for sensitive detection of urinary retinal-binding protein. *Anal. Chem.* **84,** 10324–10331 (2012).

131. Bard, A. J. & Faulkner, L. R. *Electrochemical methods: fundamentals and applications. 2nd edition.* 156–157 (2001).

132. Berthold Technologies. <www.berthold.com>

133. Pine Instrument Company. <www.pineinstrument.com>

134. Chikkaveeraiah, B. V, Bhirde, A. A., Morgan, N. Y., Eden, H. S. & Chen, X. Electrochemical immunosensors for detection of cancer protein biomarkers. *ACS Nano* **6,** 6546–61 (2012).

135. Sage, A. T., Besant, J. D., Lam, B., Sargent, E. H. & Kelley, S. O. Ultrasensitive electrochemical biomolecular detection using nanostructured microelectrodes. *Acc. Chem. Res.* **47,** 2417–2425 (2014).

136. Rusling, J. F., Kumar, C. V, Gutkind, J. S. & Patel, V. Measurement of biomarker proteins for point-of-care early detection and monitoring of cancer. *Analyst* **135,** 2496–511 (2010).

137. Newman, J. D. & Turner, A. P. F. Home blood glucose biosensors: a commercial perspective. *Biosens. Bioelectron.* **20,** 2435–53 (2005).

138. Grieshaber, D., MacKenzie, R., Voeroes, J. & Reimhult, E. Electrochemical biosensors-sensor principles and architectures. *Sensors* **8,** 1400–1458 (2008).

139. Wang, J. Nanomaterial-based electrochemical biosensors. *Analyst* **130,** 421 (2005).

140. Wang, J. Electrochemical glucose biosensors. *Chem. Rev.* **108,** 814–825 (2008).

141. Ngoepe, M. *et al.* Integration of biosensors and drug delivery technologies for early detection and chronic management of illness. *Sensors* **13,** 7680–7713 (2013).

142. Wei, D., Bailey, M. J., Andrew, P. & Ryhänen, T. Electrochemical biosensors at the nanoscale. *Lab Chip* **9,** 2123–31 (2009).

143. Zhang, G. *Nanoscale surface modification for enhanced biosensing: a journey toward better glucose monitoring*. 8 (2015).

144. Elfström, N., Juhasz, R. & Sychugov, I. Surface charge sensitivity of silicon nanowires: Size dependence. *Nano Lett.* **7,** 2608–2612 (2007).

145. Bhimji, A., Zaragoza, A., Live, L. S. & Kelley, S. O. Electrochemical enzyme-linked immunosorbent assay featuring proximal reagent generation: detection of human immunodeficiency virus antibodies in clinical samples. *Anal. Chem.* **85,** 6813–9 (2013).

146. Vallée-Bélisle, A., Ricci, F. & Uzawa, T. Bioelectrochemical switches for the quantitative detection of antibodies directly in whole blood. *J. Am. Chem. Soc.* **134,** 15197–15200 (2012).

147. Gasparac, R. & Taft, B. Ultrasensitive electrocatalytic DNA detection at two-and three-dimensional nanoelectrodes. *J. Am. Chem. Soc.* **126,** 12270–12271 (2004).

148. Drummond, T. G., Hill, M. G. & Barton, J. K. Electrochemical DNA sensors. *Nat. Biotechnol.* **21,** 1192–9 (2003).

149. Lin, M. *et al.* Target-responsive, DNA nanostructure-based E-DNA sensor for microRNA analysis. *Anal. Chem.* **86,** 2285–2288 (2014).

150. Kim, J. *et al.* Non-invasive mouthguard biosensor for continuous salivary monitoring of metabolites. *Analyst* **139,** 1632–6 (2014).

151. Hason, S., Stepankova, S. & Kourilova, A. Simultaneous electrochemical monitoring of metabolites related to the xanthine oxidase pathway using a grinded carbon electrode. *Anal. Chem.* **81,** 4302–4307 (2009).

152. Ferguson, B. & Hoggarth, D. Real-time, aptamer-based tracking of circulating therapeutic agents in living animals. *Sci. Transl. Med.* **5,** 213 (2013).

153. Veloso, A. J. *et al.* Miniaturized electrochemical system for cholinesterase inhibitor detection. *Anal. Chim. Acta* **774,** 73–8 (2013).

154. Viswanathan, S., Wu, L., Huang, M. & Ho, J. A. Electrochemical immunosensor for cholera toxin using liposomes and poly (3, 4-ethylenedioxythiophene) -coated carbon nanotubes. *Anal. Chem.* **78,** 1115–1121 (2006).

155. Shen, J., Li, Y., Gu, H., Xia, F. & Zuo, X. Recent development of sandwich assay based on the nanobiotechnologies for proteins, nucleic acids, small molecules, and ions. *Chem. Rev.* **114,** 7631–7677 (2014).

156. Tang, D., Su, B., Tang, J., Ren, J. & Chen, G. Nanoparticle-based sandwich electrochemical immunoassay for carbohydrate antigen 125 with signal enhancement using enzyme-coated nanometer-sized enzyme-doped silica beads. *Anal. Chem.* **82,** 1527–1534 (2010).

157. Ding, C., Zhang, Q., Lin, J.-M. & Zhang, S. Electrochemical detection of DNA hybridization based on bio-bar code method. *Biosens. Bioelectron.* **24,** 3140–3143 (2009).

158. Park, S.-J., Taton, T. A. & Mirkin, C. Array-based electrical detection of DNA with nanoparticle probes. *Science* **295,** 1503–6 (2002).

159. Das, J. & Kelley, S. O. Protein detection using arrayed microsensor chips: tuning sensor footprint to achieve ultrasensitive readout of CA-125 in serum and whole blood. *Anal. Chem.* **83,** 1167–72 (2011).

160. Lapierre, M., O'Keefe, M., Taft, B. J. & Kelley, S. O. Electrocatalytic detection of pathogenic DNA sequences and antibiotic resistance markers. *Anal. Chem.* **75,** 6327–33 (2003).

161. Wang, J. Carbon-nanotube based electrochemical biosensors: a review. *Electroanalysis* **17,** 7–14 (2005).

162. Wanekaya, A. K., Chen, W., Myung, N. V. & Mulchandani, A. Nanowire-based electrochemical biosensors. *Electroanalysis* **18,** 533–550 (2006).

163. Luo, X., Morrin, A., Killard, A. J. & Smyth, M. R. Application of nanoparticles in electrochemical sensors and biosensors. *Electroanalysis* **18,** 319–326 (2006).

164. Zhang, J. *et al.* Sequence-specific detection of femtomolar DNA via a chronocoulometric DNA sensor (CDS): effects of nanoparticle-mediated amplification and nanoscale control of DNA assembly at electrodes. *J. Am. Chem. Soc.* **128,** 8575–80 (2006).

165. Chen, A. & Chatterjee, S. Nanomaterials based electrochemical sensors for biomedical applications. *Chem. Soc. Rev.* **42,** 5425–38 (2013).

166. Vestergaard, M., Kerman, K. & Tamiya, E. An overview of label-free electrochemical protein sensors. *Sensors* **7,** 3442–3458 (2007).

167. Munge, B. & Coffey, A. Nanostructured immunosensor for attomolar detection of cancer biomarker interleukin-8 using massively labeled superparamagnetic particles. *Angew. Chemie Int. Ed.* **50,** 7915–7918 (2011).

168. Munge, B., Liu, G., Collins, G. & Wang, J. Multiple enzyme layers on carbon nanotubes for electrochemical detection down to 80 DNA copies. *Anal. Chem.* **77,** 4662–4666 (2005).

169. Wei, F. *et al.* A bio-abiotic interface constructed by nanoscale DNA-dendrimer and conducting polymer for ultra-sensitive bio-molecular diagnosis. *Small* **5,** 1784–1790 (2010).

170. Tang, C. K., Vaze, A. & Rusling, J. F. Fabrication of immunosensor microwell arrays from gold compact discs for detection of cancer biomarker proteins. *Lab Chip* **12,** 281–286 (2012).

171. Rusling, J., Kumar, C., Gutkind, J. & Patel, V. Measurement of biomarker proteins for point-of-care early detection and monitoring of cancer. *Analyst* **135,** 2496–2511 (2010).

172. Crosbie, P. J., Shah, R., Summers, Y., Dive, C. & Blackhall, F. Prognostic and predictive biomarkers in early stage NSCLC: CTCs and serum/plasma markers. *Transl. lung cancer Res.* **2,** 382–97 (2013).

173. Punglia, R. S., D'Amico, A. V, Catalona, W. J., Roehl, K. & Kuntz, K. M. Effect of verification bias on screening for prostate cancer by measurement of prostate-specific antigen. *N. Engl. J. Med.* **349,** 335–42 (2003).

174. Okuno, J. *et al.* Label-free immunosensor for prostate-specific antigen based on single-walled carbon nanotube array-modified microelectrodes. *Biosens. Bioelectron.* **22,** 2377–2381 (2007).

175. Wei, Q. *et al.* A novel label-free electrochemical immunosensor based on graphene and thionine nanocomposite. *Sensors Actuators B Chem.* **149,** 314–318 (2010).

176. Jiang, Z. *et al.* A label-free electrochemical immunosensor based on poly(thionine)-SDS nanocomposites for CA19-9 detection. *Anal. methods* **7,** 4508–4513 (2015).

177. Zheng, G., Patolsky, F., Cui, Y., Wang, W. U. & Lieber, C. M. Multiplexed electrical detection of cancer markers with nanowire sensor arrays. *Nat. Biotechnol.* **23,** 1294–301 (2005).

178. Tran, H. V *et al.* Label-free and reagentless electrochemical detection of microRNAs using a conducting polymer nanostructured by carbon nanotubes: application to prostate cancer biomarker miR-141. *Biosens. Bioelectron.* **49,** 164–9 (2013).

179. Polanski, M. & Anderson, N. A list of candidate cancer biomarkers for targeted proteomics. *Biomark. Insights* **2,** 1–48 (2006).

180. Makawita, S. & Diamandis, E. P. The bottleneck in the cancer biomarker pipeline and protein quantification through mass spectrometry-based approaches: current strategies for candidate verification. *Clin. Chem.* **56,** 212–22 (2010).

181. Zhu, C. S. *et al.* A framework for evaluating biomarkers for early detection: validation of biomarker panels for ovarian cancer. *Cancer Prev. Res.* **4,** 375–83 (2011).

182. Drucker, E. & Krapfenbauer, K. Pitfalls and limitations in translation from biomarker discovery to clinical utility in predictive and personalised medicine. *EPMA J.* **4,** 7 (2013).

183. Anderson, N. L. *et al.* The human plasma proteome. *Mol. Cell. Proteomics* **3,** 375–83 (2004).

184. Chikkaveeraiah, B. V, Mani, V., Patel, V., Gutkind, J. S. & Rusling, J. F. Microfluidic electrochemical immunoarray for ultrasensitive detection of two cancer biomarker proteins in serum. *Biosens. Bioelectron.* **26,** 4477–83 (2011).

185. Malhotra, R. & Patel, V. Ultrasensitive detection of cancer biomarkers in the clinic by use of a nanostructured microfluidic array. *Anal. Chem.* **84,** 6249–6255 (2012).

186. Fragoso, A. *et al.* Integrated microfluidic platform for the electrochemical detection of breast cancer markers in patient serum samples. *Lab Chip* **11,** 625–631 (2011).

187. Chen, J. *et al.* Development of an electrochemical sensing technique for rapid genotyping of hepatitis B virus. *Sensors* **14,** 5611–21 (2014).

188. Yao, F., Zhang, Y., Wei, Y. & Kang, X. A rapid and sensitive detection of HBV DNA using a nanopore sensor. *Chem. Commun.* **50,** 13853–13856 (2014).

189. Park, J.-Y. *et al.* Label-free impedimetric sensor for a ribonucleic acid oligomer specific to hepatitis C virus at a self-assembled monolayer-covered electrode. *Anal. Chem.* **82,** 8342–8348 (2010).

190. Liu, S., Wu, P., Li, W., Zhang, H. & Cai, C. Ultrasensitive and selective electrochemical identification of hepatitis C virus genotype 1b based on specific endonuclease combined with gold nanoparticles signal amplification. *Anal. Chem.* **83,** 4752–4758 (2011).

191. Zheng, L. *et al.* A sandwich HIV p24 amperometric immunosensor based on a direct gold electroplating-modified electrode. *Molecules* **17,** 5988–6000 (2012).

192. Wang, J. *et al.* DNA electrochemical biosensor for the detection of short DNA sequences related to the human immunodeficiency virus. *Anal. Chem.* **68,** 2629–2634 (1996).

193. Rodrigo, M. & Heger, Z. HIV Biosensors–The potential of the electrochemical way. *Int. J. Electrochem. Sci.* **9,** 3449–3457 (2014).

194. Nidzworski, D., Pranszke, P., Grudniewska, M., Król, E. & Gromadzka, B. Universal biosensor for detection of influenza virus. *Biosens. Bioelectron.* **59,** 239–42 (2014).

195. Xie, Z. *et al.* Ultrasensitive electrochemical immunoassay for avian influenza subtype H5 using nanocomposite. *PLoS One* **9,** e94685 (2014).

196. Chen, X. *et al.* Enzyme-free and label-free ultrasensitive electrochemical detection of human immunodeficiency virus DNA in biological samples based on long-range self-assembled DNA nanostructures. *Anal. methods* **84,** 8277–8283 (2012).

Chapter 2.

Materials and Methods

2.1 Chemicals and reagents

Cholera toxin subunit B (CT), ferrocenecarboxylic acid (FCA), ethanol, and ethylenediaminetetraacetic acid (EDTA) were purchased from Sigma-Aldrich (St. Louis, MO). Anti-cholera toxin subunit B antibodies (Abs) and alkaline phosphatase (ALP) conjugated Ab were obtained from Abnova (Taipei, Taiwan). The BluePhos phosphatase substrate system was purchased from KPL (Gaithersburg, MD) and p-aminophenylphosphate (pAPP) was acquired from Gold Biotechnology, Inc. (St. Louis, MO). Hydrogen tetrachloroaurate(III) trihydrate ($HAuCl_4$), sodium dodecyl sulphate (SDS), acetic acid (99%), bovine serum albumin (BSA), Tween-20, phosphate buffered saline (PBS), and Tris base were obtained from Fisher Scientific (Pittsburgh, PA).

Shipley 1813 photoresist, MF-319 developer, LOR-2A resist, hexamethyldisilazane (HDMS), Microposit 1165, and SU-8 were procured from MicroChem Corp. (Westborough, MA) and Transetch-N was obtained from Transene Company, Inc. (Danvers, MA). Hydrogen peroxide (27%), ammonium hydroxide (28%), 1H,1H,2H,2H-perfluorodecyltrichlorosilane (FDTS) (96%) and n-heptane (99%) were purchased from Alfa Aesar (Ward Hill, MA). Polydimethylsiloxane (PDMS) Sylgard 184 silicone elastomer kit was purchased from Dow Corning (Midland, MI). Acetone (99.5%) and sulfuric acid (96%) were purchased from J.T. Baker. Epon^{TM} resin 828 and Epikure 3140 curing agent was provided by Miller-Stephenson Chemical Co. Inc. (Danbury, CT).

2.2 Fabrication of nanocoaxial arrays

Fabrication of nanocoaxial arrays used was generously completed by colleague Dr. Binod Rizal in collaboration with the laboratory of Dr. Michael J. Naughton.

2.2.1 Nanoimprint lithography

Silicon nanopillar (SiNP) arrays were previously prepared to be used as imprint masters (Rizal et al., 2013). The SiNP arrays consisted of pillars with 2 μm height and 200 nm in diameter in a hexagonal close-packed array of 1.3 μm periodicity/pitch. Pillars were contained within an array area of 10 × 20 mm^2, with a density of ~10^6 pillars/mm^2. To aid in imprinting, a release coating was applied to the SiNP master arrays; the SiNP arrays were immersed in a solution consisting of FDTS and n-heptane in the ratio of 1:1000 (v/v), and then subsequently transferred to acetone for 5 min. Finally, the master arrays were baked at 110°C for 5 min on a hot plate.

Molds were made from a master array with polydimethylsiloxane (PDMS) which was mixed in the ratio of 10:1 (w/w) with its curing agent and degassed in a bell-jar desiccator connected to a vacuum pump for 30 min. The PDMS was then poured onto the SiNP master array, cured at room temperature for 12 h, and baked for 1 h at 90°C. The PDMS mold was peeled off of the master, and treated with the same release coating as described above prior to imprinting.

A thin film of SU-8 2002 was spin-coated on a piranha-cleaned Si wafer at 500 rpm with an acceleration of 110 rpm/s for 6 s, followed by 3000 rpm at 550 rpm/s for 36 s. To

remove any residual solvent, the substrate was baked at 65°C for 1 min and then 95°C for at 3 min. The film was cooled to room temperature and then the PDMS mold was placed on top of it. To ensure conformal contact between the mold and the film, a pressure of ~10^5 Pa was applied between the SU-8 film and PDMS mold using an in-house constructed clamping apparatus. The PDMS mold and SU-8 were held in contact for 5 min at 95°C and then exposed to UV light in a mask aligner (MA6, Karl Suss, Denmark) at 12 mW/cm^2 for 90 s. A post-exposure bake for 5 min at 95°C was then completed. The sample was allowed to cool to room temperature and then the PDMS mold was peeled off, releasing the SU-8 nanopillar array which will form the base starting substrate in the fabrication of the nanocoax.

2.2.2 Fabrication of hollow cavity nanocoax arrays

A thin film of Au (~125 nm) was deposited onto the SU-8 nanopillar array via sputter deposition (AJA International, Scituate, MA) with 250 W DC power and 0.75 nm/s deposition rate. Atomic layer deposition (Savannah S100, Cambridge Nanotech, Waltham, MA) was then used to deposit ~200 nm Al_2O_3 at 200°C, followed by a sputter deposition of Cr (~150 nm) with 200 W DC power and 0.1 nm/s deposition rate. A layer of SU-8 was spin-coated on top of the coaxial array to provide mechanical support and was cured by UV exposure (12 mW/cm^2; 90 s), followed by a hard bake at 200°C for 1 h. A mechanical polisher (Vibromet 2, Buehler) was used to remove the top part of the outer Cr of the coax array using an alumina slurry for 2.5 h. This mechanical decapitation of the coax exposed the Al_2O_3 in the coaxes' annuli; the annuli cavities were selectively etched at room temperature with Transetch-N to a time-controlled depth of approximately

500 nm, at a rate of ~20 nm/h. Nanocoaxial arrays were contained within an area of 1.8 mm^2, with a density of ~10^6 pillars/mm^2.

2.3 Fabrication of dendrites

2.3.1 Preparation of 2D and 3D substrates

Planar silicon wafers (University Wafers, Boston, MA) were sonicated in acetone for 5 min in preparation for metal deposition. A thin adhesion layer of Ti (~10 nm) was deposited onto the Si via sputter deposition, followed by ~125 nm of Au. The planar Au substrates were cut by hand with a diamond scribe into ~ 2x2 cm^2 sized samples.

Si wafers containing pillar arrays were pre-diced into 30 x 16 mm^2 substrates using a DAD3220 dicing saw (Disco, USA). Each of these areas contained a 10 x 20 mm^2 Si pillar array. These Si pillar substrates were subject to the same metal deposition steps as described above for the planar substrates.

2.3.2 Photolithographically-patterned substrates

Substrates were photolithographically-patterned in order to fabricate uniform and electrically-isolated regions for dendritic growth. Si wafers containing pillar arrays were diced into the same dimensions as described above in Section 2.3.1. The substrates were cleaned with 5 min sonication in acetone, rinsed with isopropanol (IPA) and with dH_2O, and then baked at 200°C for 5 min. HDMS was spin-coated on the substrate at 3000 rpm for 45 s, followed by LOR-2A at the same parameters. The substrate was then baked at 150°C for 7 min. The photoresist Shipley 1813 was spin-coated onto the substrate at a ramp of 500 rpm for 5 s, followed by a spin of 4000 rpm for 45 s. The substrate was

baked for 1 min at 105°C then allowed to cool to room temperature. The substrate was then held in contact with a mask and exposed to UV light in the mask aligner for 6.5 s. After exposure, the substrate was developed for 90 s in MF-319, rinsed with dH_2O for 1 min, and nitrogen dried.

A thin adhesion layer of ~10 nm Ti was deposited via sputter deposition, immediately followed by ~110 nm Au. To lift-off photoresist, the substrate was immersed in Microposit 1165 remover at 60°C overnight, followed by 5 s sonication. The substrate was then sonicated in acetone for 5 min, rinsed with IPA and nitrogen dried.

In order to protect the address lines, a second round of photolithography was performed as described above, except the LOR-2A step was excluded. UV exposure was performed with the same parameters; a second mask was used that exposed only the circular regions and the electrode pads. Substrate patterning was completed after developing with MF-319 (image of completed substrate shown below).

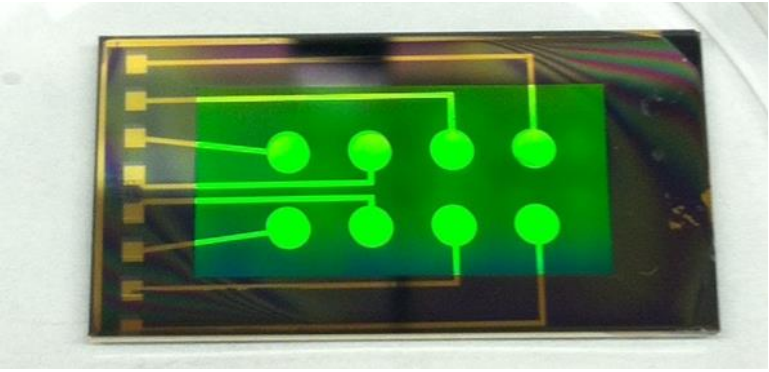

Figure 2.3.1. Completed photolithographically-patterned chip for dendritic growth.

2.3.3 Directed electrochemical nanowire assembly

Directed electrochemical nanowire assembly (DENA) was carried out with a waveform generator (Agilent 33600A Series, Santa Clara, CA) using a two-electrode system. Waveform was monitored by an oscilloscope (Agilent MSO-X 3024A) during electrochemical deposition. The Au substrate onto which dendritic growth was desired served as the working electrode. A coiled Pt wire or a planar Au chip served as the counter electrode. A square waveform was run with a frequency of 30 MHz, an amplitude of 5 V_{pp}, an offset of -1.25 V_o, a phase of 0, and a duty cycle of 50% in the presence of 30 mM $HAuCl_4$. The growth time was varied.

2.4 Characterization of nanostructures

2.4.1 Scanning electron microscopy

Structural integrity of all fabricated nanostructures was confirmed via scanning electron microscopy (SEM). SEM images of the nanocoaxial arrays, and intermittent steps during fabrication, were taken using a JEOL JSM-7001F SEM. Focused ion beam (FIB) milling to obtain cross-sectional profile images of the coax was carried out using a JEOL JIB-4500 FIB with the assistance of Dr. Gregory McMahon. SEM images of dendritic structures were taken using a JEOL JCM-6000 NeoScope benchtop SEM.

2.4.2 Resistance measurements

Electrical integrity of nanocoaxial arrays was confirmed using a 610B Electrometer (Kiethley Instruments, Cleveland, OH) to measure resistance between the working

electrode and the counter electrode of each array. For quality control, only devices with a resistance $> 10^6\ \Omega$ were used, as devices with lower resistances were subject to shorting.

2.4.3 Ferrocenecarboxylic acid redox assay

To confirm electrochemical sensing capabilities of each device, all nanostructures were tested with the redox species FCA. Differential pulse voltammetry (DPV) was performed in the presence of 1 mM FCA in PBS, pH 7.4 with the potential range of 0 V to 0.5 V, a potential step of 2 mV, a pulse amplitude of 50 mV, a pulse width of 50 ms, a pulse sample period of 100 ms, and an equilibrium time of 10 s.

2.4.4 ALP titrations

Dose titrations of ALP were electrochemically measured on each nanostructure for proof-of-concept as an electrochemical sensor. Serial dilutions of ALP in TBS (50 mM Tris, 1 mM $MgCl_2$, pH 9.0) were incubated with 1 mM of the enzymatic substrate pAPP in TBS for 30 min at room temperature in the dark. The reaction was stopped with 40 µl of 50 mM EDTA in TBS. Approximately 100 µl of each dilution was subsequently pipetted onto the nanostructure array for electrochemical measurements. ALP activity was analyzed via DPV; measurements were performed using a potential range of -0.5 V to 0.4 V, a potential step of 2 mV, a pulse amplitude of 50 mV, a pulse width of 50 ms, a pulse sample period of 100 ms, and an equilibrium time of 10 s.

2.5 Electrochemical analysis

2.5.1 Well attachment

Wells were attached to all substrates prior to electrochemical sensing (to contain solution during electrochemical analysis) using one of two epoxy systems: SU-8 3025 photoresist or the Epon™ resin 828/Epikure 3140 two-part epoxy system. The choice of epoxy system was solely based on reagent availability; both systems were equally durable and chemically stable for our purposes. Wells were fabricated from the base of pipette tips (Eppendorf, USA); pipette tips were decapitated with a razor blade to give a well height of approximately 1.5 cm. The base of the tip (*i.e.* non-severed end) was then attached to the substrate, giving a known and uniform well base area of 12.56 mm^2 (tip base inner diameter = 4 mm).

Prior to well attachment, substrates were either chemically treated with the standard RCA clean or were cleaned with UV/ozone, depending on substrate type. Substrates that were coated solely in metal (e.g. Au planar or Au pillar substrates) were RCA cleaned. Substrates containing a photoresist coating (e.g. nanocoaxial arrays, photolithographically patterned chips for dendrites) were treated with UV/ozone, as RCA clean removed the photoresist. For RCA clean, a 1:1:5 mixture of ammonium hydroxide (28%), hydrogen peroxide (27%), and dH_2O were heated to 80°C. Substrates were submerged for 10 min, then immediately placed into a beaker of dH_2O and rinsed three times. Substrates were then rinsed with 200 proof ethanol and air dried. Substrates that were cleaned with UV/ozone were treated for 20 min with a UV/Ozone ProCleaner Plus (BioForce Nanosciences, USA). Wells were immediately attached post cleaning.

To attach wells with SU-8 photoresist, SU-8 was applied to the base of the well and the well was placed onto the substrate. The substrate was then placed under UV light for 10 min and baked at 65°C for 10 min. An appreciable second layer of SU-8 was applied to the outside of the well base to prevent any leaks. The substrate underwent a second 10 min UV light exposure and 10 min bake at 65°C, followed by a final post bake at 90°C for 20 min.

Additionally, wells were attached with the Epon™ resin 828/Epikure 3140 two-part epoxy system. Epon 828 and Epikure 3140 were mixed in a 1:1 (w/w) ratio and applied to the base of the well. The well was placed on the substrate and then air dried overnight (~12 h).

2.5.2 Nanocoax

All electrochemical readouts of nanocoaxial arrays were carried out on a Reference 600 potentiostat (Gamry Instruments, Warminster, PA) using a three-electrode system. An external Ag/AgCl wire served as the reference electrode. The outer Cr of the nanocoaxes in the array served as the counter electrode and the inner Au of the nanocoaxes functioned as the working electrode. Electrochemical analysis of the nanocoaxial arrays was performed with DPV.

2.5.3 Dendrites

Electrochemical readouts were performed on a Reference 600 potentiostat or on a Reference 1000 potentiostat (Gamry Instruments, Warminster, PA) with a three-electrode

system. An external Ag/AgCl wire served as the reference electrode and an external Pt wire functioned as the counter electrode. The Au dendritic array served as the working electrode. DPV was used as the method for electrochemical analysis of dendritic arrays.

2.6 Enzyme-linked immunosorbent assay (ELISA)

2.6.1 Electrochemical ELISA

The wells of a 96-well plate were coated with 1 µg/ml of anti-cholera toxin Ab (anti-CT Ab) in 0.1 M $NaHCO_3$, pH 9.6 for 2 h at room temperature. The solution was removed from the plate and the wells were washed three times with TBST (0.05% Tween-20, 50 mM Tris, 150 mM NaCl, pH 7.4); the wells were blocked with 5% BSA in TBST overnight at 4°C. Several different concentrations of CT antigen in 2% BSA/TBST were added to individual wells and incubated for 1 h at room temperature. The plate was then washed three times with TBST. A second anti-CT Ab was added to each well at a concentration of 50 ng/ml in 2% BSA/TBST for 1 h at room temperature. The plate was washed three times with TBST. Anti-mouse IgG alkaline phosphatase labeled Ab was added to each well at a dilution of 2.7 µg/ml in 2% BSA/TBST for 1 h at room temperature. The plate was washed six times with TBST. Lastly, the wells were incubated with 1 mM pAPP in TBS reaction buffer (50 mM Tris, 1 mM $MgCl_2$, pH 9.0) at room temperature in the dark. The reaction was stopped after 30 min by adding 40 µl of 50 mM EDTA in TBS to each well. Approximately 100 µl of supernatant from each of the wells was then pipetted onto the nanostructure array for electrochemical measurements. Electrochemical ELISA was analyzed via DPV; measurements were performed using a potential range of -0.3 V to 0.2 V, a potential step of 2 mV, a pulse

amplitude of 50 mV, a pulse width of 50 ms, a pulse sample period of 100 ms, and an equilibrium time of 10 s.

2.6.2 Optical ELISA

Optical ELISAs were performed in the exact same manner alongside electrochemical ELISAs, except that the BluePhos phosphatase substrate system replaced pAPP in the final step of the assay. BluePhos was chosen over the traditional pNPP optical substrate due to its greater sensitivity. The reaction was stopped after 30 min by adding 40 µl of 50 mM EDTA to each well. Optical absorbance was measured spectroscopically at 600 nm on a SpectraMax M5 (Molecular Devices, Sunnyvale, CA).

2.7 Data analysis

DPV was the method used to measure electrochemical signal in the following studies. DPV is a pulsed voltammetric method that applies potential in a series of pulses superimposed over a staircase waveform. This pulsing manner prevents charging currents and is therefore beneficial in electrochemical systems. A generic potential waveform used in DPV is shown in Figure 2.7.1a. The current is sampled before and after the pulse, and the difference between these values is the displayed current measurement in the DPV. A typical resulting DPV is depicted in 2.7.1b, where the current is plotted against the potential.

Electrochemical signal was analyzed by overlaying DPV signals of varying CT concentrations and determining the peak current of each DPV. Raw DPV data was first

overlain as shown in Figure 2.7.2a in order to determine an appropriate potential at which to baseline the data. DPV signals were baselined, or subtracted to zero, at a chosen potential that resulted in a smooth, overlapping baseline for the majority of the DPV signals and did not interfere in the oxidation curve (i.e. must be baselined before the base of the curve appears). An example of baselined DPV signals is shown in Figure 2.7.2b where the raw DPV data from Figure 2.7.2a has been subtracted to zero at -0.25 V. Peak current (I_p) can now be determined for each DPV signal and subsequently plotted against their respective CT concentration to elucidate range of detection and limits of detection.

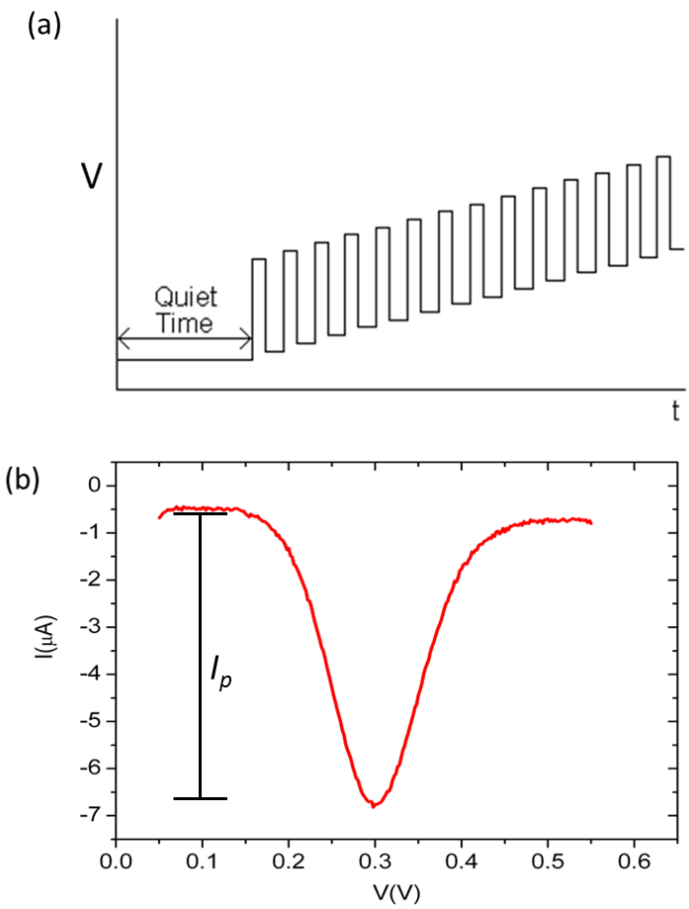

Figure 2.7.1. DPV waveform and curve. (a) Potential waveform used in DPV. Potential is pulsed in increments along a staircase waveform. X- axis: time (t); y-axis: potential (V). (b) Typical resulting DPV curve, with a peak current (I_p) occurring at 0.3 V. X-axis: potential (V); y-axis: current (I).

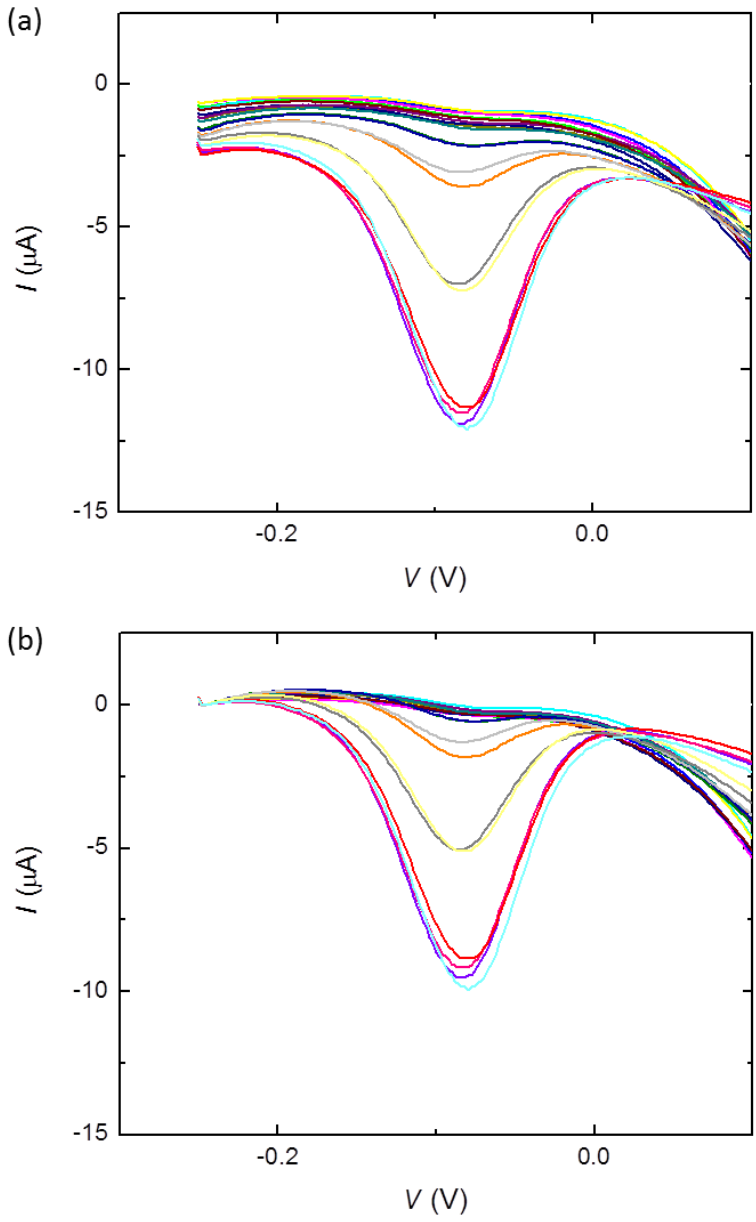

Figure 2.7.2. DPV analysis. (a) Raw DPV data for several concentrations of CT during a CT ELISA. (b) DPV signals subtracted to zero at -0.25 V to obtain a smooth, overlapping baseline in order to elucidate peak currents. X-axis: potential (*V*); y-axis: current (*I*).

Chapter 3.

Nanocoax

3.1 Introduction

Much focus has been given to ultramicroelectrodes (UMEs) over the past couple of decades as a means to increase sensitivity of electrochemical sensors. UMEs consist of electrodes with dimensions 25 μm or smaller, into the nanoscale regime. Nanogap electrodes (UMEs with a nanogap separation between them) have especially drawn attention due to several perceived advantageous properties over their macroscale counterparts. Nanogap electrodes have exhibited enhanced mass transport, decreased electric double layer capacitance (C_{dl}), and reduced solution resistance (R_s)[1–4]. The miniaturized dimensions of UMEs allow for radial diffusion and cycling of electrochemical reporter molecules between electrodes, producing a positive feedback loop and increasing signal. Additionally, small C_{dl} and R_s constants allow for short time scales that are unfeasible in macroscopic electrodes. Furthermore, exceptionally high current densities can be obtained with UMEs, whereas the currents themselves become very small, enabling improved signal-to-noise. However, a major challenge associated with UMEs is a lack of fabrication techniques that provide reproducible, detailed structures, while remaining cost-effective and allowing for high-throughput fabrication.

Previously, a novel nano-gapped UME structure, the nanocoax, was developed[5]. The nanocoax resembles a vertically oriented coaxial electrode on the nanoscale. It consists of two concentric electrodes separated by a nanogap composed of dielectric or air (Fig. 3.1.1). Due to the 3D, radial nature of the electrodes, the nanocoaxial structure can electrically interrogate higher volumes of sample within the WE-CE annulus gap over other conventional 2D and 3D vertical UMEs, leading to increased sensitivity. We have

utilized nanoimprint lithography (NIL) to form the base SU-8 pillar array with which to construct nanocoax arrays. NIL is a low-cost, rapid fabrication process that produces a large number of replicas from a single master[6]. In addition, NIL enables uniform, reproducible structures and is well-suited for 3D nanostructures such as the vertical pillar array in the nanocoax architecture.

The nanocoax previously demonstrated ultrasensitive chemical detection of volatile organic compounds[7], and exhibited nanophotonic properties as a waveguide for visible light[5,8]. Here, the nanocoax was investigated as an electrochemical biosensor in the detection of infectious disease biomarkers and compared to conventional protein detection methods. ELISAs were performed using cholera toxin (CT) as the benchmark disease biomarker and electrochemically detected utilizing pulsed voltammetry methods on nanocoaxial arrays.

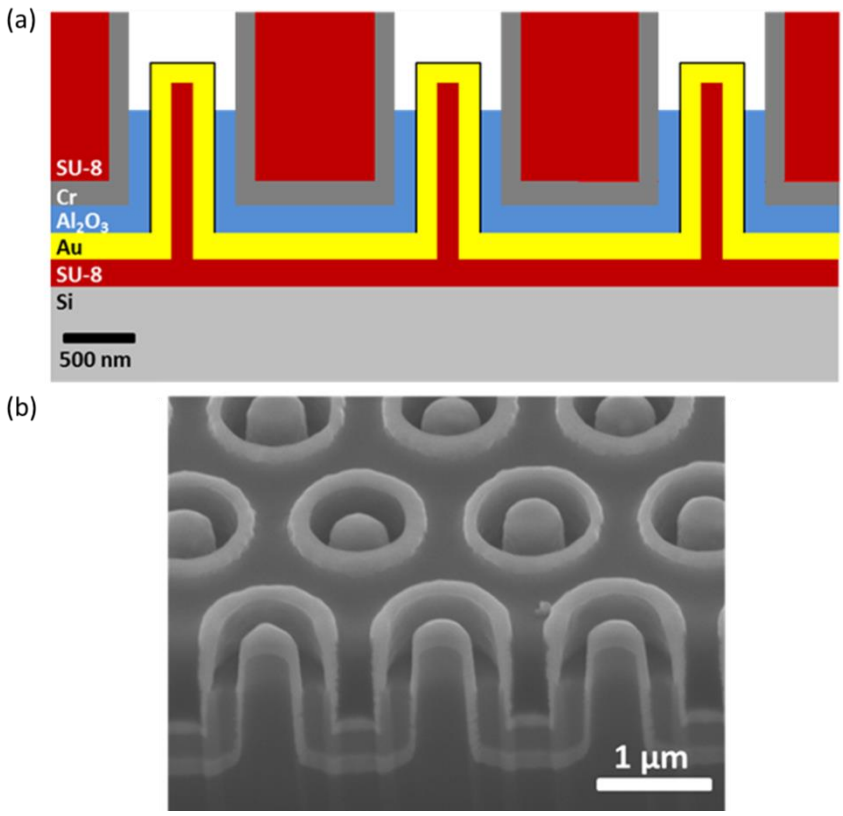

Figure 3.1.1. Structure of the nanocoax. (a) Schematic representation of a nanocoaxial array with an etched annulus. The inner Au core (shown in yellow) serves as the working electrode (WE) and the outer Cr metal (gray) serves as the counter electrode (CE). (b) SEM images of an array with 150 nm annulus thickness and 500 nm annulus depth with inner Au and outer Cr electrodes. SEM image taken at a 30° tilt.

3.2 Fabrication of nanocoaxial arrays

Nanoimprint lithography (NIL) was used to construct the base SU-8 pillar array on a silicon substrate (Fig. 3.2.1a). Previous iterations of the nanocoax utilized carbon nanotube arrays on Si as the base for nanocoax fabrication[5,7]; however non-uniformity and shorting between WE-CE were common problems with this method. Conversely, NIL allows for highly structured and mechanically stable pillar arrays.

To form the inner working electrode, the SU-8 pillars were coated with metal (Fig. 3.2.1b): an adhesion layer of ~10 nm Ti was deposited immediately followed by ~125 nm Au via sputtering. While Cr was also investigated as an inner electrode metal, all devices in this work were composed of Au inner electrodes due to the biocompatibility and electrochemical inertness of Au over a high potential range. A dielectric layer of ~200 nm Al_2O_3 was deposited with atomic layer deposition (ALD) in order to separate the inner and outer electrodes (Fig. 3.2.1c). A metal coating of ~100 nm Cr was sputtered to form the outer counter electrode (Fig. 3.2.1d). To aid in mechanical stability of the arrays, SU-8 was spin-coated to fill the gaps between each individual coax (Fig. 3.2.1e). Arrays underwent mechanical polishing in order to decapitate the outer metal layer and expose the dielectric layer (Fig. 3.2.1f). Exposed dielectric was then wet-etched to form the hollow annulus to allow for electrochemical sensing between the outer and inner electrodes (Fig. 3.2.1g).

SEMs of nanocoaxial arrays were taken to confirm proper mechanical structure (Fig. 3.2.2a). Successfully fabricated arrays consisted of nanocoaxes with 1.3 μm pitch and 2

μm height, and had nanocoax annuli that were 200 nm thick and 500 nm in depth. All arrays had a circular base area of 1.8 mm^2 as shown in Figure 3.2.2b. Each array area contained ~10^6 individual nanocoaxes electrically connected in parallel. Array areas were encapsulated within a polypropylene well using SU-8 epoxy (as described in Section 2.5.1) for reagent containment during electrochemical measurements (Fig. 3.2.2c). Additionally, gold wires were attached to electrode pads extending outside of the array area using a silver epoxy. The wires were used to connect arrays in a circuit for electrochemical measurements.

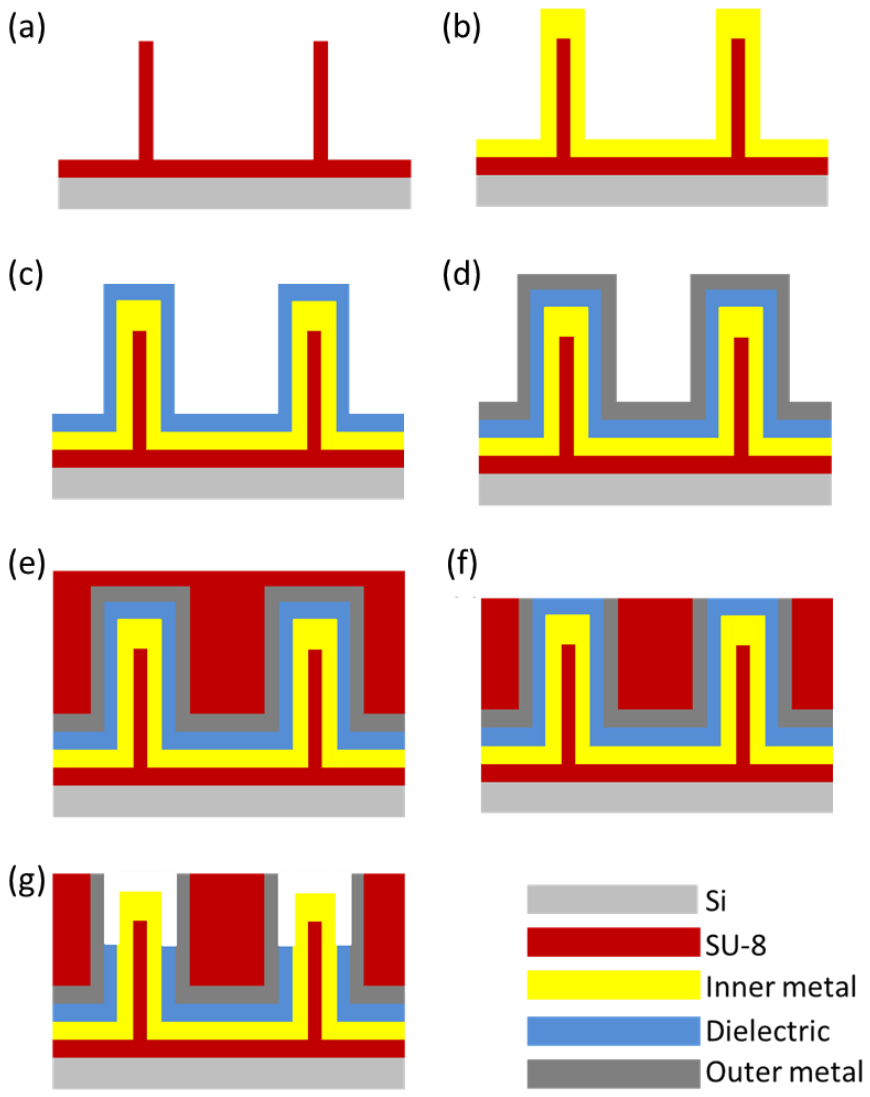

Figure 3.2.1. Fabrication scheme of nanocoaxial arrays. (a) SU-8 nanopillar arrays, (b) inner metal coating, (c) dielectric deposition, (d) outer metal coating, (e) SU-8 polymer coating, (f) mechanical polishing, and (g) dielectric wet etch.

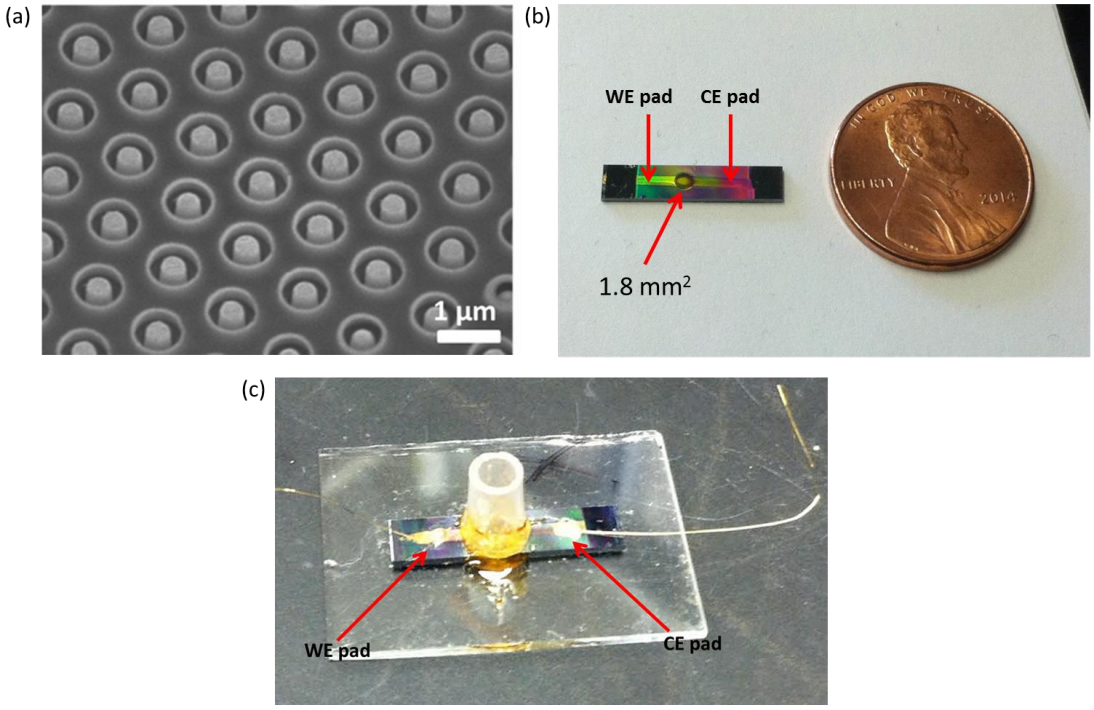

Figure 3.2.2. Fabricated nanocoaxial array. (a) SEM of a fully fabricated array (taken at a 30° tilt). (b) Chip containing a nanocoaxial array with circular base area of 1.8 mm^2, with pads for the WE and the CE extending to the ends of the chip. Penny for scale. (c) An array prepared for electrochemical measurements. A polypropylene well was attached with SU8 over the array area for reagent containment. Gold wires were attached to the WE pad and the CE pad using silver epoxy, providing a means to connect to a circuit.

3.3 Electrochemical set-up and measurements

Electrochemical measurements with nanocoaxial arrays were performed using a three-electrode system (Fig. 3.3.1a). The inner gold electrode functioned as the working electrode (WE) and the outer Cr electrode functioned as the counter electrode (CE). An external Ag/AgCl electrode served as the reference electrode (RE). Differential pulse voltammetry (DPV) was chosen as the method for electrochemical analysis due to its suppression of background current and high sensitivity[9]. A typical DPV waveform is depicted in Figure 3.3.1b for the oxidation of ferrocenecarboxylic acid (FCA). Potential is swept across a specified range as a series of pulses and the resultant current is observed. Ideally, current should remain unchanged until a redox reaction occurs, resulting in the peak at 0.3 V (as observed in Figure 3.3.1b) which is characteristic of FCA oxidation. By convention, an oxidation reaction at the WE produces an anodic current and the current is therefore designated negative. Conversely, a reduction reaction produces a positively-denoted cathodic current.

To confirm DPV as the optimal electrochemical method of choice, DPV was compared to square wave voltammetry (SWV). SWV is another commonly used pulsed voltammetry technique exhibiting high sensitivity on a fast time scale[10]. An alkaline phosphatase (ALP) dose titration was performed on a planar gold electrode (WE), with an external Pt CE and external Ag/AgCl RE. ALP converts the enzymatic substrate p-aminophenol phosphate (pAPP) into the electrochemical reporter product 4-aminophenyl (4-AP), which is subsequently detected upon reaching its oxidation potential at -100 mV. Dilutions of ALP ranging from 5 pg/ml – 0.5 μg/ml were incubated with 1 mM pAPP.

The resultant enzymatic product 4-AP was electrochemically detected at -0.1 V by either SWV (Fig. 3.3.2a) or DPV (Fig. 3.3.2b). DPV was performed with a potential range of -0.3 to 0.2 V, a pulse size of 50 mV, a pulse time of 0.05 s, a step size of 2 mV, and a sample period of 0.1 s. SWV was performed with a potential range of -0.3 to 0.2 V, a pulse size of 50 mV, and a frequency of 10 Hz. These SWV and DPV parameters were previously optimized using FCA and ALP titrations.

In order to determine the range of detection, peak current (I_p) was plotted against ALP concentration on a log-scale for both methods (Fig. 3.3.3). Peak currents were determined from the baseline normalized DPV and SWV signals, as shown in Figure 3.3.3. SWV signals were baselined at -0.25 V and DPV signals were baselined at -0.2 V. Both DPV and SWV exhibited ALP detection over a range of 500 pg/ml to 50 ng/ml, with a LOD of 500 pg/ml. The dynamic range and LOD as measured by SWV was comparable to that of DPV, so DPV was continued as the method of choice for further nanocoaxial electrochemical measurements. Additionally, the time scale for each optimized scan was on the order of ~10 s for both methods, eliminating any time advantage commonly associated with SWV. All DPV measurements in the following work were performed with the same optimized parameters as used above. Potential range was the only varied parameter and was adjusted accordingly, depending on the oxidation potential of the redox molecule to be detected.

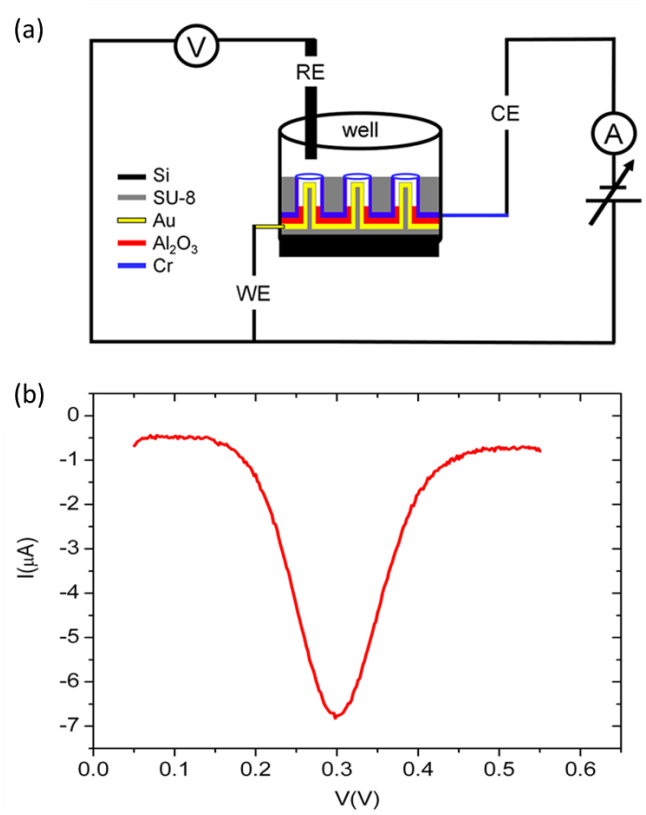

Figure 3.3.1. Electrochemical set-up. (a) Three-electrode system: inner metal (Au) of coaxial array served as WE, outer metal (Cr) served as CE, and an external Ag/AgCl wire served as RE. (b) Typical DPV waveform during the oxidation of FCA with Ag/AgCl as a RE. X-axis: potential (*V*); y-axis: current (*I*).

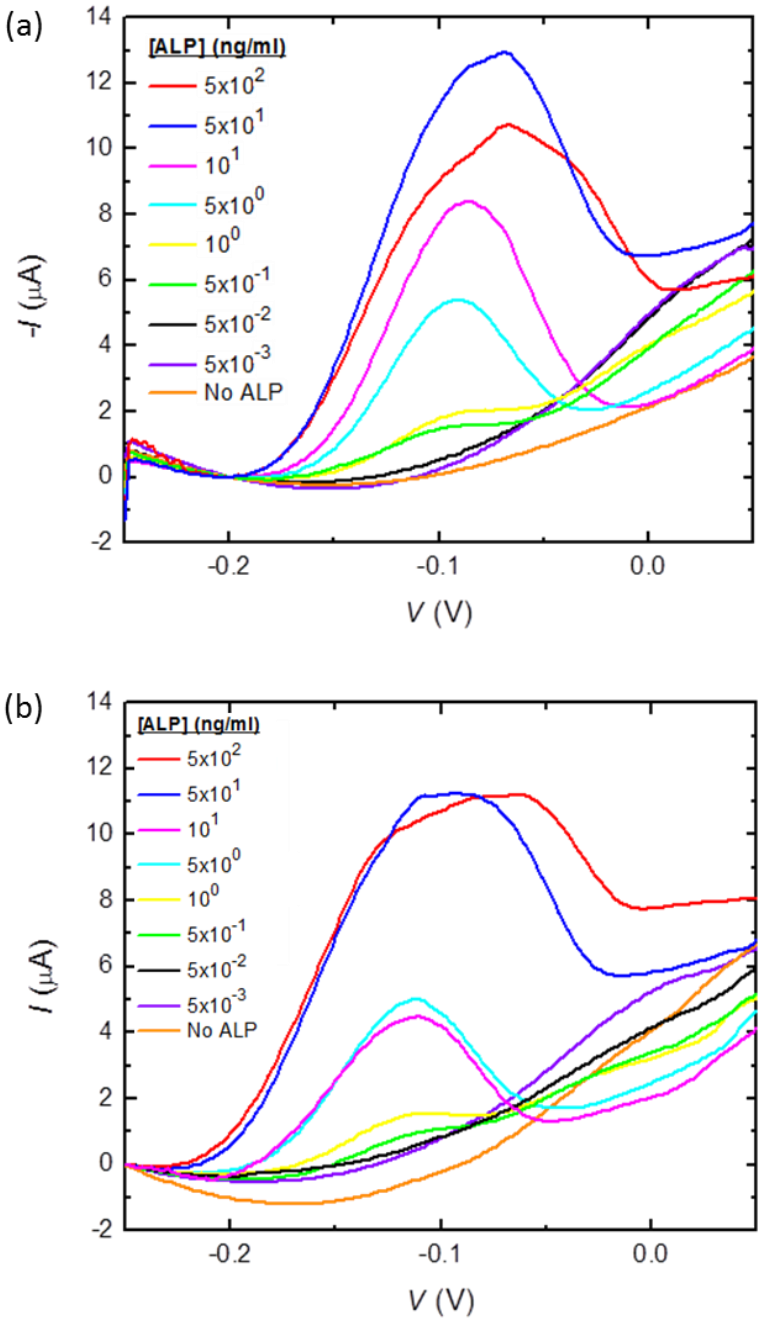

Figure 3.3.2. Electrochemical detection of an ALP titration by (a) SWV and (b) DPV on a planar gold electrode. SWV signals were baselined at -0.25 V and DPV signals were baselined at -0.2 V. X-axis: potential (*V*); y-axis: current (*I*). Data represent one trial.

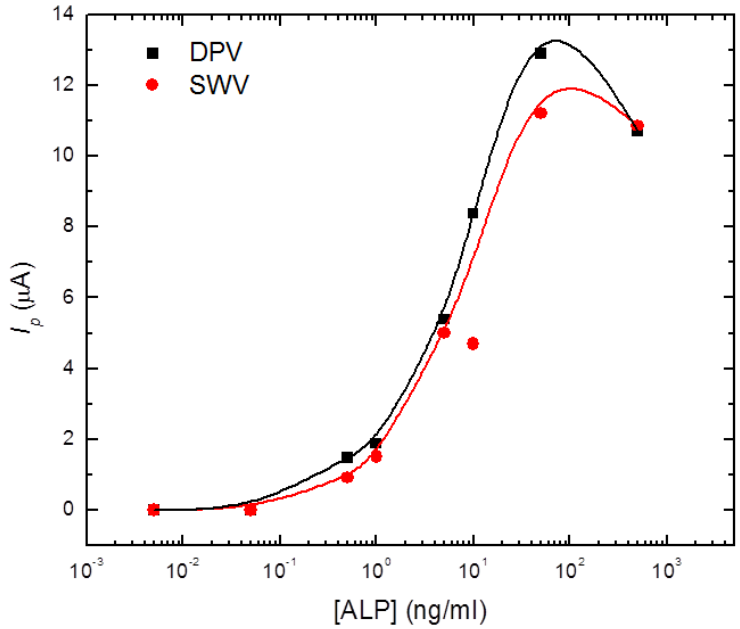

Figure 3.3.3. Range of electrochemical detection for ALP by SWV (red) and DPV (black). Peak current (I_p) was plotted against ALP concentration on a log-scale to determine range of detection. Peak currents were determined from the baseline normalized DPV and SWV signals as shown in Figure 3.3.2. Data points were fitted with B-spline curves, excluding the outlier at 10 ng/ml ALP in the SWV curve. Data represent one trial each for DPV and SWV.

3.4 Nanocoax for electrochemical sensing

Previous iterations of the nanocoax demonstrated ultrasensitive detection of volatile organic compounds (VOCs) due to a change in capacitance in the presence of these chemical gases[7]. Following this detection strategy, nanocoaxial capacitive sensing of biomolecules such as proteins was attempted; however, the presence of an electric double layer at the electrode/solution interface prevented the use of the nanocoax as a capacitive biosensor. Therefore, electrochemical techniques (e.g. DPV, SWV) that suppress capacitive charge and non-faradaic current were used.

To examine the potential of the nanocoax as an electrochemical sensor, DPV was employed to detect the oxidation of the redox species FCA. FCA (along with other ferrocene derivatives) is a commonly-used redox reporter molecule in electrochemical studies, whose oxidation potential has been highly characterized[11]. Nanocoaxial arrays of annulus thicknesses varying from 100 – 400 nm were investigated. The WE-CE annulus gap was chosen as the variable parameter due to previously reported amplification in signal associated with a decreased electrode gap[12,13]. A gold planar control of corresponding equivalent base area was examined to determine if the nanocoaxial architecture would improve signal over its macroscopic counterpart. Wells encapsulating each array were filled with about 100 µl of 1 mM FCA in PBS, pH 7.4 in the 3-electrode configuration depicted in Figure 3.3.1a. DPV was performed with a potential range of 0.0 and 0.5 V to encompass the oxidation potential of FCA at 0.3 V. We observed that current due to the oxidation of FCA increased with decreasing nanocoaxial annulus gap (Fig. 3.4.1a). Moreover in all cases, nanocoaxial arrays displayed higher current than the

planar control. Figure 3.4.1b quantitatively demonstrates the dependence of peak current on WE-CE annulus gap. On the left y-axis, peak current (determined from DPV currents in Figure 3.4.1a) was plotted against the gap size (x-axis). On the right y-axis, current densities of each array normalized to the planar control (J_{coax}/J_{planar}) were plotted against gap size (x-axis). Current densities were determined by normalizing peak current to the sensor base area. The data point at gap = 200 nm was the average of three separate nanocoaxial devices, with the error bar indicating the standard deviation. At the smallest annulus gap (100 nm), the nanocoaxial array exhibited 90 times greater signal in response to the oxidation of FCA, as compared to the planar counterpart. In addition, a significant improvement in signal-to-noise was observed, as the signal for the nanocoax was approximately 2 orders of magnitude greater than its planar counterpart, while the baseline noise level remained unchanged.

This observed signal improvement in nanocoaxial arrays over the macroscale planar electrode may be attributed to redox cycling between closely spaced, nanogap electrode surfaces. The nanoscale proximity between the WE and CE allows for dramatic amplification of signal by replenishing the redox species through reduction at the CE and rapid diffusion back to the WE. Nanocoaxial arrays with smaller WE-CE gaps exhibited greater signal improvement, suggesting that as annulus gap decreases, the effect of redox cycling increases. Furthermore, the concentric nature of the nanocoax structure allows for radial diffusion between the CE and WE. As a consequence, many more redox molecules reach the WE than in the case of planar diffusion found in planar electrodes and 2D nanogap devices. A final factor contributing to signal improvement may be the

high number of individual coaxes in the array. Each 1.8 mm^2 array contains ~10^6 coaxes connected in parallel, whose signals are additive.

Although nanocoaxial arrays with 100 nm WE-CE gaps demonstrated the highest signal improvement, following studies utilized coaxes with a 200 nm gap due to limiting factors associated with the 100 nm gap. WE-CE gaps of 100 nm exhibited difficulties with liquid loading during reagent exchange; this may be due to high surface tension at such a small gap, preventing reagent from properly diffusing into the annulus. Coaxes with 50 nm annulus gaps had been investigated and exhibited a decrease in current compared to 100 nm gaps, suggesting that a threshold point had been reached in which the decreased WE-CE gap becomes detrimental. In addition, yield of successful fabrication of 100 nm gap coaxial arrays was low, due to possible increased potential of shorting between the small electrode gap.

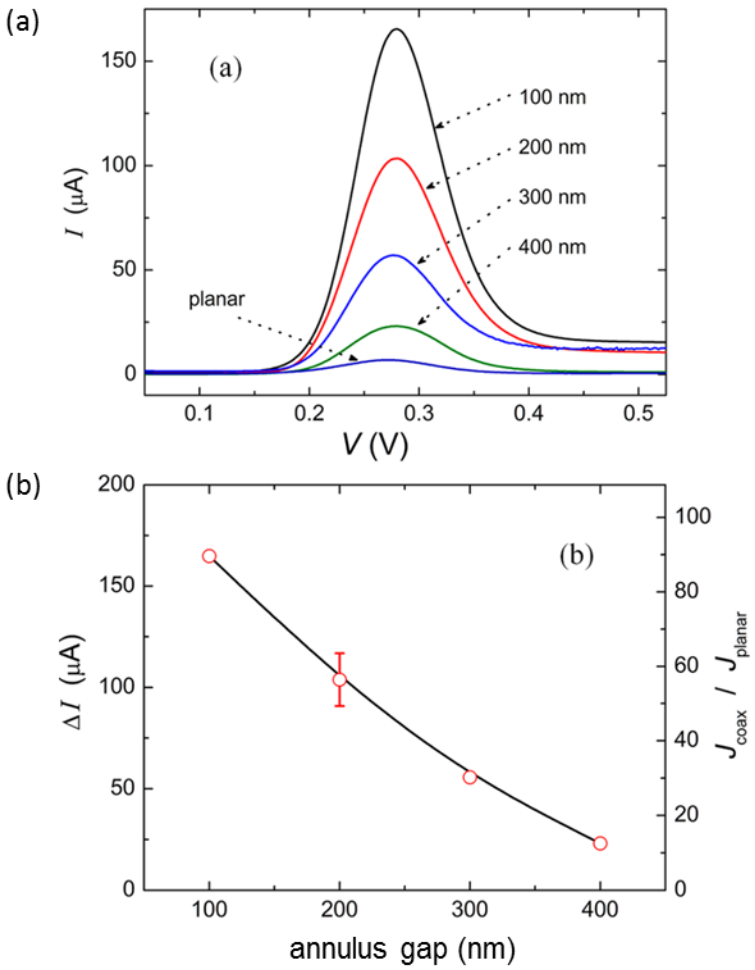

Figure 3.4.1. Electrochemical signal of nanocoaxial arrays with varying annulus thickness. (a) DPV signal of FCA oxidation on arrays with annuli varying from 100 to 400 nm WE-CE gaps. Planar counterpart with millimeter-scale CE-WE gap is also shown. X-axis: potential (V); y-axis: current (I). (b) Left y-axis: Peak currents (ΔI) vs. annulus WE-CE gap on the x-axis. Right y-axis: nanocoaxial current density normalized to that of planar current density (J_{coax}/J_{planar}) vs. annulus WE-CE gap on the x-axis. At annulus gap = 200 nm, three measurements were taken on three different devices; error bars represent standard deviation. All other data points represent one trial. Taken from Ref 14.

3.5 A nanocoaxial-based electrochemical biosensor

Nanocoaxial arrays of 200 nm annulus gap were further investigated as electrochemical sensors to detect biological molecules. All arrays underwent three steps of quality control before utilization in biological assays: SEM imaging, resistance measurements, and FCA oxidation signal. As previously mentioned (in Section 3.2), SEM was used to assess if arrays appeared to be correctly fabricated structurally. To confirm electrical integrity of each nanocoaxial array, resistance was measured between the working electrode and the counter electrode of each array. Typical resistance values of devices used ranged from 10 - 100 GΩ. Arrays with resistance below the MΩ regime were disregarded due to potential shorting issues. Nanocoaxial arrays were additionally tested with the redox species FCA to confirm electrochemical sensing capabilities. DPVs were performed with 1 mM FCA in PBS, pH 7.4 over a potential range of 0 to 0.5 V. DPV signals varied from -60 to -150 μA between arrays.

Batch-to-batch variation between arrays was observed with these quality control tests. Most notably in Figure 3.5.1, lower DPV current signals (-60 to -80 μA) corresponded to arrays with non-decapitated, intact inner electrodes (Fig. 3.5.1b). Higher DPV current signals (-150 μA) were observed with arrays whose inner electrode has been decapitated to expose the underlying SU-8 pillar (Fig. 3.5.1c). A possible explanation for this discrepancy may be due to increased hydrophilicity of SU-8 exposed nanocoaxes after pre-treatment with UV-ozone; all arrays underwent a UV/ozone cleaning pre-treatment before use, and treatment of SU-8 with ozone opens up residual epoxide rings in the polymer, dramatically increasing hydrophilicity[15]. This could provide decreased surface

tension at the annulus on coaxes with exposed inner SU-8 pillars and therefore allow more reagent into the gap. Because of this signal enhancement, all of the following electrochemical measurements were performed on arrays with decapitated, SU-8 exposed inner electrodes. The exception was the ALP titration in Figure 3.5.2 which was performed on an array with non-decapitated inner electrodes; this was due to the fact that this structural-dependent difference in FCA current signal had not yet been observed.

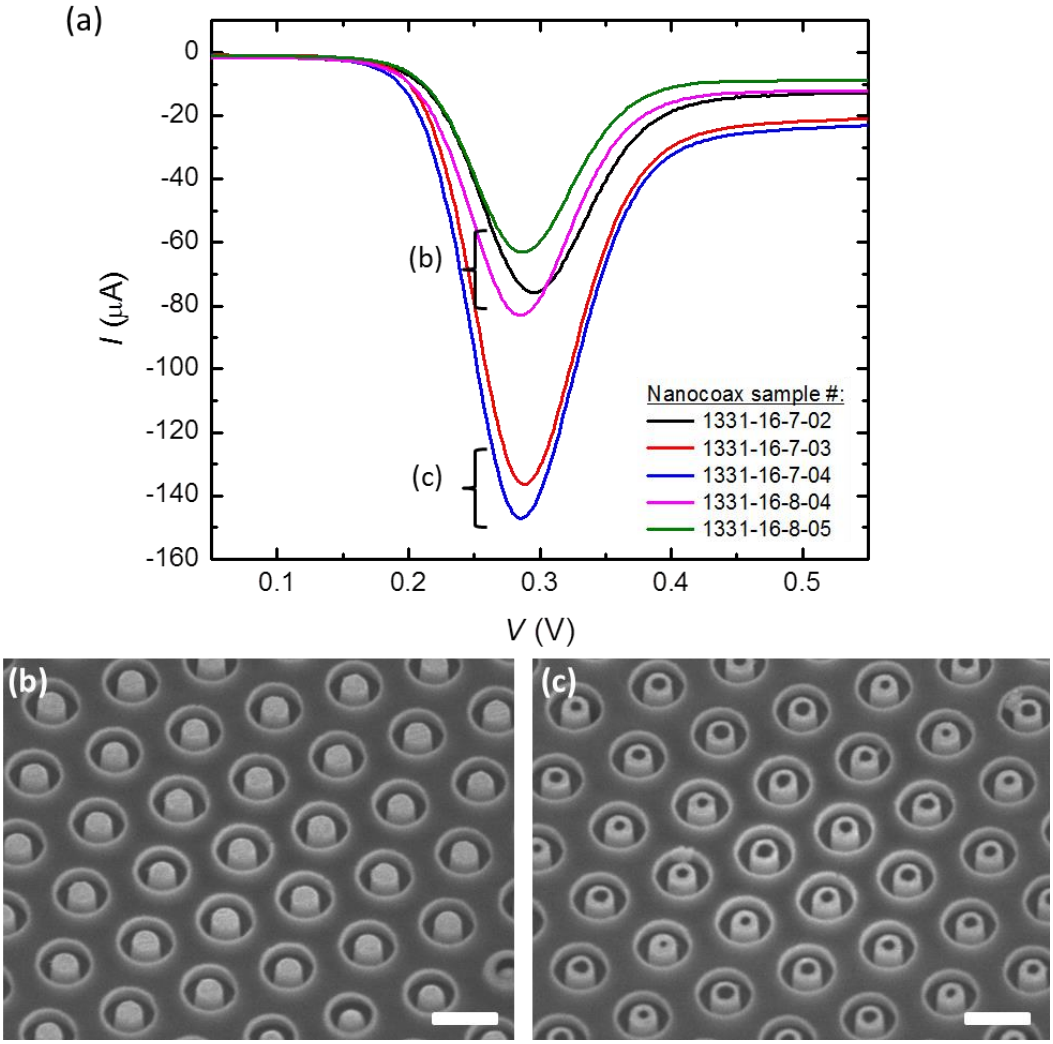

Figure 3.5.1. Electrochemical characterization of nanocoaxial arrays. (a) DPV signals of FCA oxidation on several arrays. Y-axis: current (*I*); x-axis: potential (*V*). (b) SEM of arrays with intact inner electrodes and (c) decapitated inner electrodes. Scale bars represent 1 μm; SEM images taken at a 30° tilt.

Next, an ALP titration was performed and DPVs were recorded on the nanocoax for proof-of-concept of a nanocoaxial-based electrochemical ELISA. Serial dilutions of ALP were incubated with 1 mM of the enzymatic substrate pAPP and then electrochemically examined on the nanocoax (Fig. 3.5.2a), as well as on a planar gold electrode to compare the nanocoaxial architecture for ALP detection to its macroscale counterpart (Fig. 3.5.2b). Each set of titration data (nanocoax and planar) was taken on a single device. Runs on additional devices gave qualitatively similar results; however, it was noted that some devices exhibited no electrochemical signal, likely due to shorting and fabrication issues. With the planar gold device, an ALP concentration of 10^{-3} ng/ml was required to measure an appreciable signal change from baseline at the -100 mV region. However, the nanocoax exhibited a noticeable current peak from baseline starting at an ALP concentration of 10^{-6} ng/ml (i.e. 10^{3}x more sensitive).

To determine the range of detection, peak current was normalized to the base area of each sensor (*J*) and plotted against ALP concentration (Fig. 3.5.3). At all concentrations the planar gold device exhibited appreciably lower overall current magnitude compared to the nanocoax. In addition, the nanocoax exhibited a greater dynamic range, over the ALP concentrations of 10^{-6} - 1 ng/ml. The planar counterpart, on the other hand, exhibited only a two decade dynamic range from 10^{-4} - 10^{-2} ng/ml ALP, trending toward saturation at the upper end and a lower limit of detection at 10^{-4} ng/ml ALP. It is worth noting that the true "active" area of the nanocoaxial array (i.e. the inner core/working electrode within each coax) is only a fraction (about 1/4) of the array's base area to which the current was normalized; yet the electrochemical signal from the nanocoax still surpassed

that of the planar device whose entire base area constitutes its working electrode. Therefore, this ALP titration highlights not only proof-of-concept for an electrochemical ELISA on the nanocoax, but also the significant advantage of the nanocoaxial structure over its planar counterpart towards greater electrochemical sensing capabilities.

We next developed an electrochemical ELISA for detection of cholera toxin (CT). CT was chosen as the benchmark disease biomarker due to its clinical relevance in water-borne infectious diseases[16]. In addition, the non-toxic B subunit of CT was utilized, which allowed for ease of handling. The CT ELISA was optimized identically for both optical and electrochemical readouts. All steps were performed in the same manner, except in the final step where the reporter molecule was added; Bluephos was added for optical readout, whereas pAPP was added for electrochemical readout. EDTA was chosen as the stop solution to quench the ALP reaction due to its ability to quench both optical and electrochemical ELISAs without interfering in readout; other stop solutions examined, such as sodium hydroxide, interfered with electrochemical readout.

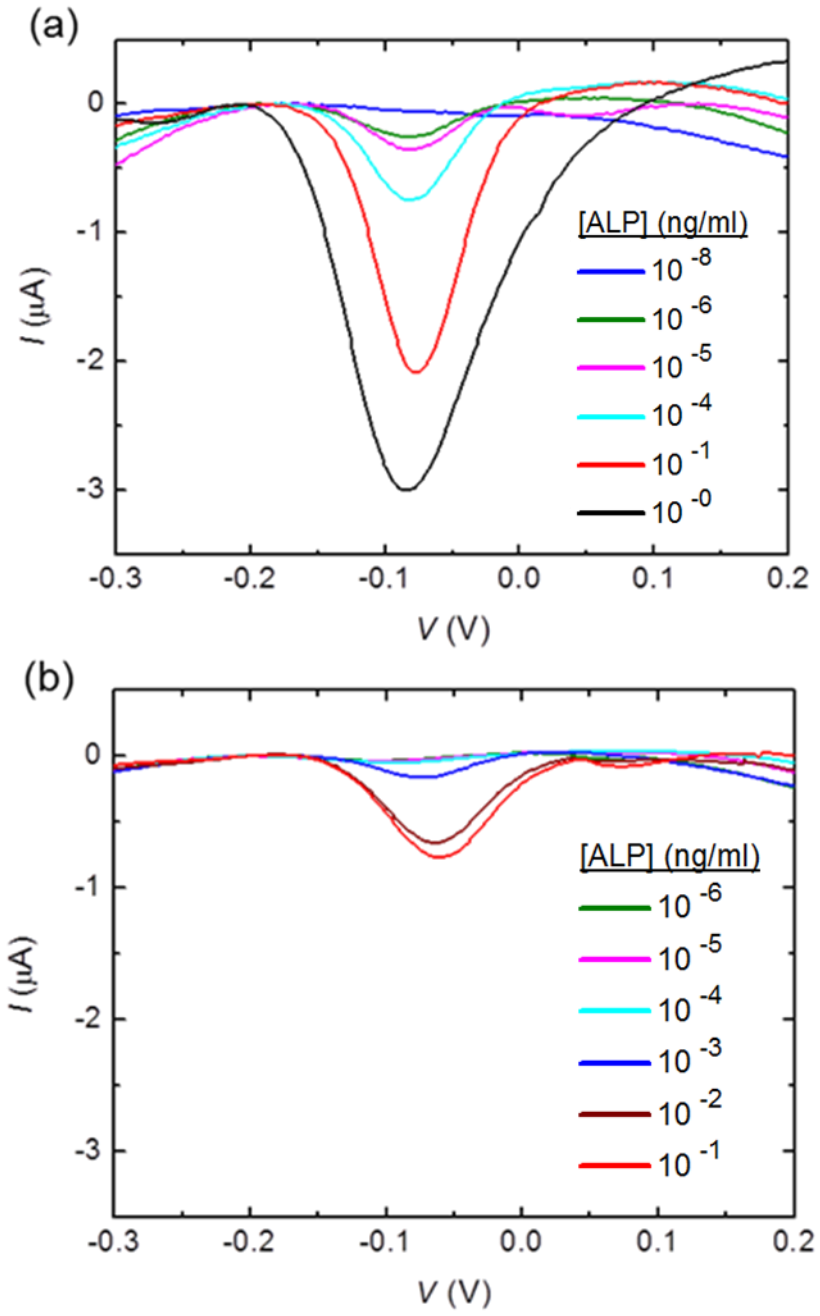

Figure 3.5.2. DPV signals of an ALP titration on (a) a nanocoaxial array and (b) a planar gold counterpart. DPV signals were subtracted to baseline at -0.2 V. X-axis: potential (*V*); y-axis: current (*I*).

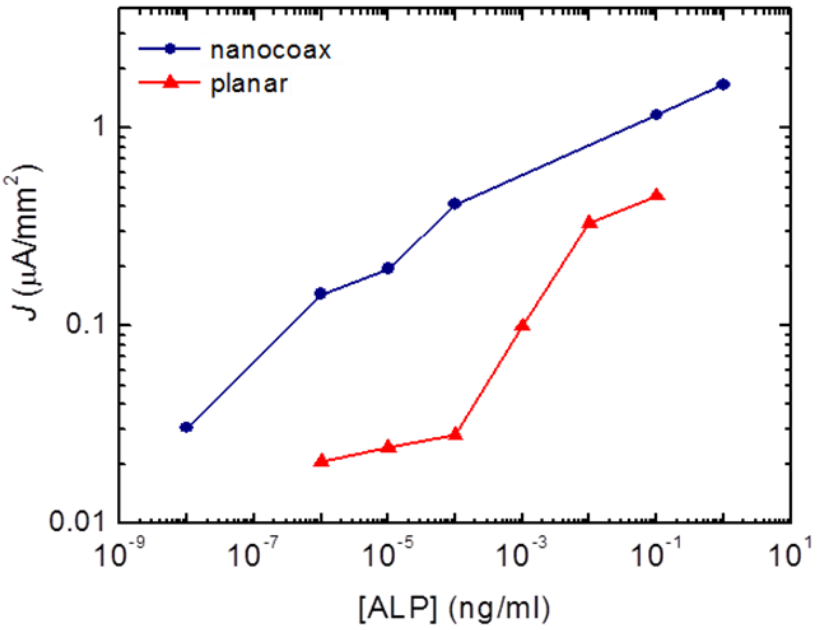

Figure 3.5.3. Detection range of ALP titration by nanocoax (blue) and planar Au sensor (red). On the y-axis, current density (*J*) was plotted against the log-scale of ALP concentration (x-axis). Current density was determined by normalizing peak current (from Figure 3.5.2) to base area of each sensor. Data represent one trial each.

ELISA reactions were performed externally in a 96-well plate and completed assay supernatants were then applied to the nanocoaxial array. The ELISA was run in duplicate with staggered replicates. All steps of the ELISA were run in parallel in both replicates until the final step: addition of 1 mM pAPP. 1 mM pAPP in TBS, pH 9 was added to the first replicate (R1), while TBST, pH 7.4 was added to the second replicate (R2). The ELISA proceeded to completion in R1, and DPVs were immediately recorded for R1 using the same parameters previously mentioned. Buffer was then removed from R2 and 1 mM pAPP in TBS, pH 9 was added to complete the assay. DPVs were then subsequently recorded for R2 on the same device. The replicates were staggered in such a manner due to previously observed degradation of 4-AP (the final redox product of the ELISA); the staggered replicates attempted to prevent any 4-AP degradation in R2 that would occur from increased wait time before DPV measurements.

Figure 3.5.4 shows the DPV signals obtained for both replicates of a staggered electrochemical ELISA, with the current subtracted to baseline at -0.2 V to determine peak current. CT concentrations ranging from 1 ng/ml to 10 μg/ml were examined. Both replicates produced discernable current peaks at all CT concentrations, however the DPV signal for the "No CT" control exhibited a noticeable current peak as well. This suggested non-specific binding of the ALP-labeled antibody; therefore, the detection antibody concentration was adjusted accordingly to a lower concentration in all following ELISAs. In addition, R1 (Fig. 3.5.4a) did not demonstrate the smooth, overlapping DPV baselines as seen in R2 (Fig. 3.5.4b). The first DPV signal in R1 ("No CT" measurement) exhibited significant drift, resulting in a deviating baseline from other

DPV signals. However, this drift eventually faded in subsequent R1 measurements as indicated by uniform, overlapping baselines, and was not present in any R2 measurements. This suggested that coaxial devices may need to be electrically preconditioned before use. Preconditioning is thought to remove any remaining contaminants and "warm up" the electrode[17,18]. Therefore, all future measurements were preceded by 3-5 DPV runs in TBS buffer to alleviate any effects from drift.

To determine the dynamic range, peak current was plotted against the CT concentration on a log scale (Fig. 3.5.5a). Peak current was determined from DPV signals in Figure 3.5.4 that were baselined at -0.2 V. A log-linear dynamic range of 4 ng/ml - 100 ng/ml ($R^2 \geq 0.95$) was observed, with a lower LOD of 1 ng/ml. The effect of drift in R1 is further emphasized in Figure 3.5.5a; both replicates qualitatively exhibited the same range of detection, however at lower concentrations in R1, current signals were quantitatively lower until the drift effect fell off after a few measurements on the device.

In addition, the electrochemical nanocoaxial sensor was compared to the conventional optical ELISA as a standard control. The optical ELISA was performed in the same manner as the electrochemical ELISA, with the exception that the BluePhos substrate was used in place of pAPP. BluePhos is converted by ALP into a colorimetric product, whose optical absorbance is read at λ_{max}=600 nm. In Figure 3.5.5b, CT concentration was plotted against absorbance; the optical readout exhibited a log-linear range of detection from 2 ng/ml - 100 ng/ml ($R^2 \geq 0.95$), with a lower LOD of 1 ng/ml. Here, electrochemical detection with the nanocoax and the standard optical readout exhibited

essentially the same range of detection and LOD. However, as seen in Figure 3.5.5, the lower end had not yet trended to a zero value in either the electrochemical or optical readouts, suggesting that both methods are capable of CT detection beyond the range of CT investigated. Following experiments increased the lower range beyond 1 ng/ml to discover the true LOD of each method.

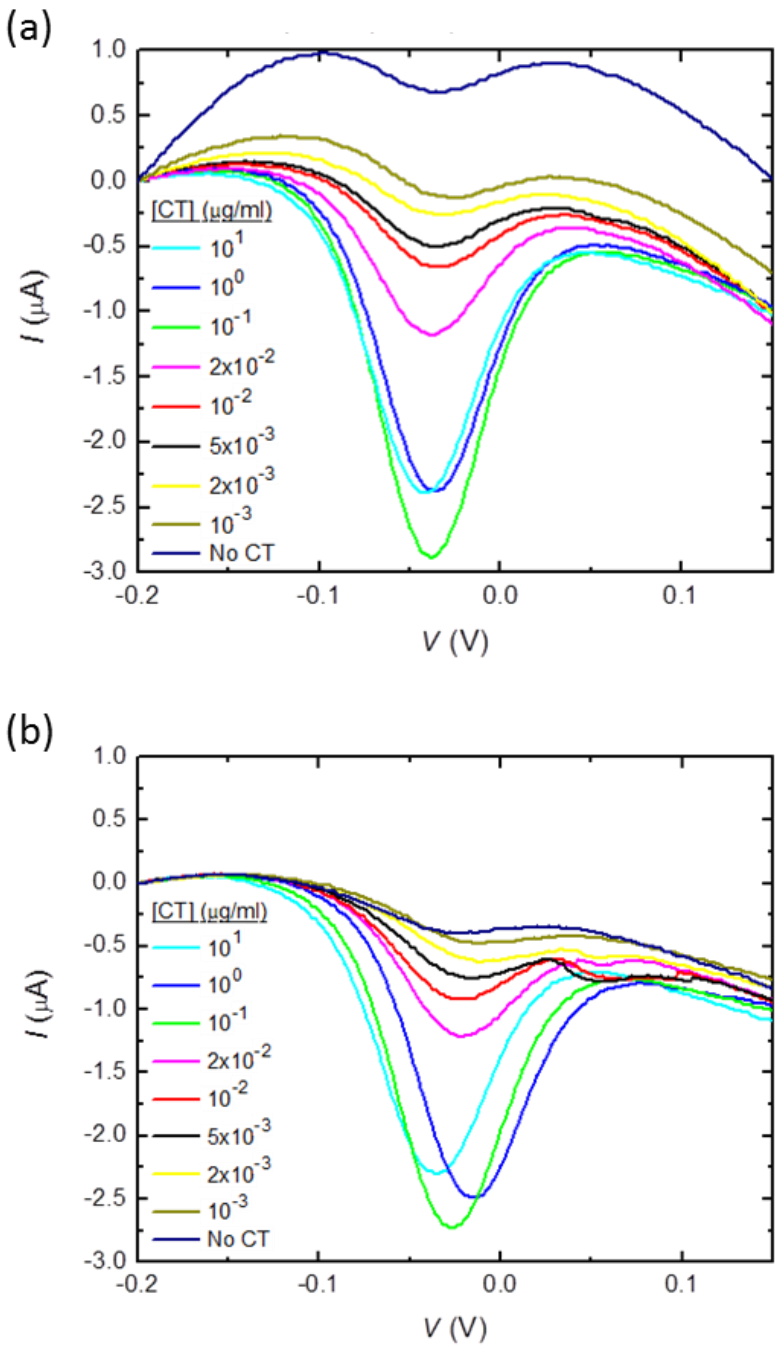

Figure 3.5.4. DPV signals of a staggered CT ELISA on a nanocoaxial array for (a) replicate 1 (R1) and (b) replicate 2 (R2). Both replicates were measured on the same device. Current subtracted to baseline at -0.2 V. X-axis: potential (*V*); y-axis: current (*I*).

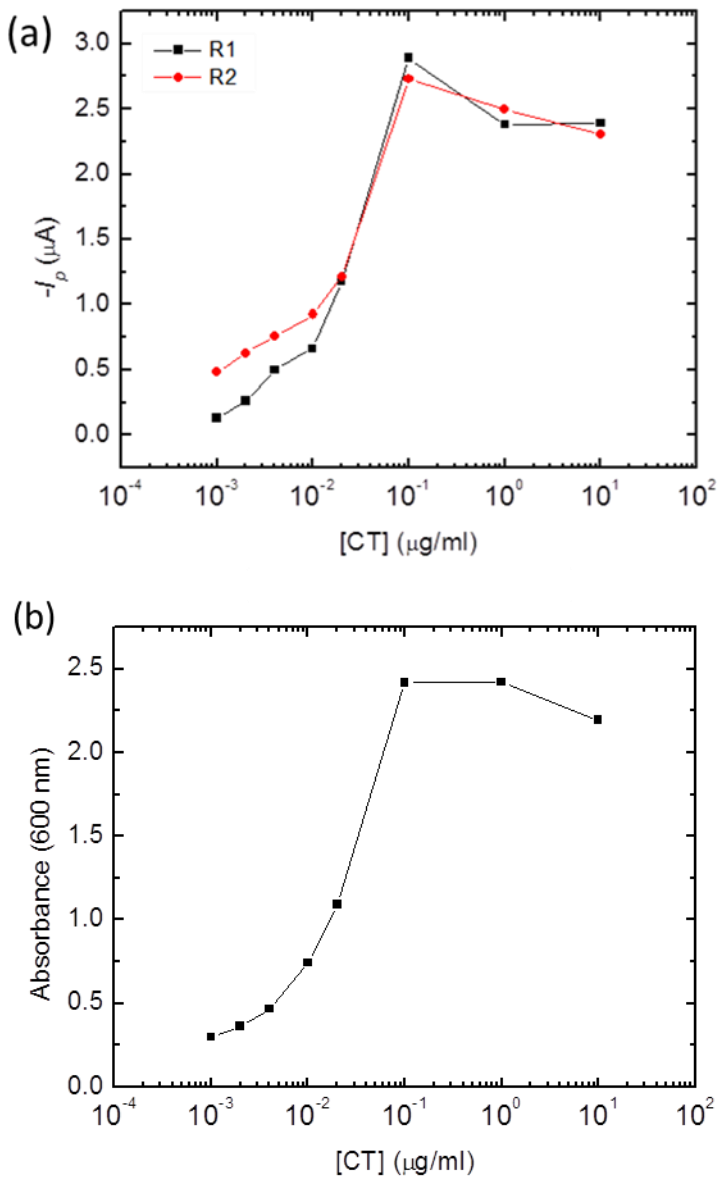

Figure 3.5.5. Detection range of staggered CT ELISA by electrochemical and optical methods. (a) Electrochemical readout on nanocoax: peak current ($-I_p$) of staggered replicates (R1 and R2) on the y-axis vs. log-scale of CT concentration on the x-axis. Both replicates measured on the same nanocoaxial device. (b) Optical readout: absorbance at 600 nm (y-axis) vs. log-scale of CT concentration (x-axis). Data represent one trial.

Reusability and reproducibility of nanocoaxial arrays were examined with the same device used in Figure 3.5.6. Another CT ELISA was performed and DPVs were recorded (Fig. 3.5.6a). The device was preconditioned with three DPV runs of TBS, pH 9 prior to the measurement of ELISA reactions in order to alleviate drift. Successful preconditioning was demonstrated by a smooth, overlapping DPV baseline after the final run of TBS (yellow line in Fig. 3.5.6a). To assess reproducibility, three subsequent measurements were taken for $2x10^{-2}$ μg/ml. It should be noted that the "No CT" and 10^{-3} μg/ml CT concentrations were not shown; data were initially recorded on a different device that shorted midway through the experiment, depleting the ELISA reactions for those concentrations. Range of detection was determined by plotting peak current against CT concentration (Fig. 3.5.6b); the device detected CT from 10^{-2} to 1 μg/ml, with a LOD of 10^{-2} μg/ml, whereas previously the same device had detected CT from $4x10^{-3}$ to 10^{-1} μg/ml with a LOD of 10^{-3} μg/ml. In both ELISAs, the device detected CT across a range of 3 orders of magnitude; however during reuse, the device was less sensitive at the lower end range and the range shifted up an order of magnitude. Despite degradation of signal at lower CT concentrations, statistical analysis of the replicate data at $2x10^{-2}$ μg/ml indicates significant reproducibility of measurements on a single nanocoaxial device. These results indicated that the device was capable of being reused for multiple ELISAs; however, a degradation of sensitivity at lower concentrations observed over time shifted the range of detection.

Electrochemical detection of CT by nanocoaxial arrays was further analyzed with an increased range of CT concentrations to determine the true range and LOD. ELISAs

were performed in duplicate and both replicates were electrochemically measured concurrently on the same device. Identical CT concentrations in both replicates were measured in parallel as opposed to measuring all of R1 first and then R2 as was done with a staggered ELISA. Degradation effects of 4-AP between replicates were significantly minimized in this manner. In addition, any variation in the addition of pAPP to R1 and R2 in staggered stages was eliminated. Figure 3.5.7 shows the DPV signals obtained from a non-staggered ELISA run in duplicate, with the current subtracted to baseline at -0.15 V to elucidate peak current. To determine the dynamic range, peak current was plotted against the CT concentration on the log scale (Fig. 3.5.8). Here, we observed a log-linear dynamic range of 10 ng/ml - 1 μg/ml ($R^2 \geq 0.95$), with a lower LOD of 2 ng/ml (as determined by LOD = $I_{p,control} + 3\sigma_{control}$; control = No CT sample). Statistical analysis of the replicate data indicates significant reproducibility of measurements on a single nanocoaxial device. It should be noted that error bars representing standard deviation are present at every CT concentration in Figure 3.5.8; however in most cases, the error bars were smaller than the graphed data points themselves.

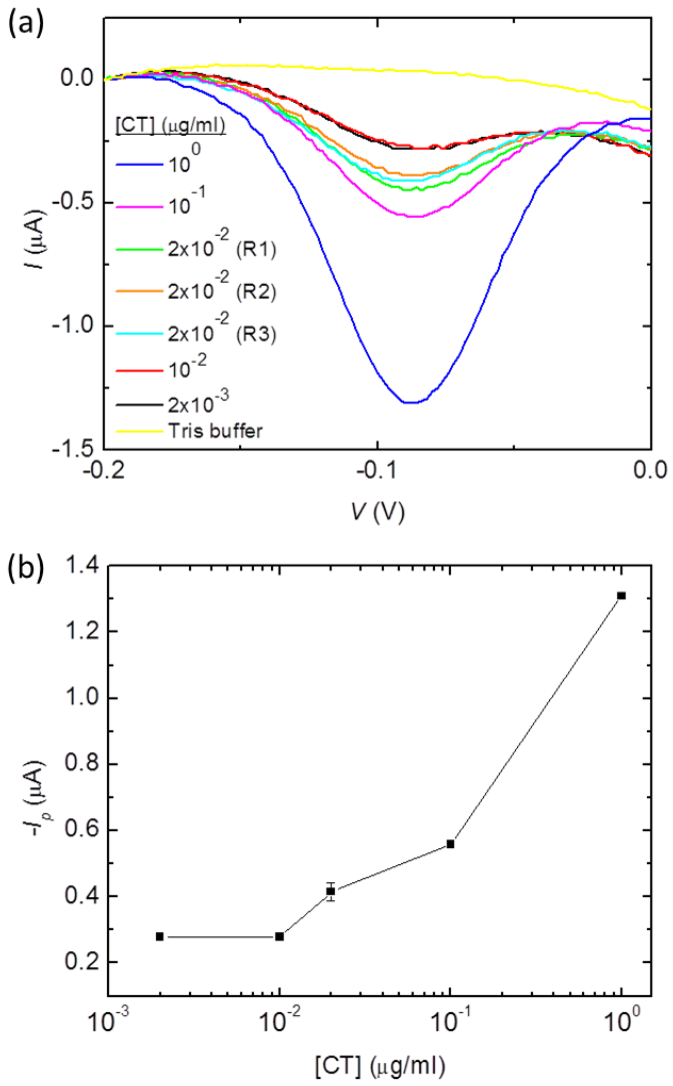

Figure 3.5.6. Reusability of nanocoaxial arrays. (a) DPV signals of a CT ELISA on a previously used coaxial array. DPV signals were subtracted to baseline at -0.2 V. Three replicates were performed at [CT] = $2x10^{-2}$ μg/ml. X-axis: potential (*V*); y-axis: current (*I*). (b) Peak current ($-I_p$) on the y-axis vs. log-scale of CT concentration on the x-axis. Peak currents were determined from baselined DPV signals in Figure 3.5.6a. Error bar at [CT] = $2x10^{-2}$ μg/ml represents standard deviation. All other data points represent one trial.

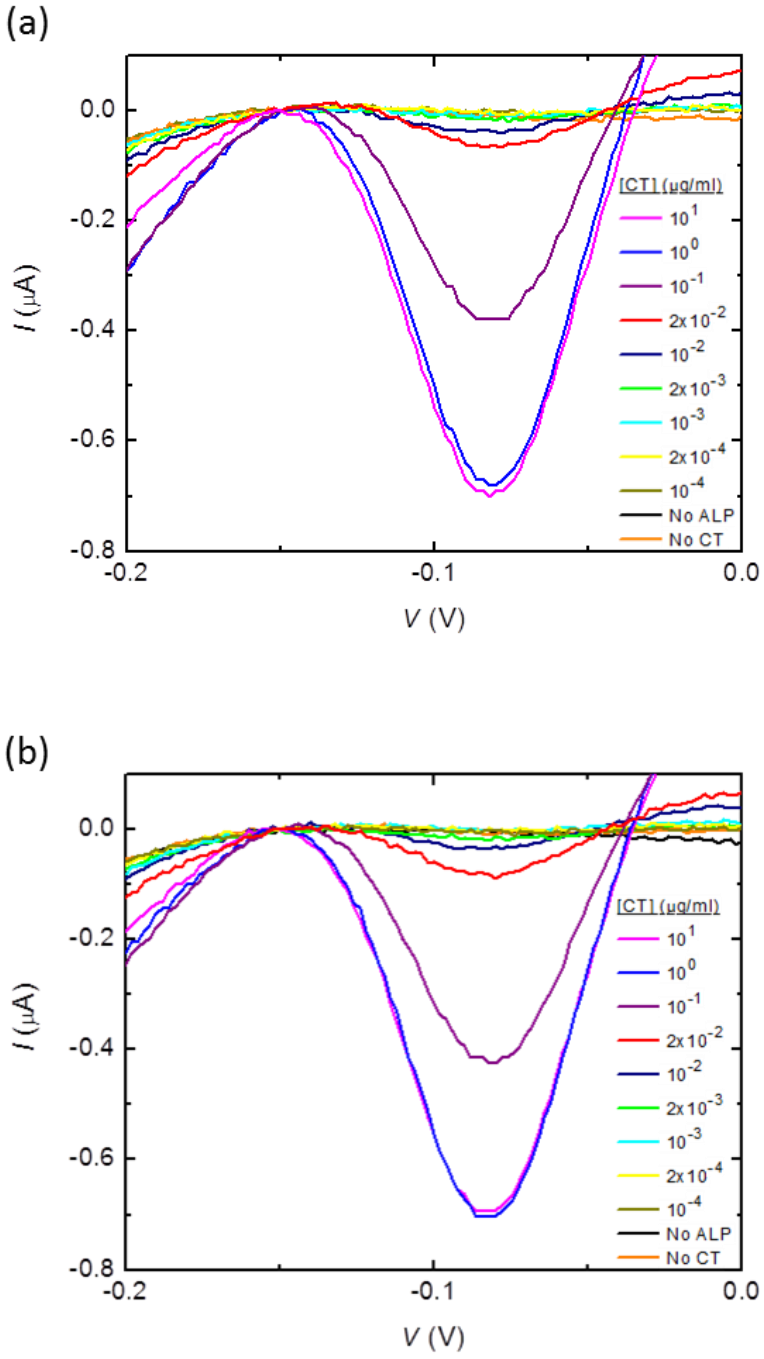

Figure 3.5.7. DPV signals of a non-staggered ELISA. (a) First replicate (R1) and (b) second replicate (R2) were measured in parallel on the same nanocoax device. DPVs were subtracted to baseline at -0.14 V. X-axis: potential (*V*); y-axis: current (*I*).

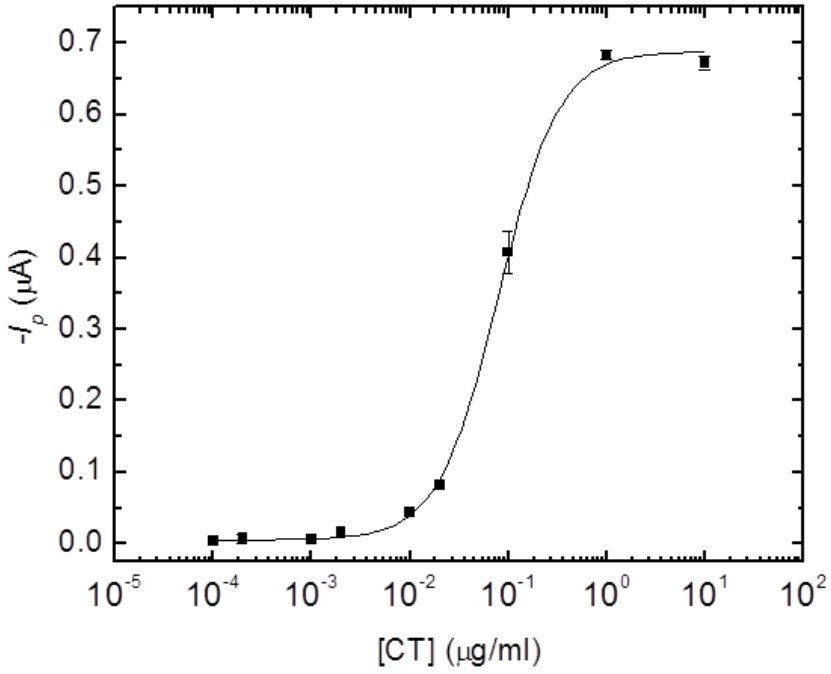

Figure 3.5.8. Detection range of a non-staggered ELISA on a nanocoax. Peak current (-I_p) (y-axis) vs. log-scale of CT concentration (x-axis) from a non-staggered ELISA. Peak currents were determined from baselined DPV signals in Figure 3.5.7. Data points represent average of duplicates (R1 and R2); error bars represent standard deviation.

In addition, electrochemical detection with the nanocoaxial sensor was compared to the conventional optical ELISA as a standard control. The optical ELISA was carried out in duplicate and the results are shown in Figure 3.5.9 on the right y-axis, with absorbance plotted against CT concentration. On the left y-axis of Figure 3.5.9, peak current was plotted against CT concentration (peak currents were determined from Figure 3.5.7). The optical readout was linear over a dynamic range of 10 ng/ml to 1 μg/ml, with a LOD of 1 ng/ml. Electrochemical detection was linear over the same dynamic range of 10 ng/ml to 1 μg/ml and exhibited a similar LOD of 2 ng/ml. These results indicated that the nanocoaxial electrochemical sensor is comparable to the standard optical ELISA with respect to the linear dynamic range of detection and exhibited a LOD on the same order of magnitude (2 ng/ml vs. 1 ng/ml).

It was observed that the DPV signal from the oxidation of 1 mM FCA degraded over multiple measurements, despite exchanging FCA reagent in between each measurement[19]. While devices had an initial current of -80 to -150 μA (depending on inner electrode structure) during FCA oxidation, subsequent measurements on all arrays exhibited a decrease in current and an eventual stabilization at -25 to -30 μA. However, as demonstrated in Figures 3.5.5 and 3.5.8, nanocoaxial arrays were able to electrochemically detect CT with comparable sensitivity to the conventional optical readout. These results indicated that the current saturation observed with FCA was an effect independent of ELISA performance (i.e. the oxidation of 4-AP).

To confirm this observation, DPVs of a CT ELISA were performed on an array that had not been previously FCA tested (Fig. 3.5.10a). Four DPVs were performed with 1 mM FCA after ELISA measurements had been already been recorded. The initial FCA current signal was ~ -90 μA, which fell in the characteristic range of initial FCA tests on coaxial arrays. Subsequent DPV measurements exhibited a decrease in current and eventual stabilization at ~ -25 μA. In addition, DPV signals of FCA oxidation were taken on another separate array before and after an ELISA was electrochemically measured (Fig. 3.5.10b). The FCA response recorded before ELISA measurements was ~ -110 μA, ~ -25 μA after the first ELISA replicate (R1), and ~ -25 μA after the second ELISA replicate (R2). Both replicates (R1 and R2) detected CT over the same range and exhibited the same LOD with comparable peak currents (as seen in Figure 3.5.5a), despite the change in FCA current from -110 μA before R1 to -25 μA before R2 measurements. Moreover, both of these devices reproducibly detected CT over a similar range (~1 ng/ml – 1 μg/ml) and LOD (~ 1 ng/ml), regardless of whether FCA oxidation current was around -100 μA or stabilized at -25 μA before ELISA measurements. This strongly suggests that the signal degradation of FCA is independent of ELISA performance and may be a molecule specific phenomenon that does not necessarily indicate device degradation.

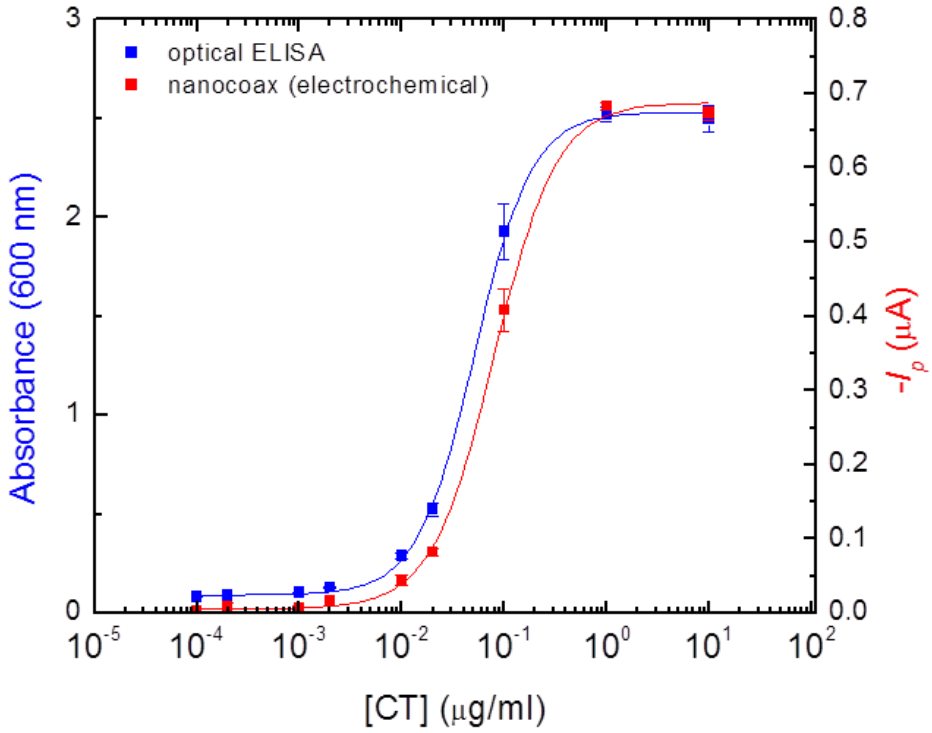

Figure 3.5.9. Electrochemical and optical readouts of a CT ELISA. On the right y-axis, peak current (I_p) vs. CT concentration (x-axis) is plotted for electrochemical detection by the nanocoaxial array (red). Peak currents were determined from the baselined DPV signals as shown in Figure 3.5.7. Data represents two trials run on the same device; error bar shown is the standard deviation. On the left y-axis, absorbance at λ = 600 nm is plotted against CT concentration (x-axis) for the conventional optical readout of an ELISA (blue). Data represent two trials. Error bar shown is the standard deviation.

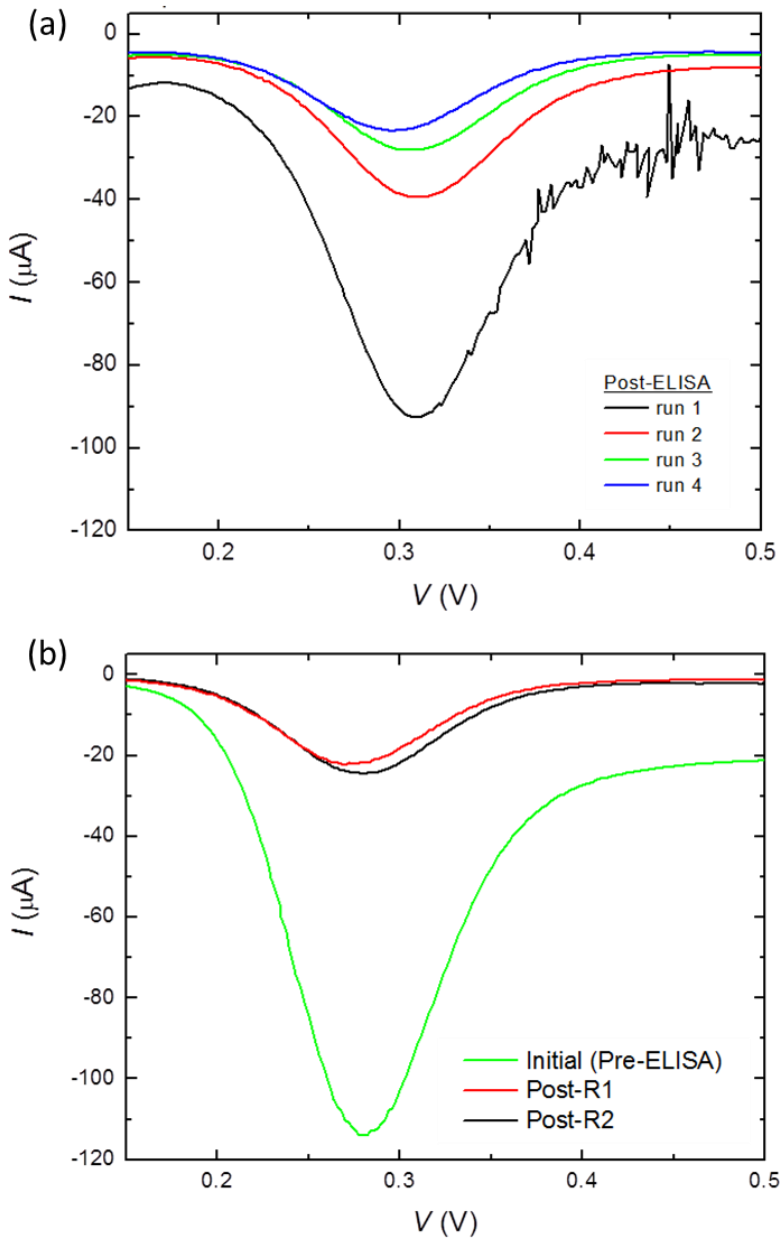

Figure 3.5.10. FCA degradation on nanocoaxial arrays independent of ELISA performance. (a) DPVs of 1 mM FCA on a nanocoaxial device that has already undergone ELISA measurements without any previous FCA testing. (b) DPVs of 1 mM FCA on a device before and after ELISA measurements run in duplicate (R1: replicate 1; R2: replicate 2). Y-axis: potential (*V*); x-axis: current (*I*).

3.6 Future directions: extended core coax

We have demonstrated electrochemical nanocoaxial detection of CT with sensitivity comparable to the conventional optical readout. However two issues inhibit the nanocoax from further development into a POC device: diffusion of reagent into the annulus gap and liquid loading/exchange. Difficulties with reagent diffusion into the annulus gap due to surface tension was observed with increasingly small annuli gaps, inhibiting redox molecules from diffusing between the electrodes for electrochemical measurements and thus lowering sensitivity. In addition, once reagent was inside the gap, liquid exchange of reagents was extremely hindered, if not impossible. Ethanol washes followed by N_2 drying were required to remove reagent between measurements. However in a POC device, ELISA reagents (e.g. CT antibody) would ideally be tethered to the inner electrode; this requirement for ethanol washes in between steps is not amenable to biofunctionalization as ethanol would denature and disrupt protein interactions.

A next generation coaxial device, the extended core coax (ECC), is also currently being developed to overcome these obstacles. The ECC retains the nanocoaxial architecture, however the inner electrode extends some distance (e.g. 200 nm) above the outer electrode. Moreover, annulus depth has been lessened to 200 nm from the previous 500 nm depth, with the prospect of eliminating any depth altogether. Together, these two factors should reduce surface tension between electrodes and allow for proper liquid exchange. Moreover, the extended core structure would allow for biofunctionalization and advance the nanocoaxial architecture towards POC potential. The ECC architecture

could allow for a highly-effective flow-through device, where reagent entry into the annulus is not required, yet the nanoscale proximity (WE-CE) advantage is maintained.

ECC arrays were fabricated by similar methods as first generation nanocoaxial arrays. Si pillar arrays served as the base substrate, and were coated with a 10 nm Ti adhesion layer, followed by 110 nm Au to form the inner electrode. A dielectric layer of 150 nm Al_2O_3 was deposited via ALD, followed by sputter deposition of 125 nm Cr to form the outer electrode. Cr and Al_2O_3 were then wet-etched away to expose the extended gold core and form the dielectric annulus with a 200 nm depth. Figure 3.6.1a shows a SEM image of a fully fabricated ECC array. These arrays have a base area of 0.2 mm^2 (d= 500 μm) and contain ~10^5 individual coaxes, compared to the 1.8 mm^2 base area of first generation arrays (d = 1.5 mm), which contained ~10^6 coaxes. In addition, a single chip of 16 x 30 mm^2 area has ten independently addressed arrays (with the ability to accommodate more), providing a platform amenable to multiplexing for the detection of multiple disease biomarkers simultaneously.

To examine the potential of the ECC architecture for electrochemical sensing, DPVs were performed to detect the oxidation of 1 mM FCA (Fig. 3.6.1b). Multiple DPV measurements exhibited similar current signals, with an average peak current of approximately -30 μA. Subsequent runs exhibited smoother curves, suggesting a similar requirement for preconditioning as the previous coax iteration. Current densities (*J*) were calculated for the ECC and for the first generation nanocoax to compare electrochemical performance (Fig. 3.6.2); a planar Au control was examined as well. Current densities

were determined by dividing the peak current from Figure 3.6.1b by the array base area. Current density for the nanocoax was calculated using -150 μA, the highest peak current obtained from FCA oxidation on a first generation array. The ECC array exhibited a current density of 150 $\mu A/mm^2$ and the nanocoaxial array exhibited a current density of 83 $\mu A/mm^2$. Planar Au controls exhibited a current density of 5 $\mu A/mm^2$. The ECC array exhibited an approximate 2-fold increase in current density over the nanocoax, with an array base area 9x smaller.

The increased current density of the ECC array could allow for improved sensitivity in the electrochemical detection of biomarkers over the first generation nanocoax. Additionally, ECC arrays provide a platform amenable to biofunctionalization and multiplexing. Further studies (ALP dose titrations, ELISAs) with the ECC arrays will be completed to determine if the increased current density corresponds to improved sensitivity. If sensitivity is not improved, the ECC will still provide advantages over the first generation nanocoax. The extended core will allow for biofunctionalization of receptor protein directly onto the inner electrode, and the small array areas would allow for facile multiplexing for multiple disease biomarkers on a single portable chip. Together, these factors could advance the nanocoaxial architecture towards a true POC device.

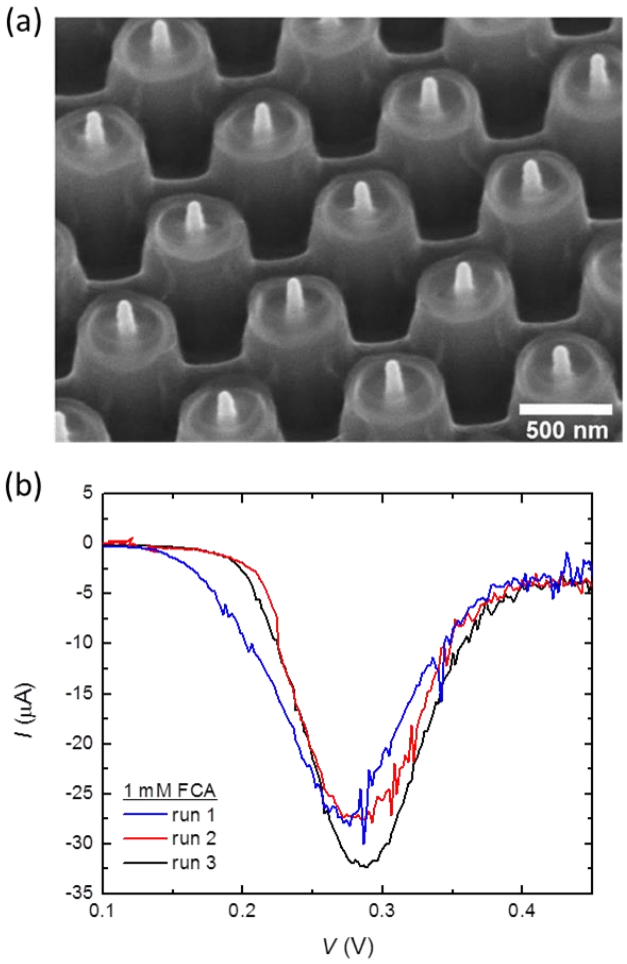

Figure 3.6.1. Extended core coax. (a) SEM of an ECC array (taken at 30° tilt), with an inner Au core as the WE and an outer Cr CE. (b) DPV signals of 1 mM FCA on an ECC array. DPVs were measured on the same device. X-axis: potential (*V*); y-axis: current (*I*).

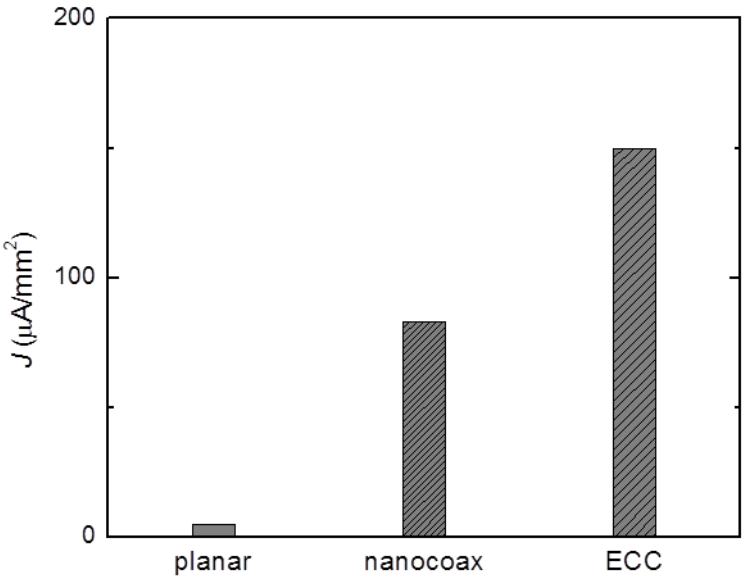

Figure 3.6.2. Current densities (*J*) of planar Au, nanocoax and ECC during the oxidation of 1 mM FCA. Current densities were determined by dividing DPV peak current by array base area.

Summary

Nanocoaxial-based arrays have been fabricated and developed as electrochemical biosensors for the detection of the infectious disease biomarker, CT. The decreasing nanoscale proximity between the working and counter electrodes has been shown to be advantageous in enhancing electrochemical signal, with an optimal WE-CE gap of 200 nm. Nanocoaxial detection of alkaline phosphatase titrations provided proof-of-concept for an electrochemical ELISA, and demonstrated increased sensitivity over its planar electrode counterpart. The nanocoax exhibited electrochemical detection of a CT ELISA comparable to the standard optical ELISA with regard to dynamic range and LOD. Both nanocoaxial electrochemical readout and the optical readout exhibited a log-linear range of detection over the CT concentrations of 10 ng/ml to 1 μg/ml. Nanocoaxial arrays demonstrated a LOD of 2 ng/ml, on the same order as the optical readout whose LOD was 1 ng/ml.

The electrochemical readout of the nanocoax matches the performance of the optical readout, while providing advantages over the conventional ELISA towards further development to POC applications. Nanocoaxial-based sensors allow for a simple electrical readout that utilizes less reagent and provides a miniaturized platform amenable to multiplexing for the detection of multiple disease biomarkers simultaneously. With further development and characterization of the extended core coax architecture, nanocoaxial sensors will have high potential towards use in POC devices.

References

1. Heinze, J. Ultramicroelectrodes in electrochemistry. *Angew. Chemie Int.* 1268–1288 (1993).

2. Li, T. & Hu, W. Electrochemistry in nanoscopic volumes. *Nanoscale* **3,** 166–76 (2011).

3. Schuster, R., Kirchner, V., Xia, X., Bittner, A. & Ertl, G. Nanoscale electrochemistry. *Phys. Rev. Lett.* **85,** 473–486 (1998).

4. Chen, X. *et al.* Electrical nanogap devices for biosensing. *Mater. Today* **13,** 28–41 (2010).

5. Rybczynski, J. *et al.* Subwavelength waveguide for visible light. *Appl. Phys. Lett.* **90,** 021104 (2007).

6. Guo, L. J. Nanoimprint lithography: methods and material requirements. *Adv. Mater.* **19,** 495–513 (2007).

7. Zhao, H. *et al.* Ultrasensitive chemical detection using a nanocoax sensor. *ACS Nano* **6,** 3171–8 (2012).

8. Merlo, J., Ye, F., Rizal, B., Burns, M. J. & Naughton, M. J. Near-field observation of light propagation in nanocoax waveguides. *Opt. Express* **22,** 14148–14154 (2014).

9. Ricci, F., Adornetto, G. & Palleschi, G. A review of experimental aspects of electrochemical immunosensors. *Electrochim. Acta* **84,** 74–83 (2012).

10. Bard, A. J. & Faulkner, L. R. *Electrochemical methods: fundamentals and applications. 2nd edition.* 156–157 (2001).

11. Stepnicka, P. *Ferrocenes: Ligands, Materials and Biomolecules*. 281–319 (2008).

12. Yi, M., Jeong, K.-H. & Lee, L. P. Theoretical and experimental study towards a nanogap dielectric biosensor. *Biosens. Bioelectron.* **20,** 1320–6 (2005).

13. White, R. & White, H. Electrochemistry in nanometer-wide electrochemical cells. *Langmuir* **84112,** 7672–7677 (2008).

14. Rizal, B. *et al.* Nanocoax-based electrochemical sensor. *Anal. Chem.* **85,** 10040–4 (2013).

15. Delplanque, A. *et al.* UV/ozone surface treatment increases hydrophilicity and enhances functionality of SU-8 photoresist polymer. *Appl. Surf. Sci.* **314,** 280–285 (2014).

16. Http://www.who.int/mediacentre/factsheets/fs107/en/. *WHO Cholera*. (2012).

17. Stefan, R.-I., van Staden, J. F. & Aboul-Enein, H. Y. *Electrochemical Sensors in Bioanalysis*. 213 (2001).

18. Engstrom, R. Electrochemical pretreatment of glassy carbon electrodes. *Anal. Chem.* **2314,** 2310–2314 (1982).

19. Rizal, B. *Nanocoax arrays for sensing devices*. 82–87 (2014).

Chapter 4.

Dendrites

4.1 Introduction

Metallic dendrites represent another type of electrode gaining attention as sensitive electrochemical sensors. Metallic dendrites are crystals with tree-like branching structures, and can be composed of a single metal or an alloy[1]. Dendrites are an attractive class of materials for electrochemical sensors due to their high surface-area-to-volume ratio. This increase in surface area facilitates larger numbers of biomolecular events at the electrode surface, promoting high levels of collisions with target analytes and higher rates of diffusion. Additionally, the increased surface area enhances the amount of probe molecules that can be attached onto the sensor electrode for target capture. This property makes dendritic structures appealing in a wide variety of applications, including catalysis[2,3], chemical sensing[4,5], and electrochemical sensing[6,7]. Historically, dendrites have typically been fabricated as dispersed particles in solution, and therefore require several final processing steps to produce a properly oriented product on an electrode surface[3,5,8].

Directed electrochemical nanowire assembly (DENA) is a one-step, high growth rate technique to produce oriented, single-crystal metallic nanowires and dendrites from an electrode surface[9], eliminating the need for additional end processing steps. An alternating electric field in the presence of a salt solution induces the crystallization of the nanowires or dendrites onto an electrode in solution. The direction of growth and orientation of the structure is determined by the electric field and electrode configuration[10,11]. DENA was first performed by Cheng et al.[12] for the growth of Pd

nanowires; since then, DENA has been utilized for the fabrication of nanowires and dendrites composed of various metallic crystals such as Ag[5], Au[1], Pt[13], Cu[14], and In[15]. Recently, dendritic structures have been applied in electrochemical biosensing for the detection of disease biomarkers[16]. For example, Kelley et al.[17] demonstrated sensitive and specific electrochemical detection of the cancer biomarker CA-125 with dendritic structures ranging from 30 to 100 μm in size and exhibiting a detection range of 0.1 to 100 U/ml. This range and limit of detection is comparable to the standard ELISA method of protein detection. Moreover, these micron-scaled dendritic structures are capable of being integrated into multiple arrays on a single chip, allowing for multiplexed detection of multiple disease markers. Kelley et al.[18] also created a panel for nucleic acid cancer biomarkers on a multiplexed dendritic electrode platform. The dendritic array demonstrated simple, highly sensitive detection of mRNA from several prostate tumor cell lines with lower limits of 10 ng mRNA, and in under a 1 h total processing time.

Here, we applied DENA to fabricate nanostructured gold dendrites on varying base substrates and evaluated dendritic-based arrays as electrochemical sensors for the detection of disease biomarkers. A typical dendritic array used in electrochemical sensing is depicted in Figure 4.1.1. ELISAs were performed using cholera toxin (CT) as the benchmark disease biomarker and were electrochemically detected utilizing pulsed voltammetry methods on the dendritic arrays.

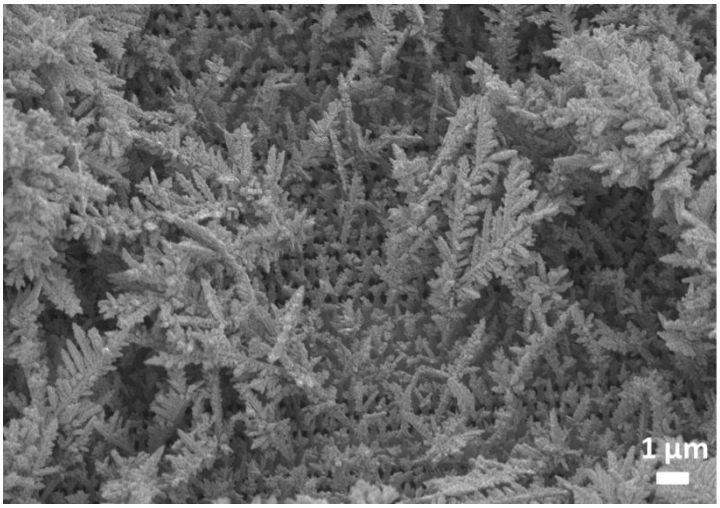

Figure 4.1.1. SEM of gold nanostructured dendrites fabricated by DENA on an Au-coated Si pillar array.

4.2 Fabrication of dendritic arrays

Dendritic arrays were fabricated using directed electrochemical nanowire assembly (DENA). Au-coated base substrates served as the working electrode (WE) onto which dendrites were grown; these base substrates included planar Au, Au-coated Si pillar arrays, and the inner Au core of previously described nanocoaxial structures (Ch. 3). DENA was performed using a square waveform and alternating current, with the substrate submerged in 30 mM chloroauric acid ($HAuCl_4$) solution across from a counter electrode (CE). The CE was composed of either a Pt wire or a planar Au chip in all DENA processes, depending on availability. Distance between the working and counter electrodes was varied for optimal dendritic growth, as discussed later in Section 4.5. The waveform was carried out with a frequency of 30 MHz, an amplitude of 5 V_{pp}, an offset of -1.25 V_o, a phase of 0, and a duty cycle of 50% for 20 min. A schematic of the square waveform is illustrated in Figure 4.2.1a. The working electrode (WE) was negatively biased by the voltage offset in order to seed and promote dendritic crystalline growth of Au^{3+} cations at the base gold substrate. Frequency, amplitude, and offset were varied to determine the optimal parameters, as discussed below. However, the above parameters were determined optimal for dendritic growth, and are the parameters used in the following experiments unless otherwise stated.

Two different setups were utilized with which to perform DENA processes. Initially, dendritic structures were grown on the micro-scale setup as illustrated in Figure 4.2.1b. Wells were attached to substrates prior to dendrite growth in order to form a reagent reservoir for the ~100 µl of $HAuCl_4$ solution used during DENA. An external Pt wire

served as the CE and was set in the well at a distance of 100 μm from the WE. Later growth conditions were performed on a macro-scale setup, schematically represented in Figure 4.2.1c. The gold substrate was placed vertically in ~25 ml of $HAuCl_4$ solution across from a CE (e.g. Pt wire, planar Au) at a distance of about 25 mm. In this setup, DENA was performed prior to well attachment; this allowed for SEM analysis of DENA samples to confirm dendrite fabrication prior to any electrochemical measurements. With the micro-scale setup, dendritic structures could only be interrogated via SEM after biological assays were performed and the well had been permanently removed.

Dendrites were grown on different starting base substrates in order to fabricate either planar dendritic arrays or 3D dendritic arrays. Au-coated planar Si was used as the base substrate to create planar dendrites. An SEM of planar dendrites is shown in Figure 4.2.2a. On the other hand, Au-coated Si pillars (Figure 4.2.2b) were used as the base substrate to fabricate 3D dendrites. An SEM of 3D dendrites is depicted in Figure 4.2.2c. Planar dendrites tended to exhibit flatter, more granular, and more widespread growth; 3D dendrites grew in a more upward fashion, with crystals extending tens to hundreds of microns above the pillar base. Planar dendrites were characterized by a bulky "boulder" look, whereas the 3D dendrites resembled "trees" rooted on the pillar tips. The difference in structure can be attributed to electric fields that concentrate at sharp edges and points. On the planar substrate, the electric field is evenly distributed due to the absence of points or edges, and therefore promotes unbiased dendritic growth throughout the entire sample. This resulted in the observed flat, widespread dendrite growth characteristic of planar base samples. Conversely, the pillar arrays provided a concentrated electric field at the

tips of each pillar, favoring dendrite growth solely at the pillar tips. This is further corroborated by the lack of any dendritic growth at the base of the pillars in the 3D dendrite samples.

Dendritic growth could be initially confirmed by eye; the substrate exhibited a rust-like color on the area where DENA has been performed. This color change can be seen in Figure 4.2.3a where 3D dendrites have been grown on a Au-coated Si pillar array. The well has been removed, leaving behind a residual epoxy ring and revealing a dark brown region of dendrites. The physical change in sample appearance is striking in comparison to the pillar region outside of the well's epoxy ring. To prepare samples for electrochemical measurements, dendritic array areas were encapsulated within a polypropylene well using SU-8 epoxy for reagent containment. Additionally, gold wire was attached to the chip on an area outside of the array area using silver epoxy. The wire was used to connect arrays in a circuit for electrochemical measurements. A 3D dendritic sample that is fully prepared for electrochemical assays is depicted in Figure 4.2.3b.

SEM was used to examine the growth and structure of the fabricated dendrites. Dendritic growth was defined by uniform coverage of dendritic structure across the entire sample area as seen in Figure 4.2.4a. Additionally, growth was characterized by highly branched structures that were tall and highly extending (Figure 4.2.4b). Well-fabricated 3D dendrites exhibited extending structures that were tens to hundreds of microns tall above the pillar base. Conversely, limited dendritic growth demonstrated non-uniform, sparse coverage of the substrate area. As shown in Figure 4.2.4c, dendrite growth is varied

throughout the sample; denser growth is concentrated around the outer circumference, and sparse growth is located in the central region of the substrate. Additionally, low growth resulted in very limited branching of dendrites, and non-extending structures as seen in Figure 4.2.4d. 3D dendrites were drastically shortened when conditions produced limited growth. Optimization of conditions to routinely fabricate uniformly covered samples with highly-branched, highly-extending dendrites is discussed in Section 4.5.

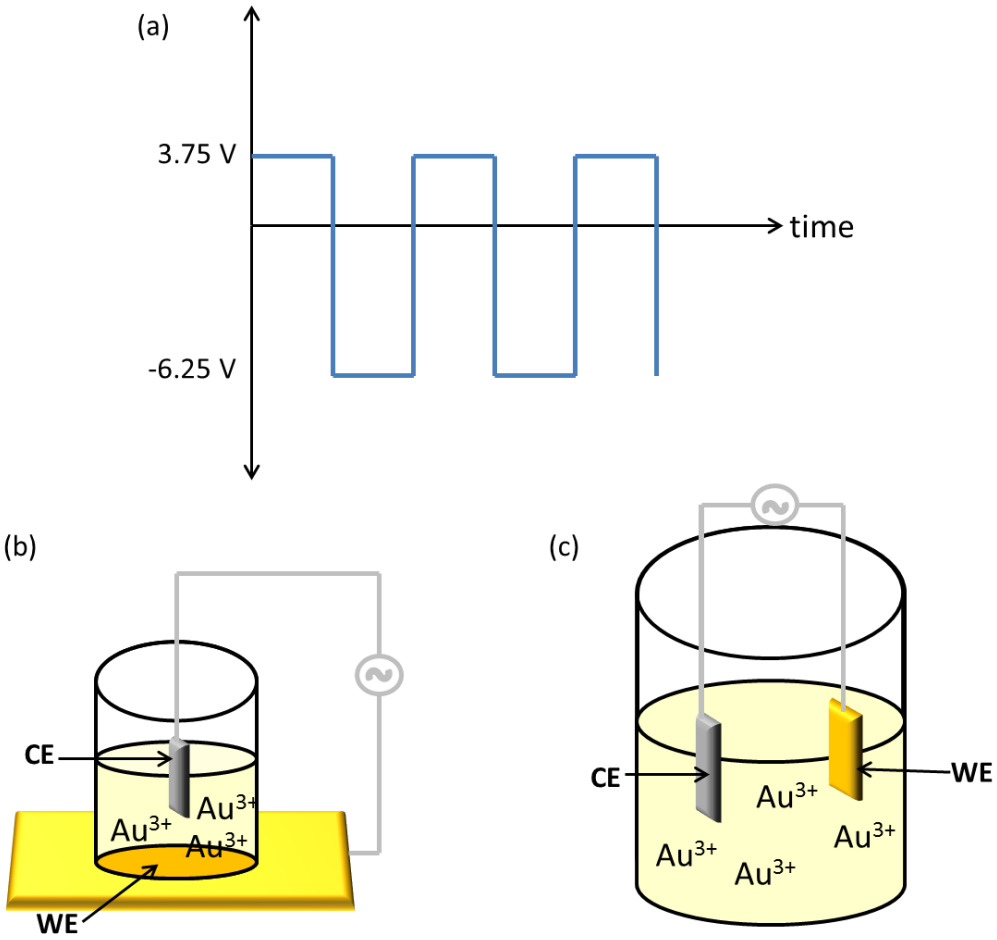

Figure 4.2.1. DENA fabrication scheme. (a) Schematic of a typical square waveform used during DENA with an amplitude of 5 V_{pp}, an offset of -1.25 V_o, a phase of 0, and a duty cycle of 50%. (b) Micro-scale setup for dendritic growth on a gold WE (e.g. planar, pillars) with an external Pt wire functioning as the CE. (c) Macro-scale setup for dendritic growth on a gold WE (e.g. planar, pillars) with a parallel CE (e.g. Pt wire, planar Au).

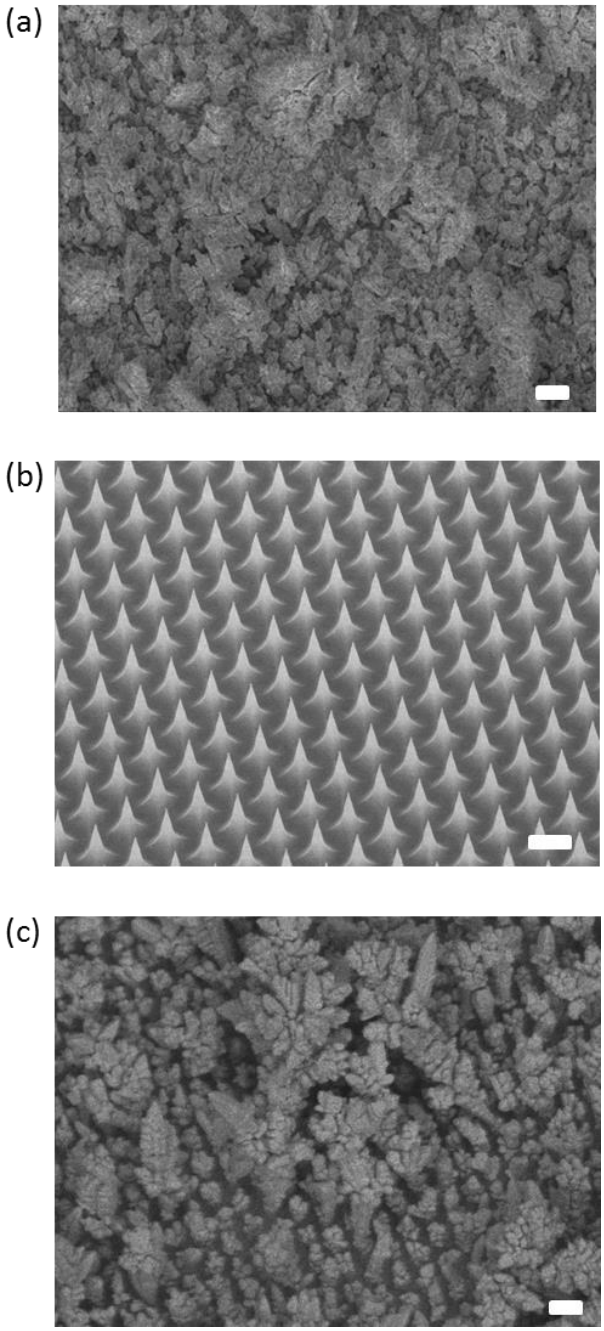

Figure 4.2.2. SEMs of dendritic samples fabricated by DENA. (a) Planar dendrites grown on a Au-coated planar Si substrate. (b) Au-coated Si pillar array with pillars 2 μm in height that served as the base substrate for 3D dendrites. (c) 3D dendrites grown on a Au-coated Si pillar array. Scale bars represent 1 μm. SEMs taken at 30° tilt.

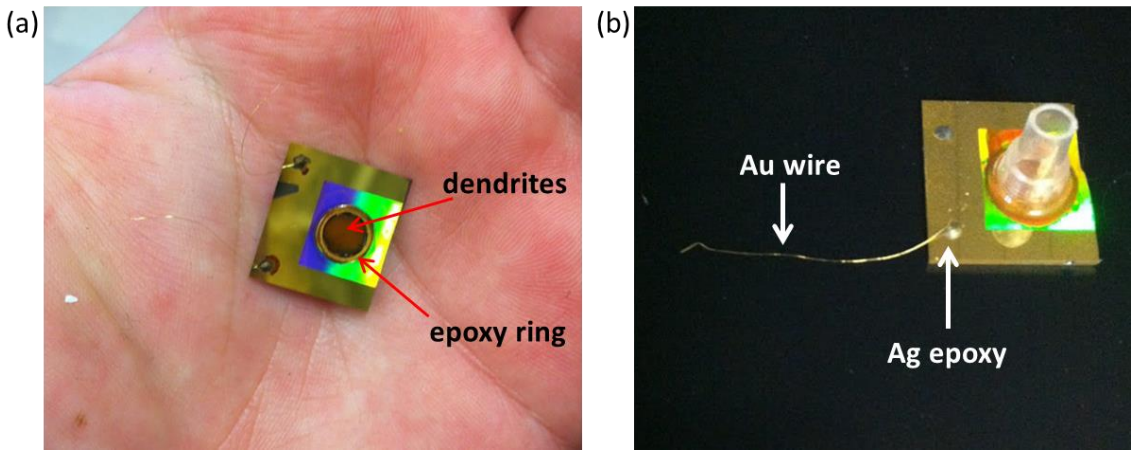

Figure 4.2.3. Dendritic sample preparation. (a) A 3D dendritic sample after DENA has been performed and the well has been removed. A residual ring of epoxy has been left behind from the well removal. Dendritic growth can be visualized by eye due to the presence of a rusty color (in the circular area). (b) A 3D dendritic array prepared for electrochemical measurements. A polypropylene well was attached over the array area for reagent containment. Gold wire was attached to the chip on an area outside of the array using Ag epoxy.

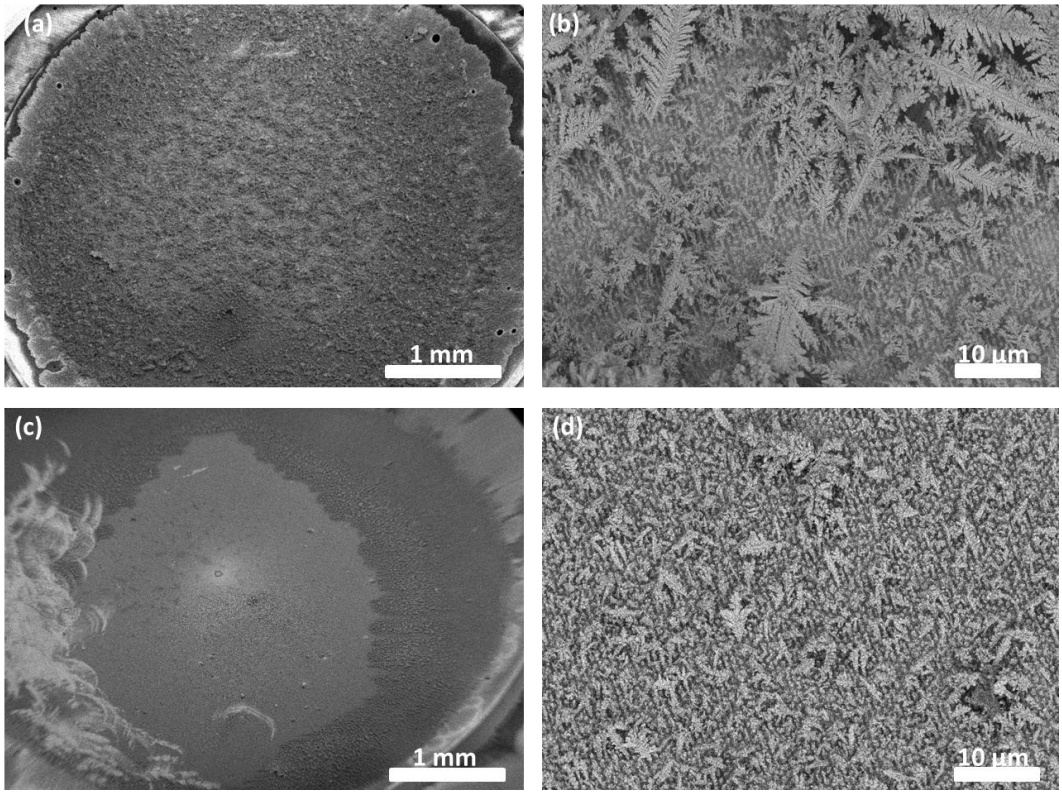

Figure 4.2.4. SEMs of variations in dendritic growth. (a) Dendritic growth signified by uniform, dense coverage throughout the entire base area. (b) Highly branched and highly extending growth characteristic of a well-fabricated dendritic sample. (c) Poorly fabricated dendrite structure with non-uniform growth; dense growth is concentrated to the outer rim of the area, with sparse growth observed in the middle of the base area. (d) Poor growth exhibits limited branching and non-extending, shortened structures. All samples shown are 3D dendrites grown on Au-coated Si pillar base arrays. SEMs taken at 30° tilt.

4.3 Dendrites for electrochemical sensing

Electrochemical measurements with dendritic arrays were performed using a three-electrode system (Fig. 4.3.1a). The dendritic array functioned as the WE, an external Pt wire functioned as the CE, and an external Ag/AgCl electrode served as the reference electrode (RE). Differential pulse voltammetry (DPV) was chosen as the method for electrochemical analysis due to its suppression of background current and high sensitivity[19]. A typical DPV waveform for the oxidation of the redox species ferrocenecarboxylic acid (FCA) is depicted in Figure 4.3.1b. Potential is swept across a specified range as a series of pulses and the resultant current is observed. Ideally, current should remain unchanged until a redox reaction occurs, resulting in the peak around 0.3 V (as observed in Figure 4.3.1b) which is the characteristic potential of FCA oxidation. By convention, an oxidation reaction at the WE produces an anodic current and the current is therefore designated negative. Conversely, a reduction reaction produces a positively denoted cathodic current. In the following studies, DPV was performed with previously optimized parameters: a pulse size of 50 mV, a pulse time of 0.05 s, a step size of 2 mV, and a sample period of 0.1 s. Potential range varied depending on the redox reporter molecule used in order to encompass the oxidation potential of the molecule.

DPVs were performed on dendritic arrays with 1 mM FCA to ensure electrochemical integrity of the devices prior to biosensing applications. Arrays were set up in the 3-electrode system described in Figure 4.3.1, and 1 mM FCA in PBS, pH 7.4 was placed in the well along with the external RE and CE. All arrays had the same base area of ~12.5 mm^2 (r = 2 mm). DPVs were performed with a potential range of 0.0 and 0.5 V to

encompass the oxidation potential of FCA at 0.3 V. DPV signals for planar dendrites and 3D dendrites are shown in Figure 4.3.2, along with their planar Au and Au pillar array counterparts. Peak current was determined for each DPV signal by subtracting the current at 0.1 V from the current at 0.3 V. The planar Au control exhibited a peak current of approximately -50 μA while planar dendrites of the same base area exhibited a peak current of approximately -20 μA (Fig. 4.3.2a). Other planar Au samples tested demonstrated the same peak current, whereas planar dendrite samples exhibited peak currents ranging from -20 to -30 μA. In addition to a lower peak current, planar dendrites tended to exhibit less defined, wider peaks compared to their Au planar counterparts. However, the overall current magnitude of the planar dendrites significantly increased over the planar Au control. The planar Au baseline current hovered around -1 μA whereas the planar dendrite exhibited a baseline current around -52 μA. Additionally, the planar Au control had a current maximum of -50 μA (same as the peak current), whereas the planar dendrites displayed a current maximum of about -75 μA.

The 3D dendrites displayed a similar trend, as seen in Figure 4.3.2b. Peak currents were determined in the same manner by subtracting the current at 0.1 V from the current at 0.3 V. The Au pillar control exhibited a peak current of approximately -50 μA while 3D dendrites of the same base area exhibited a peak current of approximately -15 μA. Other tested samples exhibited similar peak currents for Au pillar arrays, whereas 3D dendrite samples exhibited a peak current range of -15 to -25 μA. 3D dendrites exhibited much less defined peaks compared to the planar dendrites as well as the Au pillar array counterpart; the peaks appeared characteristically flattened and widened, with a more

gradual rise to the current peak. Furthermore, the overall current magnitude of the 3D dendrites was significantly increased over the Au pillar control. The Au pillar array exhibited a baseline current around -1 μA whereas the 3D dendrites exhibited a baseline current around -58 μA. Additionally, the Au pillar control had a current maximum of -50 μA (same as the peak current), whereas the 3D dendrites displayed a current maximum of about -72 μA. This would suggest that the high current magnitudes observed with planar dendritic and 3D dendritic samples may be a result of the increased surface area.

Despite an observed increase in surface area in planar and 3D dendritic samples (as confirmed via SEM), electrochemical response to FCA oxidation (as measured by peak current) decreased when compared to their control counterparts. Planar Au and Au pillar arrays exhibited peak currents of approximately -50 μA; planar dendrites and 3D dendrites displayed peak currents of about -20 μA and -15 μA, respectively. One may expect an increase in surface area to correspond to an increase in electrochemical detection of FCA oxidation. However, the effective surface area that participates in electrochemical reactions may be inhibited due to diffusion limitations. FCA may not be able to diffuse into the lower areas of dendritic structures due to their large, complex and densely-packed nature. Therefore, only the top portion of dendritic structures may be participating in the oxidation of newly diffusing FCA from the bulk solution.

Furthermore, the concentrated electric fields that occur at points and edges could produce high electric fields at the branching ends of dendrites. This variation in electric field throughout the dendrite structure could potentially cause FCA to start oxidizing at earlier

potentials (before 0.3 V), specifically at the high electric fields at the point of branches. This factor, along with diffusion limitations, could account for the gradual rise of current as FCA begins to oxidize at earlier potentials, resulting in the observed flattened, broad peak at 0.3 V instead of the sharp well-defined current seen in the control samples. The absence of this broadened FCA peak in other nanostructures, such as the nanocoax, further corroborates that this is a structurally-dependent artifact.

The high baseline current and peak current values reported above were present in the DPV signals (1 mM FCA) of all dendritic samples (planar and 3D) we have fabricated. Currently, we surmise that these characteristics are a product of diffusion limitations, increased surface area, and/or the presence of a non-uniform electric field. While this is purely speculation at this point, these DPV curves of FCA oxidation can be used to confirm the presence of dendritic growth after DENA and is currently used as an electrochemical checkpoint prior to biological sensing.

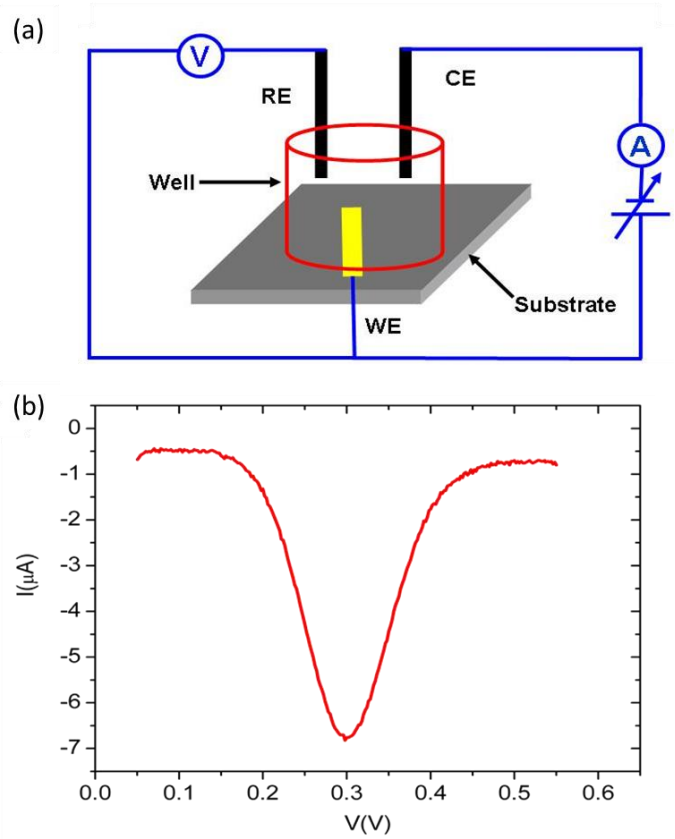

Figure 4.3.1. Electrochemical setup. (a) A three-electrode system was used: the dendritic array served as the WE, an external Pt wire served as the CE, and an external Ag/AgCl wire functioned as the reference electrode (RE). (b) Typical DPV waveform during the oxidation of 1 mM FCA. X-axis: potential (*V*); y-axis: current (*I*).

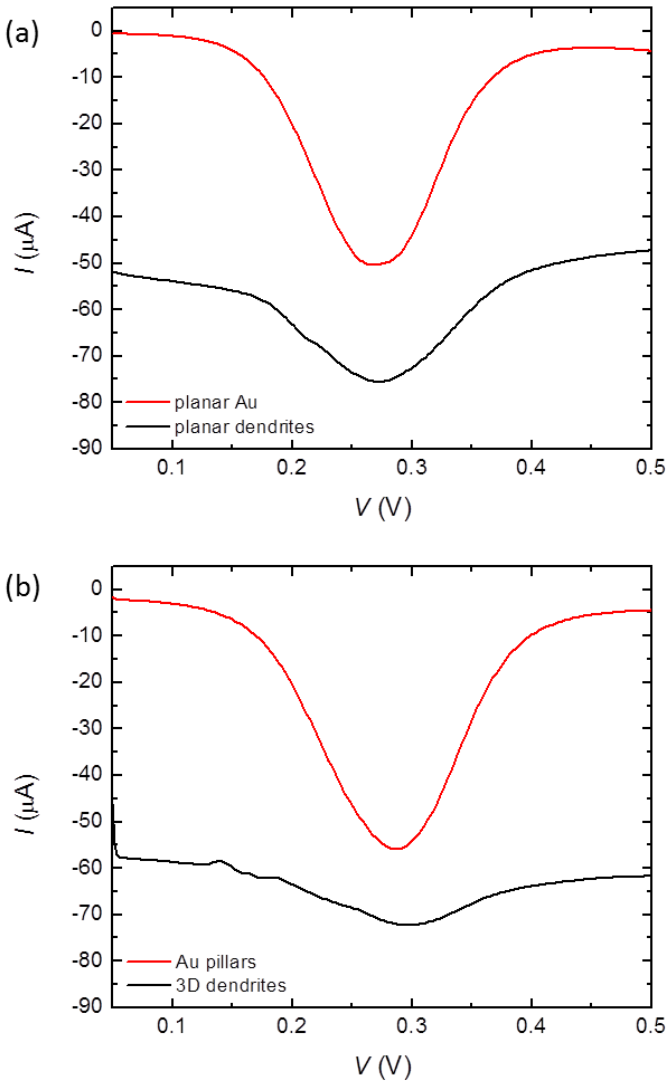

Figure 4.3.2. DPV signals of FCA oxidation on dendritic arrays. (a) DPV signal for the oxidation of FCA on planar dendrites (black) and on a planar Au control (red) of corresponding base area. (b) DPV signal for the oxidation of FCA on a 3D dendritic array (black) as well as on a Au pillar control array (red) of corresponding base area. X-axis: potential (*V*); y-axis: current (*I*).

4.4 Dendritic-based electrochemical sensors for biosensing

To demonstrate proof-of-concept for a dendritic-based electrochemical ELISA, an alkaline phosphatase (ALP) dose titration was performed and DPVs were recorded on planar dendrites. Serial dilutions of ALP were incubated with 1 mM of the enzymatic substrate p-aminophenyl phosphate (pAPP) and then electrochemically examined on planar dendrites (Fig. 4.4.1a), as well as on a planar Au electrode to observe whether the dendritic architecture affected ALP detection (Fig. 4.4.1b). Each set of titration data (planar dendrites and Au planar control) was taken on a single device. With the planar gold device, an ALP concentration of 10^{-2} ng/ml was required to measure an appreciable signal change from baseline at the -100 mV region. The planar dendrites exhibited a noticeable current peak starting at the lowest ALP concentration tested, 10^{-3} ng/ml.

To determine the range of detection, peak current (I_p) was determined from the DPV signals in Figure 4.4.1 and plotted against ALP concentration (shown in Fig. 4.4.2). The planar Au control (black) exhibited lower overall current magnitude compared to the planar dendrites (red). In addition, the planar dendrites detected ALP over all of the concentrations tested: 10^{-3} to 10 ng/ml. The planar Au counterpart detected ALP over 10^{-2} to 10 ng/ml, yet appears to be trending towards upper end saturation at 1 ng/ml. It is worth noting that a 10^{-3} ng/ml ALP concentration was not tested for planar Au due to an electrical short during the DPV measurement; however, the peak current for planar Au at 10^{-2} ng/ml ALP appears at a near zero value and is trending to a lower limit of detection. On the other hand, the planar dendrites exhibit a peak current still above 1 μA at the lowest ALP concentration tested, 10^{-3} ng/ml. Therefore, this ALP titration indicated that

the dendritic architecture was advantageous in electrochemical detection capabilities, and provided proof-of-concept for an electrochemical ELISA on dendritic arrays.

We next developed an electrochemical ELISA for the detection of cholera toxin (CT) as previously described in Chapter 3. The CT ELISA was optimized identically for both optical and electrochemical readouts. All steps were performed in the same manner, except in the final step where the reporter molecule was added; Bluephos was added for optical readout whereas pAPP was added for electrochemical readout. EDTA was chosen as the stop solution to quench the ALP reaction due to its ability to quench both optical and electrochemical ELISAs without interfering in the readout; other stop solutions examined, such as sodium hydroxide, interfered with electrochemical readout.

ELISA reactions were performed externally in a 96-well plate and completed assay supernatants were then applied to the dendritic array for DPV measurements. The ELISA was run in duplicate and DPVs were recorded separately for the first replicate (R1) followed by the second replicate (R2). CT ELISA was performed on planar dendrites and on a planar Au control; the resulting DPV signals from one replicate are shown in Figure 4.4.3. CT concentrations ranging from 10^{-2} to 100 μg/ml were examined. DPV signals were subtracted to zero at -0.25 V in order to determine peak current. The planar dendrites (Fig. 4.4.3a) exhibited a higher overall current magnitude compared to the planar Au control (Fig. 4.4.3b). However for both the planar Au and the planar dendrites, the lowest tested CT concentration of 10^{-2} μg/ml produced a distinguishable peak current from the "No CT" control baseline.

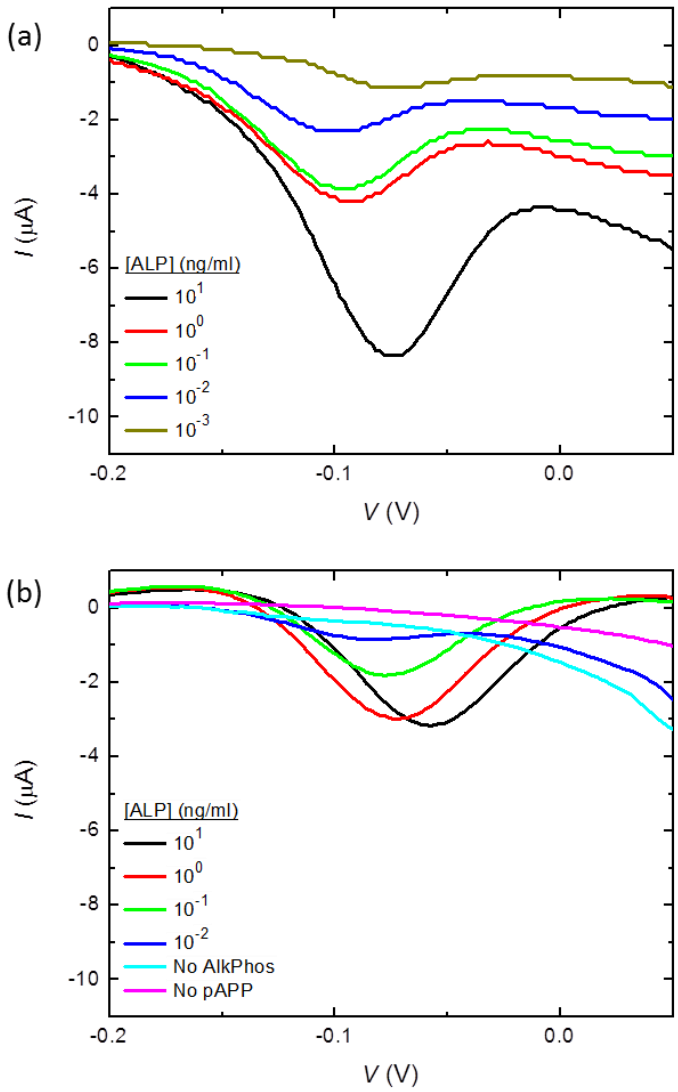

Figure 4.4.1. DPV signal of an ALP dose titration on (a) planar dendrites and (b) planar Au. Current was baselined to zero at -0.25 V to evaluate peak current. X-axis: potential (*V*); y-axis: current (*I*).

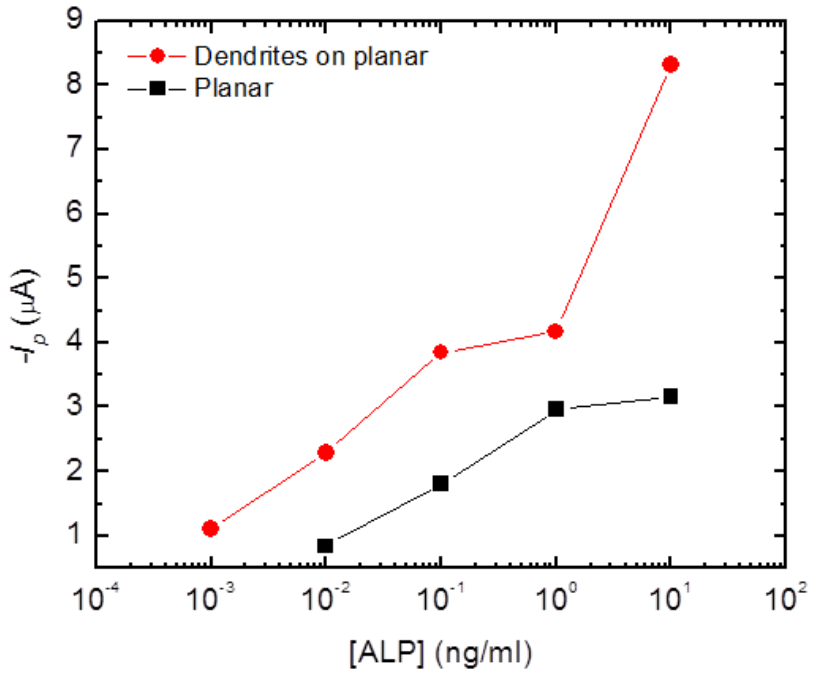

Figure 4.4.2. Detection range of an ALP titration by planar dendrites (red) and planar Au control (black). On the y-axis, peak current (I_p) was plotted against the log-scale of ALP concentration (x-axis). Peak current was determined from DPV signals in Figure 4.4.1. Data represent one trial each.

CT ELISAs were also performed on 3D dendrites and on a Au pillar control; the recorded DPV signals are shown in Figure 4.4.4. CT concentrations ranging from 10^{-2} to 100 μg/ml were examined, and DPV signal was baselined at -0.2 V to elucidate peak current. The 3D dendrites (Fig. 4.4.4a) exhibited an overall increase in current magnitude compared to the Au pillar control (Fig. 4.4.4b), yet both samples produced noticeable current peaks from the "No CT" baseline at the lowest CT concentration tested, 10^{-2} μg/ml. The DPV signals suggest that the Au pillar array appears to be trending toward saturation at the upper end, whereas the 3D dendrites can still detect higher CT concentrations.

Only the first replicates of each ELISA are shown in Figure 4.4.3 and Figure 4.4.4 and are used in the following data analysis for dynamic range determination; this was due to significant degradation of 4-AP (the final redox product of the ELISA) observed in the second replicates due to prolonged wait time before DPV measurements. A complete disappearance of DPV peaks at lower concentrations was observed in the second replicate of the planar Au control, indicating that the effect was not dendritic specific and likely due to 4-AP degradation. Therefore, the following ELISAs were performed in staggered duplicates to eliminate the discrepancy in wait time between R1 and R2.

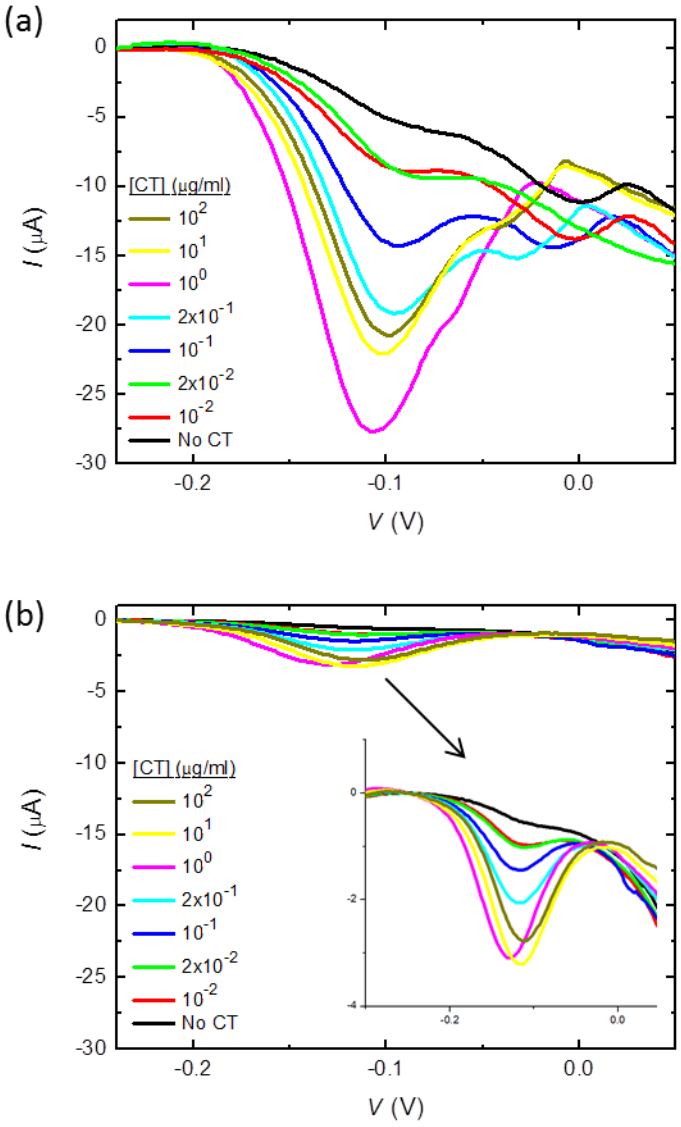

Figure 4.4.3. DPV signals of CT ELISA on (a) planar dendrites and (b) planar Au. DPVs represent the first replicate of an ELISA run in duplicate. Current was subtracted to zero at -0.25 V to determine peak current. X-axis: potential (*V*); y-axis: current (*I*).

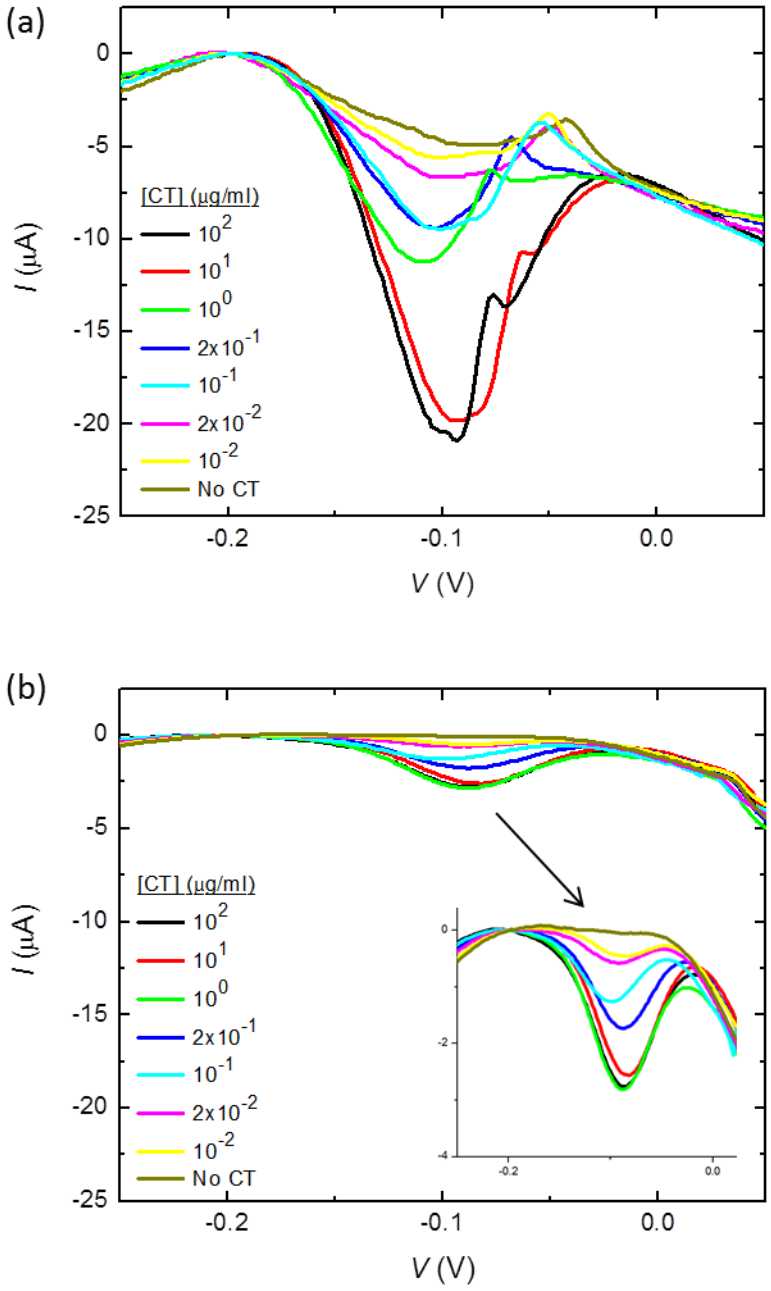

Figure 4.4.4. DPV signals of CT ELISA on (a) 3D dendrites and (b) Au pillars. DPVs represent the first replicate of an ELISA run in duplicate. Current was subtracted to zero at -0.2 V to determine peak current. X-axis: potential (*V*); y-axis: current (*I*).

To determine the dynamic range of the tested sensor arrays, peak current was plotted against the CT concentration on the log scale (Fig. 4.4.5). Peak current was determined from DPV signals in Figure 4.4.3 and Figure 4.4.4 that were baselined at either -0.25 V or -0.2 V, respectively. Planar Au (purple) and Au pillar (blue) controls exhibited overlapping peak current magnitudes and an identical range of detection. Both controls detected CT over a range of 10^{-2} to 1 μg/ml, with a log-linear region between 10^{-1} to 1 μg/ml ($R^2 \geq 0.95$); however, the curves begin to trend toward a lower end limit at 10^{-1} μg/ml. Planar dendrites (red) exhibited the same range of detection of 10^{-2} to 1 μg/ml as well as the same log-linear region between 10^{-1} to 1 μg/ml ($R^2 \geq 0.95$). However, the overall magnitude of the peak current was increased by approximately 10-fold over the Au planar control. 3D dendrites (black) had an improved range of detection over the controls and the planar dendrites. 3D dendrites were capable of CT detection over all concentrations tested: 10^{-2} to 100 μg/ml. Although the 3D dendrites do not exhibit tight log-linearity with this one replicate, they maintain a somewhat linear trend and have not yet reached a lower or upper limit.

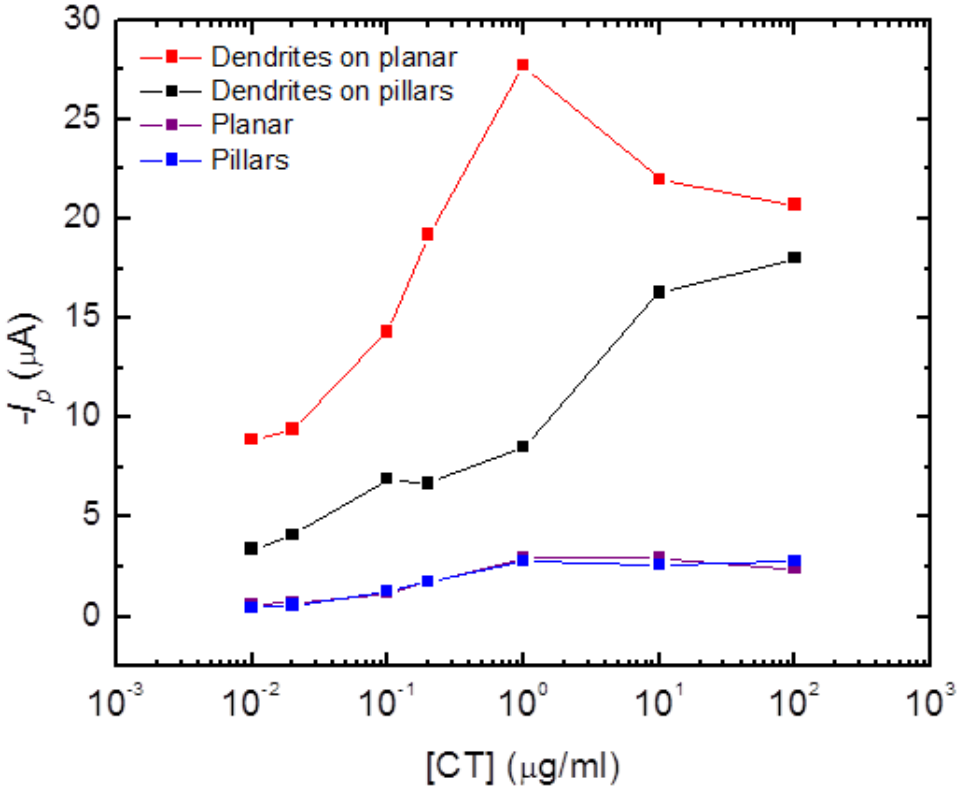

Figure 4.4.5. Detection range of CT ELISA on planar dendrites (red) and 3D dendrites (black). Planar Au (purple) and Au pillar (blue) controls were also examined. On the y-axis, peak current (I_p) was plotted against the log-scale of CT concentration (x-axis). Peak current was determined from baselined DPV signals from Figures 4.4.3 and 4.4.4. Data represent one trial each.

In addition, the electrochemical ELISA readout on dendritic arrays was compared to the conventional optical ELISA as a standard control. The optical ELISA was performed in the same manner as the electrochemical ELISA, with the exception that the BluePhos substrate was used in place of pAPP. BluePhos is converted by ALP into a colorimetric product, whose optical absorbance is read at λ_{max}=600 nm. In Figure 4.4.6, CT concentration was plotted against absorbance; the optical readout exhibited a log-linear range of detection from 10^{-2} to 1 μg/ml CT ($R^2 \geq 0.95$). Additionally, the optical ELISA does not appear to be reaching a lower limit of detection.

3D dendrites exhibited improved electrochemical detection of CT over the other electrochemical sensing devices tested (Table 4.4.1). 3D dendrites detected CT over a range of 10^{-2} to 100 μg/ml while its Au pillar array counterpart, planar dendrites, and planar Au detected CT over a range of 10^{-2} to 1 μg/ml. Additionally, 3D dendrites electrochemical readout increased the upper range of detection when compared to the optical ELISA, which exhibited a detection range of 10^{-2} to 1 μg/ml. This suggested that the 3D dendritic architecture may have the potential to improve sensitivity and extend the dynamic range of CT detection over planar dendrites and non-dendritic counterparts, as well as the standard optical ELISA. Although only one replicate was analyzed, the results suggested improved electrochemical sensing with 3D dendrites over the planar dendrites. Therefore, 3D dendritic arrays were the chosen architecture with which to progress development and characterization as an electrochemical biosensor. Following studies increased CT concentrations beyond the 10 ng/ml lower limit to discover the true LOD and range of detection; the lower end had not yet trended to a zero value in either

the electrochemical and optical readouts, suggesting that both methods are capable of CT detection beyond the range of CT investigated. Moreover, ELISA replicates were staggered to prevent degradation of 4-AP.

Staggered ELISA reactions were performed externally in a 96-well plate and completed assay supernatants were then applied to the dendritic array. The ELISA was run in duplicate with staggered replicates. All steps of the ELISA were run in parallel in both replicates until the final step: addition of 1 mM pAPP. 1 mM pAPP in TBS, pH 9 was added to the first replicate (R1), while TBST, pH 7.4 was added to the second replicate (R2). The ELISA proceeded to completion in R1, and DPVs were immediately recorded for R1. Buffer was then removed from R2 and 1 mM pAPP in TBS, pH 9 was added to complete the assay. DPVs were then subsequently recorded for R2 on the same device.

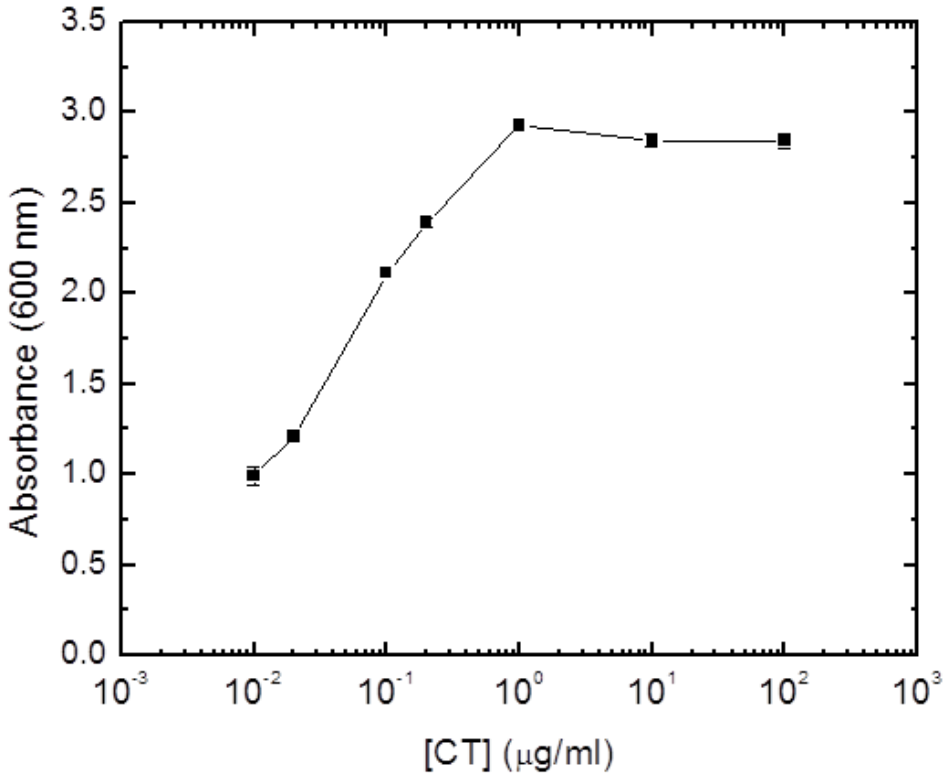

Figure 4.4.6. Detection range of optical CT ELISA. On the y-axis, absorbance at 600 nm is plotted against the log-scale of CT concentration (x-axis). Data represent two trials. Error bars represent standard deviation.

Detection Method	Lower limit	Upper limit
Optical ELISA	10 ng/ml	1 µg/ml
Planar	20 ng/ml	1 µg/ml
Planar dendrites	20 ng/ml	1 µg/ml
Pillars	10 ng/ml	1 µg/ml
Pillar dendrites	10 ng/ml	100 µg/ml

Table 4.4.1. Upper and lower limits of a CT ELISA for various detection methods.

CT ELISAs were performed in the aforementioned staggered manner on 3D dendrites, a Au pillar control array, and a planar Au control. The resulting DPV signals from one replicate are shown in Figure 4.4.7. DPV signals were subtracted to zero at -0.2 V in order to determine peak current. The planar Au and Au pillar array controls (Fig. 4.4.7a and Fig 4.4.7b, respectively) exhibited similar overall current magnitudes, whereas the 3D dendrites demonstrated a significant increase in overall current magnitude (Fig 4.4.7c).

To determine the dynamic range, peak current was plotted against CT concentration in Figure 4.4.8. Peak current was determined from baselined DPV signals in Figure 4.4.7. 3D dendrites (black) exhibited an increase in current magnitude over the planar Au (red) and Au pillar array (blue), with an approximate 4-fold increase in current at each CT concentration. 3D dendrites exhibited a log-linear range of detection over 10^{-2} to 10^{-1} μg/ml ($R^2 \geq 0.95$), and the Au pillar array and planar Au both had a log-linear range of detection from $2x10^{-2}$ to 10^{-1} μg/ml ($R^2 \geq 0.95$). All three detection platforms reached upper end saturation at 10^{-1} μg/ml. 3D dendrites exhibited a lower limit of $2x10^{-3}$ μg/ml; however Au pillar arrays and planar Au were not examined for CT concentrations lower than $2x10^{-3}$ μg/ml and 10^{-2} μg/ml, respectively, and so their true LOD could not be determined. This was due to the fact that a proper CT concentration range for ELISAs was still being investigated.

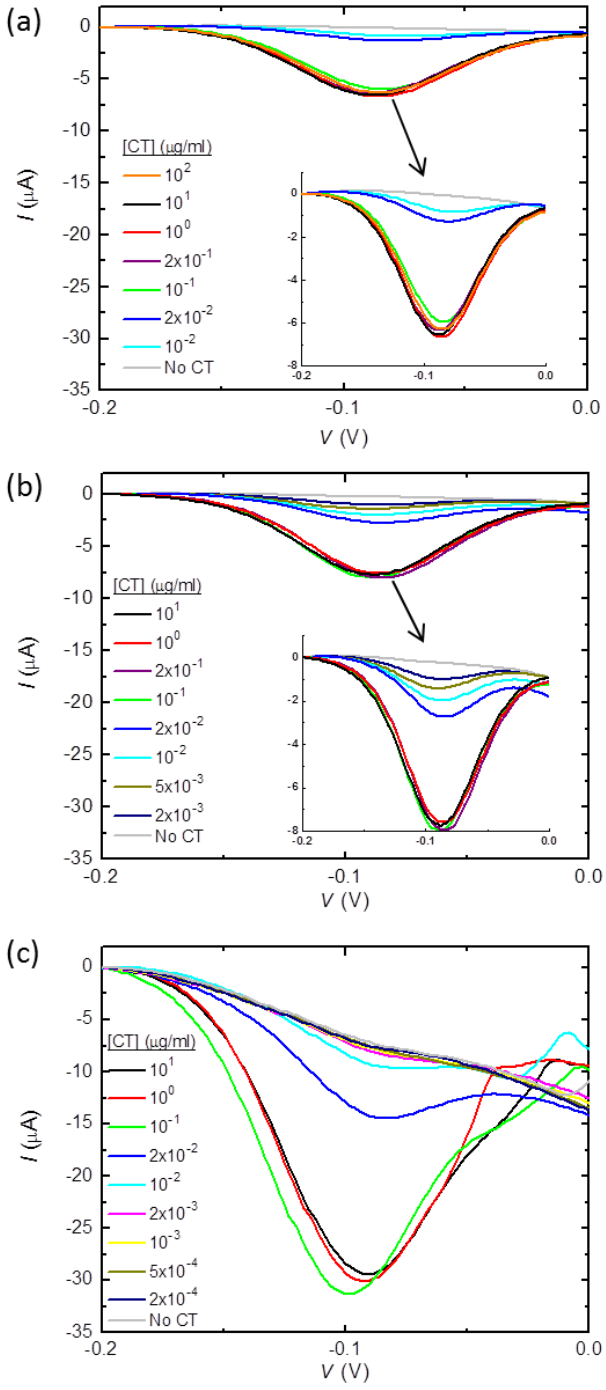

Figure 4.4.7. DPVs of a staggered CT ELISA on (a) planar Au, (b) Au pillars, and (c) 3D dendrites. DPV signals were subtracted to zero at -0.2 V to elucidate peak current. X-axis: potential (*V*); y-axis: current (*I*)

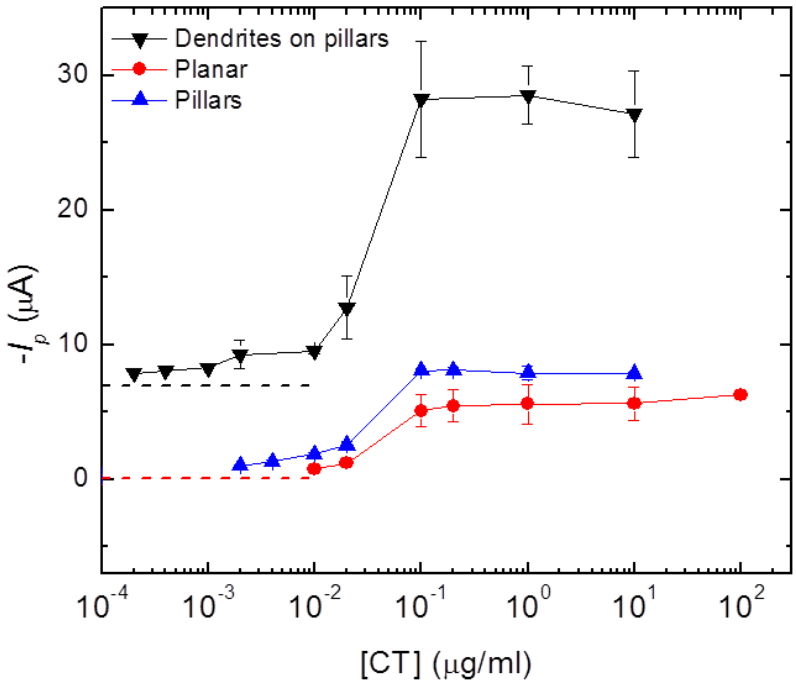

Figure 4.4.8. Detection range of a staggered CT ELISA on 3D dendrites (black). Planar Au (red) and Au pillar (blue) controls were also examined. On the y-axis, peak current (I_p) was plotted against the log-scale of CT concentration (x-axis). Peak current was determined from baselined DPV signals from Figure 4.4.7. Dashed lines represent background current ("No CT" control current value) for 3D dendrites (black line) and Au planar and Au pillars (red line). Data represent two trials run on the same device. Error bar shown is standard deviation.

A difference in the DPV baselines was observed between dendritic samples and the control counterparts. In the planar Au and Au pillar control sensors, the "No CT" background current in the baselined DPVs was approximately 0 μA at the oxidation potential of 4-AP (-0.1 V). This can be seen by the lack of an appreciable slope in the "No CT" DPV signal (Fig. 4.4.7a and Fig. 4.4.7b) as well as quantitatively by the dashed line (red) in Figure 4.4.8. On the other hand, the "No CT" background current in the baselined DPV in dendritic sensors has a non-zero value at -0.1 V. The DPV signals in the dendritic samples slope downward, giving the control and background signals (i.e. CT concentrations that do not change from the "No CT" control) an assigned, non-zero current value. This slope can be seen in the "No CT" DPV signal in Figure 4.4.7c; the non-zero background current can be seen quantitatively by the dashed line (black) in Figure 4.4.8.

This appearance of a significant downward slope was present in all dendritic-based sensors, both planar and 3D. In an I-V curve such as the DPV, the slope of the curve's baseline corresponds inversely to the resistance of the system. A negligible slope, as seen in the planar Au and Au pillar samples, indicates high resistance and therefore lower conductance. Conversely, the larger slope seen with dendritic DPVs indicates lower resistance and therefore higher conductance. While the origin of this effect is still unknown, this could suggest that the additional, nanostructured surface area of the dendritic structures increases the conductance of the electrode and reduces the resistance of the electrochemical system.

4.5 Variations in dendritic structure

Variation in the detection range of CT by 3D dendrites was observed between the previous ELISA (Fig. 4.4.5) and the staggered ELISA (Fig. 4.4.8). The initial 3D dendritic array detected CT over a range of 10^{-2} to 100 μg/ml, while maintaining a linear trend over all concentrations detected. The latter 3D dendritic array exhibited a decreased range of detection at the upper end, with a log-linear dynamic range from 10^{-2} to 10^{-1} μg/ml. To determine the cause of this discrepancy, SEMs of the two different samples were examined. SEM images of the 3D dendritic array from the first CT ELISA are shown in Figure 4.5.1. As seen in Figure 4.5.1a, dendritic growth was not uniform across the sample. The inner region, highlighted by box 1 and magnified in Figure 4.5.1b, exhibited sparse growth with short, non-extending dendrites. The outer region, designated by box 2 and magnified in Figure 4.5.1c, possesses dense, highly branched and highly extending dendrites.

The dendritic array used in the second CT ELISA displayed a different growth pattern (Fig. 4.5.2). In Figure 4.5.2a, the majority of the sample exhibited uniform growth, however this growth was limited. Figure 4.5.2b highlights the dendritic growth characteristic of the majority of the sample (box 1 in Fig. 4.5.2a); the dendrites are similar the inner region of the initial array, with sparse coverage and stubby, non-extending structures. The desired dense, highly-branched and highly-extending dendritic structures are only observed in a thin outer region, highlighted by box 2 in Figure 4.5.2a and magnified in Figure 4.5.2c.

The structural variance between these two samples may account for the discrepancy in detection range of CT. The first dendritic array demonstrated a greater range of detection, as well as a larger portion of the sample (≥ 50%) covered with highly-branched, extending dendritic structures. Conversely, the second dendritic array was dominated with sparse, limited dendritic growth and a decreased range of detection was observed. These results supported that the idea that increased, expansive dendritic growth is capable of increasing electrochemical detection. Several subsequent dendritic samples (n = 3) were fabricated in an attempt to reproduce the initial dendritic structure, however variations still existed between these samples and they more closely resembled the second, sparsely-coated dendritic array. It was apparent that proper dendritic fabrication was not reproducible between samples at this point; therefore, DENA parameters were examined to reproducibly and repeatedly produce samples with uniform coverage of extensive dendritic growth.

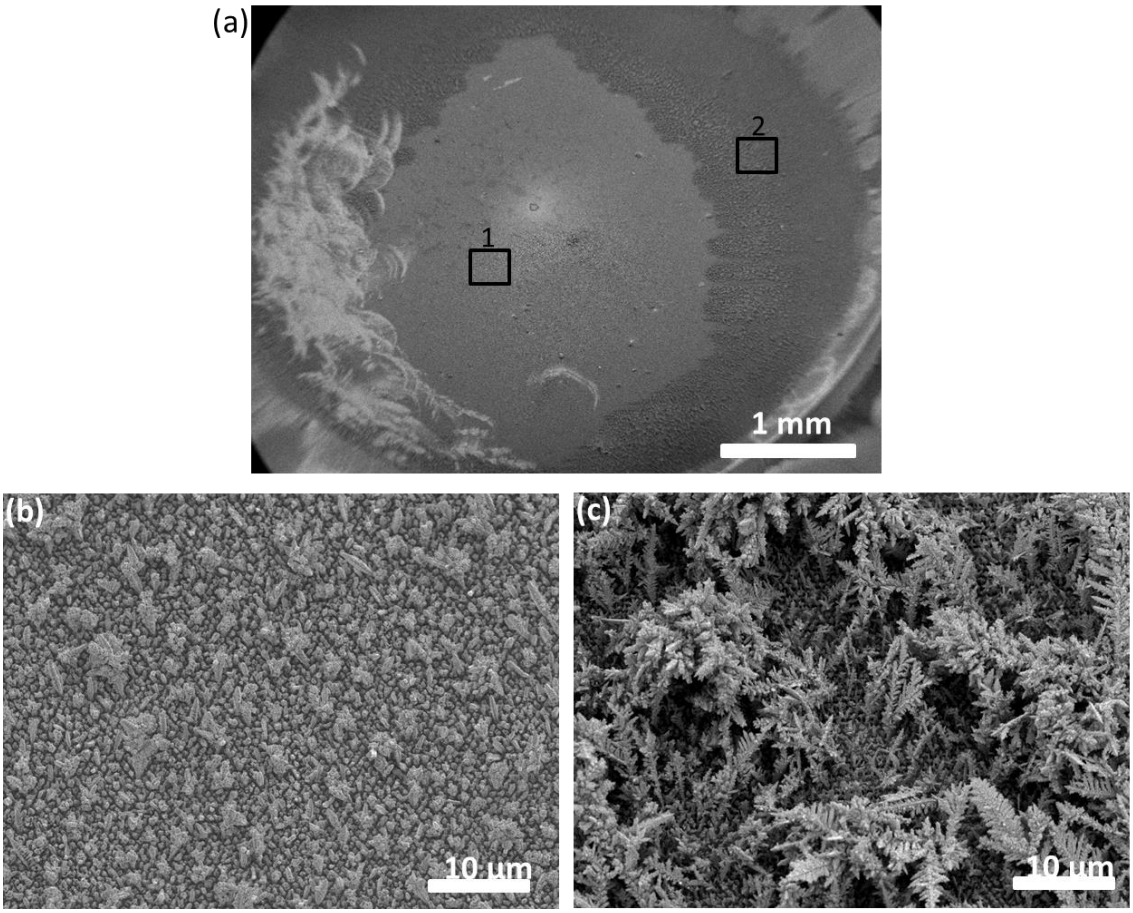

Figure 4.5.1. SEMs of 3D dendritic array used in initial, non-staggered ELISA from Figure 4.4.5. (a) SEM of entire sample area. The inner region highlighted by box 1 is magnified in (b). The outer region highlighted by box 2 is shown in (c). SEMs taken at 30° tilt.

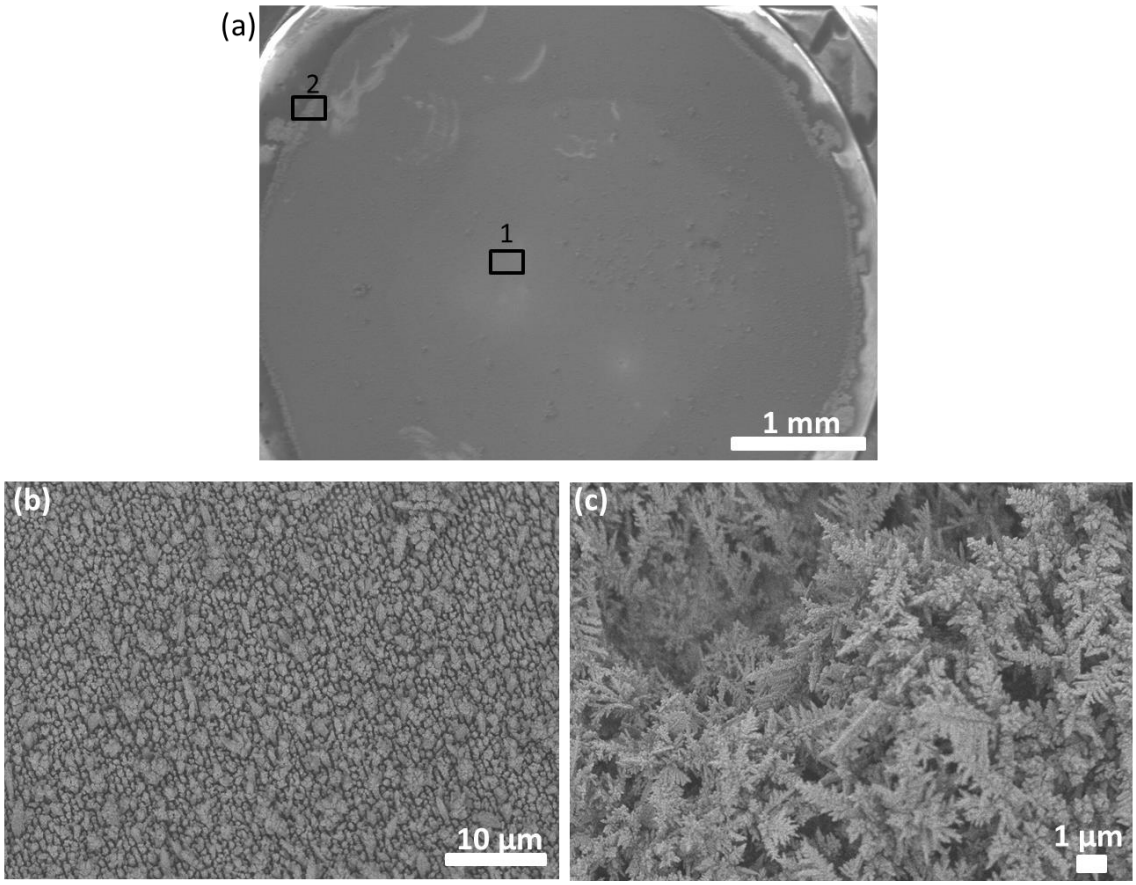

Figure 4.5.2. SEMs of 3D dendritic array used in staggered CT ELISA from Figure 4.4.8. (a) SEM of entire sample area. The dendritic structure of the majority of the sample is highlighted by box 1 and is magnified in (b). Growth in the thin outer region highlighted by box 2 is shown in (c). SEMs taken at 30° tilt.

4.6 Optimization of DENA growth parameters

Several DENA parameters were investigated and the resulting dendritic arrays were examined via SEM (Figure 4.6.1). Previously, DENA had been performed using a square waveform with the following standard parameters: a frequency of 30 MHz, an amplitude of 5 V_{pp}, a potential offset of -1.25 V_o, 50% duty cycle and 0 phase for 20 min in 30 mM $HAuCl_4$, with a WE-CE distance of 100 μm. The parameters examined included $HAuCl_4$ solution temperature, WE-CE electrode distance, and frequency.

In Figure 4.6.1a, DENA was performed with the standard parameters, however the salt solution was allowed to warm fully to room temperature (10 min) prior to dendritic growth. The salt solution is stored in 4°C, and had previously been used for DENA immediately after removal from the fridge. Under this condition, not only was uniform coverage achieved, but the dendritic growth was highly-branched and extensive across the entire sample. A control array was grown with the standard conditions and no salt solution warm up time (Fig. 4.6.1b); the solution was applied directly to the array for DENA from the fridge. No warm up time resulted in a dendritic array that had limited growth in comparison to the array with 10 min warm up. The left panel in Figure 4.6.1b indicates a reduced growth in comparison to the array in the left panel of Figure 4.6.1a. Additionally, the magnified right panel of Figure 4.6.1b displays shortened dendritic structures that are lacking the highly-branched character observed in the right panel of Figure 4.6.1a. These results indicated that the 10 min warm up time is critical, and may allow for improved diffusion of gold salt ions to the electrode surface during DENA. All following DENA processes were carried out with a 10 min warm up time.

Electrode distance between the WE and CE was also examined, as it was thought that a greater WE-CE distance may improve electric field uniformity and therefore dendritic growth. In Figure 4.6.1c, the WE-CE distance had been increased from the standard 100 μm to 5 mm, and DENA was performed after the salt solution had reached room temperature. While the growth coverage appeared uniform across the sample (as seen in the left panel of Fig. 4.6.1c), the dendritic structure was shortened and did not display elongated branching (right panel Fig. 4.6.1c). Therefore, this suggests that the standard 100 μm is the more optimal WE-CE distance for fabricating the desired, highly extensive dendrites.

Frequency of the DENA square waveform was also tested. It had previously been demonstrated that increased DENA frequency results in decreased nanowire radius and increased growth tip velocity[11]; therefore, we hypothesized that increasing the frequency may allow for thinner, taller structures. In Figure 4.6.1d, the frequency was increased form the standard 30 MHz to 50 MHz, and DENA was performed after the salt solution had reached room temp. Uniform coverage was obtained (left panel Fig. 4.6.1d) however growth appeared limited when compared to growth observed in Figure 4.6.1a. Upon magnification (right panel Fig. 4.6.1d), it was observed that the increased frequency did not improve dendrite growth over the standard 30 MHz frequency; dendrites were short and stubby, and lacked branching. Therefore, the standard frequency of 30 MHz was maintained in following DENA growth processes.

After reproducible fabrication of dendritic structures was achieved, electrochemical biosensing studies were resumed. In the following studies, dendrites were fabricated on photolithographically-patterned chips using a new macroscale set-up. DENA processes were performed with a frequency of 30 MHz, an amplitude of 5 V_{pp}, an offset of -1.25 V_o, a phase of 0, and a duty cycle of 50% for 20 min with a WE-CE distance of 100 μm. The solution concentration was kept at 30 mM $HAuCl_4$, however underwent a 10 min warm-up period prior to DENA processes. While further studies into optimizing DENA parameters should be investigated in the future, we continued to examine electrochemical sensing abilities of uniformly covered, extensively-branched dendritic samples to determine whether the dendritic architecture offered any advantage over the standard ELISA.

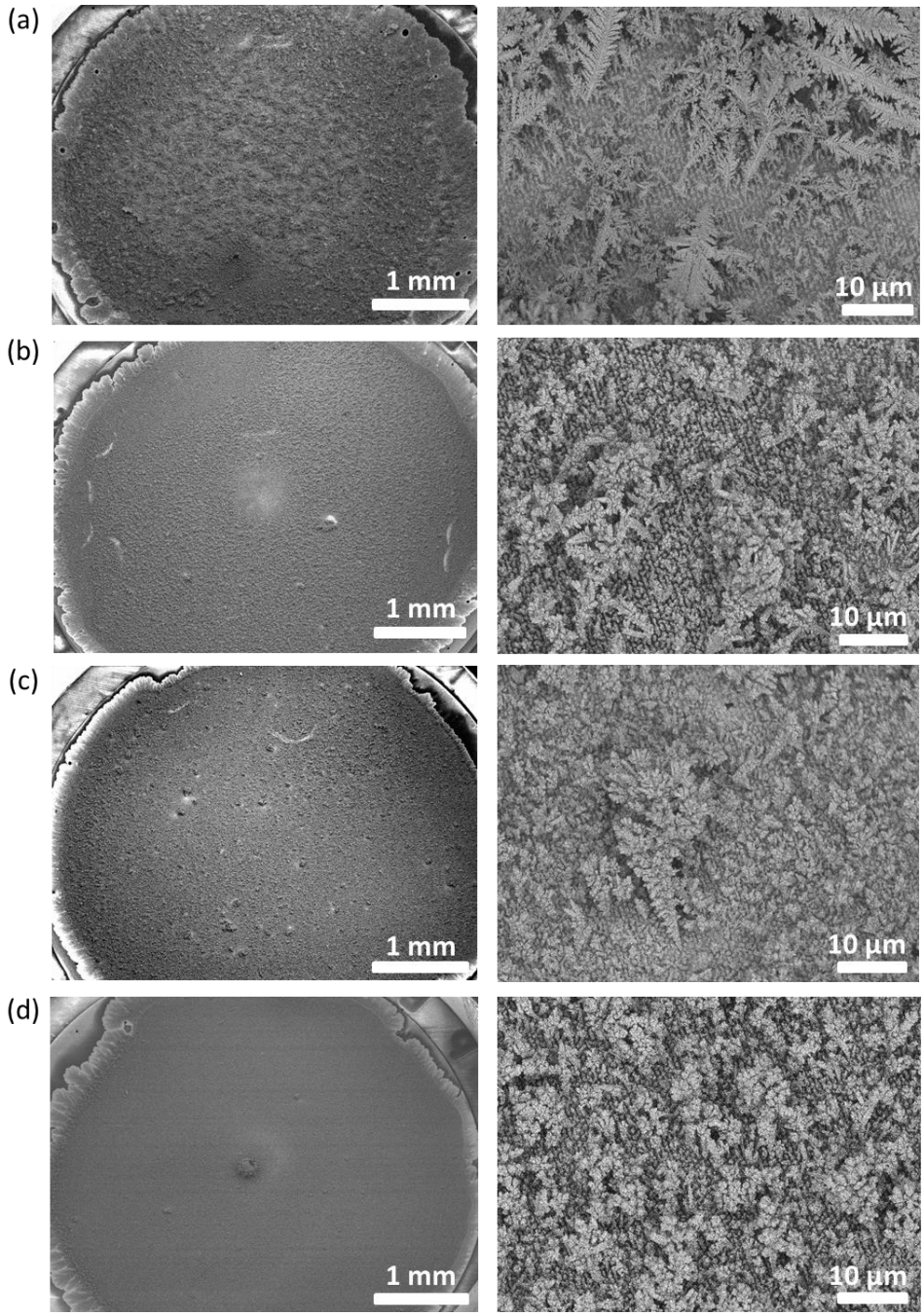

Figure 4.6.1. SEMs of 3D dendritic arrays with varied growth parameters.

Figure 4.6.1. SEMs of 3D dendritic arrays with varied growth parameters. (a) Dendritic array grown under standard conditions with a 10 min warm up for the 30 mM $HAuCl_4$ solution prior to DENA. (b) Control array grown under standard conditions and with no solution warm up time. DENA was performed with solution from 4°C storage. (c) Dendritic array grown with a distance of 5 mm between the WE and CE instead of the standard 100 μm WE-CE distance. A 10 min warm up for the 30 mM $HAuCl_4$ was included; all other parameters were standard. (d) Dendritic array fabricated with a 50 MHz frequency instead of the standard 30 MHz. A 10 min warm up for the 30 mM $HAuCl_4$ was included; all other parameters were standard. SEMs taken at 30° tilt.

4.7 Fabrication of dendritic arrays on photolithograpically-patterned chips

Following DENA procedures were performed on a new macroscale setup, as previously described in Section 4.2. Using this setup, the substrate was placed directly into the salt solution, eliminating the requirement for a well reservoir during DENA. In this manner, samples could be imaged via SEM to ensure proper growth prior to use for electrochemical ELISA measurements. Additionally, a photolithographically-patterned chip was designed in order to permit growth only in certain designated areas, as opposed to over the entire submersed chip. This would allow for several individually-addressed arrays on a single chip, which would be amenable for future biomarker multiplexing and biofunctionalization. As seen in Figure 4.7.1a, the chips consisted of eight, individually-addressed, Au pillar array regions, each with a base area of ~3 mm^2. The area outside of these regions was protected by photoresist, including the gold leads, to prevent dendritic growth during DENA. Gold pads were exposed (i.e. not covered in photoresist) in order to connect the arrays to the circuit for DENA growth. These gold pads remained outside of the salt solution, protected from DENA processes as seen in Figure 4.7.1b. The chip was designed with the future prospect of simultaneously growing dendrites on all eight regions, to ideally grow structurally identical dendritic arrays. These arrays could be biofunctionalized with ELISA antibodies to move away from the plate-based format towards a more POC prototype, as well as provide a miniaturized platform for multiplexing.

3D dendrites were grown with the macro-scale setup on one array of the patterned chip. The DENA parameters previously stated in section 4.6 were used; however in these

macro-scale studies, the WE-CE distance was ~25 mm and either a coiled Pt wire or planar Au chip were used as the CE depending on availability. SEM images confirmed proper growth, designated by uniform coverage of extensively branched dendritic structures across the sample. The SEM image in Figure 4.7.2a shows the overall region of the dendritic array. The majority of the array exhibited consistent coverage of dendritic structures ranging from tens to hundreds of microns in length (Figure 4.7.2b), except for a portion of the array on the left outer region. In this area, dendritic growth appeared denser and more extensive as seen in Figure 4.7.2c. This effect is also noted to a lesser degree around the entire circumference of the array. This is likely due to accelerated growth at the edge where the electric field is strongest, as well as unhindered access to the $HAuCl_4$ solution; inner regions of the area may be diffusion limited and competing for reagent, whereas the outer region has no other growing dendritic branches with which to share reagent or compete, allowing these outer branches to grow without any steric limitations.

Using the DENA macroscale setup, a 3D dendritic array was fabricated that was consistent with the desired growth previously acquired with the micro-scale setup. Dendritic structures were highly branched and extensive, while maintaining uniform and consistent coverage across a majority of the sample. Additionally, the targeted array was the only array that exhibited any dendritic growth despite all arrays being submerged in the solution. This indicated that the arrays were independently addressed and that the gold leads were properly protected by the photoresist. Using this photolithographically-patterned chip, multiple electrically-isolated arrays can be grown simultaneously on a

single chip, providing a platform amenable to multiplexing and a potential on-chip ELISA format in the future. Additionally, this chip allows for SEM examination and confirmation of dendritic growth prior to electrochemical measurements, unfeasible before with the micro-scale setup.

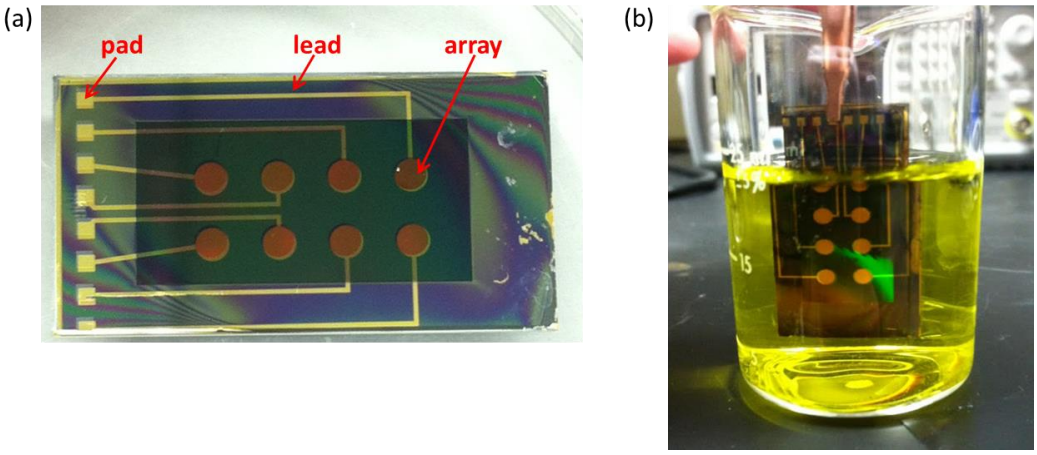

Figure 4.7.1. Photolithographically-patterned chips for 3D dendritic arrays. (a) Patterned chip containing eight, individually addressed, Au pillar arrays of base area ~3 mm^2 each. Gold leads connect each array to a respective gold pad. The gold leads are protected by photoresist; the arrays and pads remain exposed for either dendritic growth or connection to the circuit, respectively. Dimensions of entire chip area are 16 x 30 mm^2. (b) Patterned chip in the macro-scale setup for DENA. Exposed Au pillar arrays are submerged in 30 mM $HAuCl_4$; the gold pad corresponding to the array targeted for DENA growth is connected by an alligator clip to the circuit.

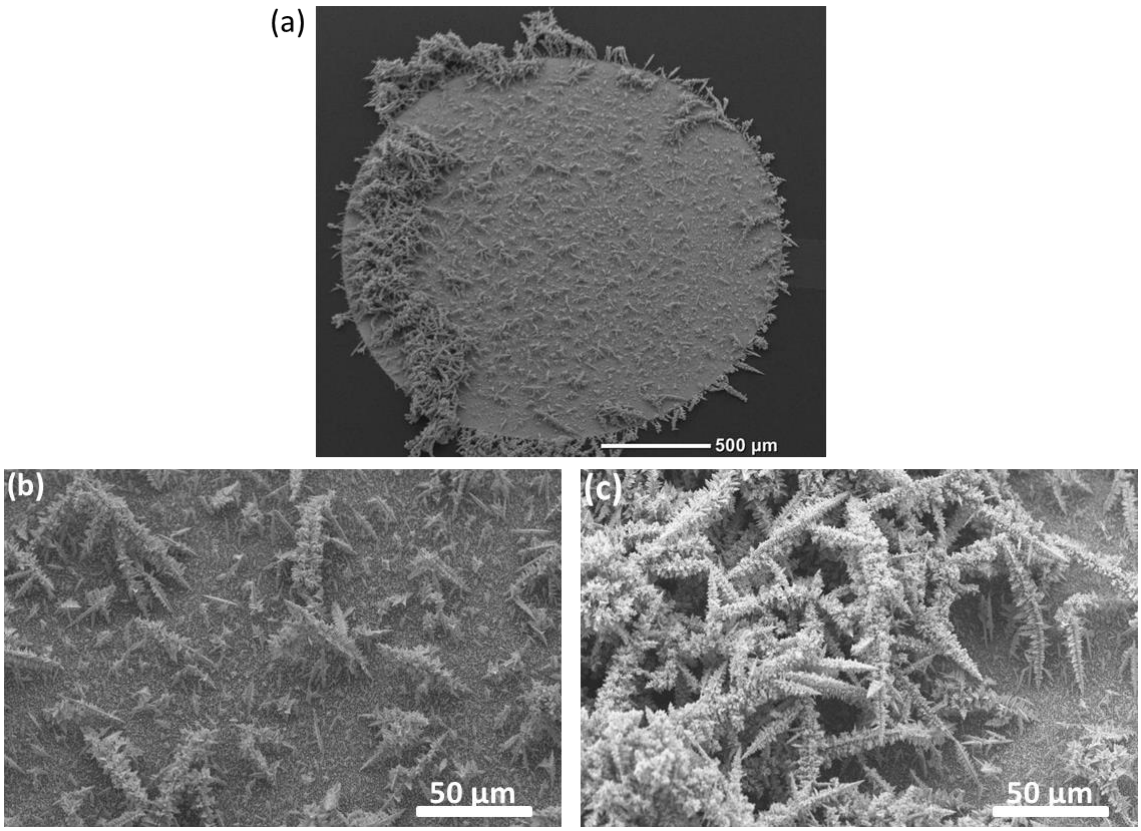

Figure 4.7.2. SEMs of a 3D dendritic array on a photolithographically-patterned chip. (a) Entire region of dendritic array with base area ~3 mm^2. (b) Dendritic growth characteristic of inner region as well as the majority of the sample. (c) Dendritic growth characteristic of the outer left region of the array, as well as dendrites lining the circumference of the array. SEMs taken at 30° tilt.

4.8 Dendritic-based biosensors using photolithographically-patterned arrays

After SEM confirmation of proper dendritic growth on photolithographically-patterned chips, well reservoirs were attached around each array (as previously described in Section 2.5.1) and electrochemical ELISAs were performed. CT concentration range was expanded from previous ELISAs in order to determine the true dynamic range and LOD of dendritic-based sensors. ELISAs were performed in duplicate and both replicates were electrochemically measured concurrently on the same device. Identical CT concentrations in both replicates were measured in parallel as opposed to measuring all of R1 first and then R2 as was done with a staggered ELISA. Degradation effects of 4-AP between replicates were significantly minimized in this manner. In addition, any variation in the addition of pAPP to R1 and R2 in staggered stages was eliminated.

DPV signals of a CT ELISA were recorded with a 3D dendritic array (Fig. 4.8.1a), as well as with a Au pillar control array (Fig. 4.8.1b). CT concentrations ranging from 10^{-4} to 10 μg/ml were examined. DPV signals were baselined to zero at -0.2 V in order to determine the peak current in the -0.1 V region. With the Au pillar control, a CT concentration of 10^{-2} μg/ml was required in order to measure an appreciable signal change from baseline. However, the 3D dendritic array exhibited a noticeable peak current from baseline starting at $2x10^{-3}$ μg/ml CT.

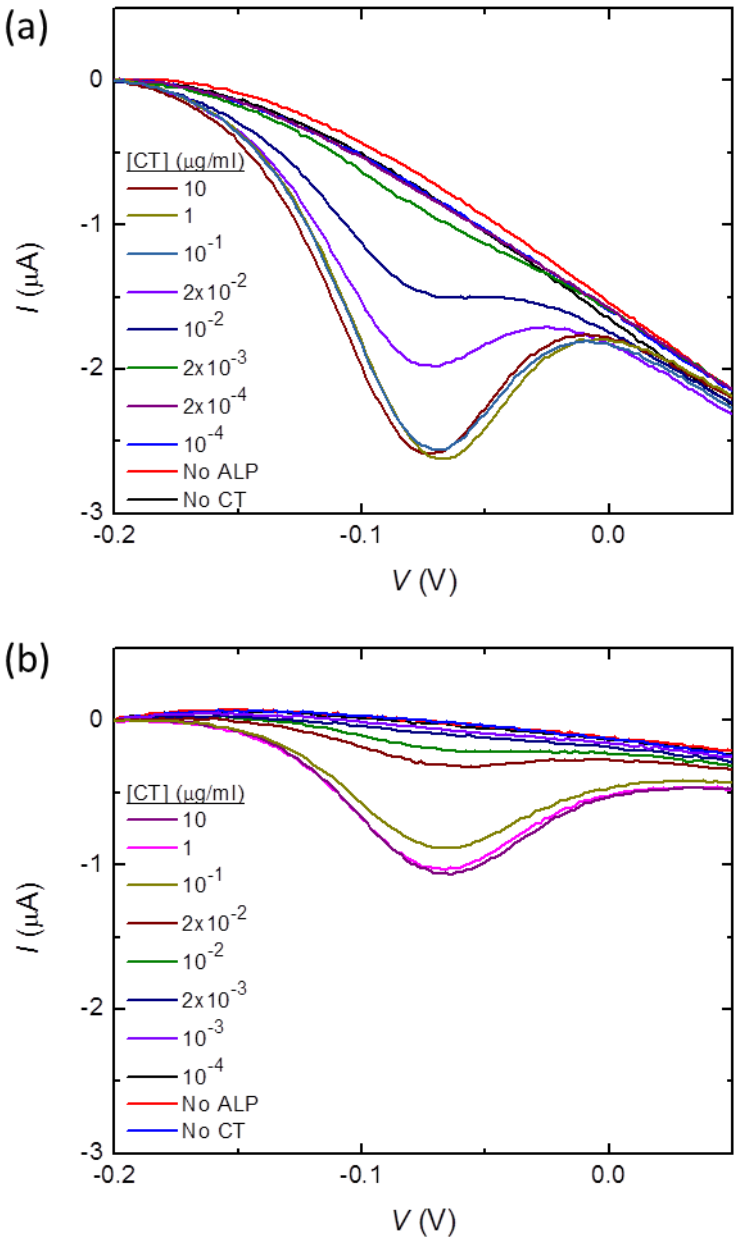

Figure 4.8.1. DPVs of CT ELISA on a photolithographically-patterned chip containing (a) 3D dendritic array and (b) a control Au pillar array. DPV signals were subtracted to zero at -0.2 V to determine peak current. Data represent one replicate of CT ELISAs run in duplicate. X-axis: potential (*V*); y-axis: current (*I*).

To determine the dynamic range, peak current was plotted against the CT concentration on the log scale in Figure 4.8.2. Peak currents (I_p) were determined from baselined DPV signals in Figure 4.8.1. Dashed lines correspond to the average current value of the "No CT" control and lower CT concentrations that did not produce a peak current from baseline. The Au pillar array control (blue) exhibited a lower overall current magnitude compared to the 3D dendritic array (black). Additionally, the 3D dendritic array demonstrated a greater log-linear dynamic range, over the CT concentrations of $2x10^{-3}$ to 10^{-1} μg/ml ($R_2 \geq 0.95$). The Au pillar control, on the other hand, exhibited a log-linear dynamic range over the concentrations of 10^{-2} to 10^{-1} μg/ml CT ($R2 \geq 0.95$). The dendritic architecture increased the sensitivity of the detection by an order of magnitude, improving the pillar array LOD from 10^{-2} to 10^{-3} μg/ml with the dendritic array.

Here, we observed the sloping DPV baseline associated with previous dendritic samples in the 3D dendritic array on the photolithographically-patterned chip. The Au pillar array produced a relatively non-sloping baseline as seen in previous control samples. Dendritic samples on the patterned chip maintained the low resistance and high conductance seen with prior dendritic samples fabricated with the micro-scale setup. Additionally, the 3D dendritic array on the patterned chip improved the lower end detection range of CT by an order of magnitude over 3D dendrites fabricated in the micro-scale setup. Initial CT ELISAs on micro-scale fabricated 3D dendrites exhibited a log-linear range of detection of 10^{-2} to 100 μg/ml CT. On the other hand, the patterned 3D dendritic array detected CT over a log-linear range of $2x10^{-3}$ to 10^{-1} μg/ml. This could be due to the smaller dendritic footprint in the overall area contained by the well reservoir on the patterned chip; the

dendritic array has a base area of 3 mm^2 but the well reservoir encapsulates an area of ~12.5 mm^2. Therefore, there is extra room around the array in which reagent can diffuse to the sides of the outer edge dendrites on the array circumference. This property may allow for improved diffusion of redox reporter to the outer side portion of the array, increasing the lower end level of detection. In the previous set-up, however, the entire area encapsulated by the well reservoir was covered with dendritic growth (~12.5 mm^2), limiting reagent diffusion to the top of the array only. Further studies should be conducted in which pillar spacing is increased to find the ideal "sweet spot", where reagent is free to diffuse around each dendrite and is not hindered by surrounding dendritic growth, yet the advantage of increased surface area is maintained.

Electrochemical detection with the 3D dendritic sensor was compared to the conventional optical ELISA as a standard control. The optical ELISA was carried out in duplicate and the results are shown in Figure 4.8.3, with absorbance plotted against CT concentration. The dashed line corresponds to the average absorbance value of the "No CT" control. The optical readout was log-linear over a dynamic range of 10^{-3} to 10^{-1} μg/ml ($R^2 \geq 0.95$), with a LOD of 10^{-3} μg/ml. Electrochemical detection was log-linear over the dynamic range of $2x10^{-3}$ to 10^{-1} μg/ml ($R^2 \geq 0.95$) and exhibited a similar LOD of $2x10^{-3}$ μg/ml. These results indicated that the dendritic electrochemical sensor is comparable to the standard optical ELISA, exhibiting a log-linear dynamic range of detection over the same 2 orders of magnitude (10^{-3} to 10^{-1} μg/ml) and a LOD on the same order of magnitude (10^{-3} μg/ml).

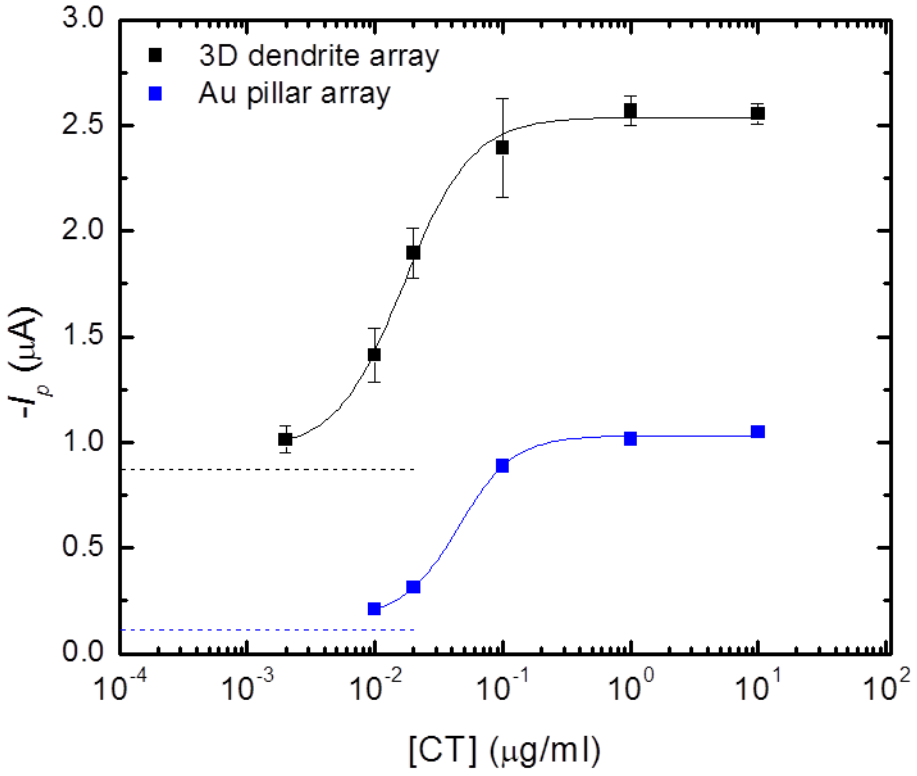

Figure 4.8.2. Detection range of CT ELISA on photolithographically-patterned 3D dendritic array (black). A control Au pillar array (blue) on the same chip was also examined. On the y-axis, peak current (I_p) was plotted against the log-scale of CT concentration (x-axis). Peak current was determined from baselined DPV signals from Figure 4.8.1. Dashed lines correspond to the average current of the "No CT" and lower CT concentrations that did not produce a peak current. Data represent two trials run on the same device. Error bar shown is standard deviation.

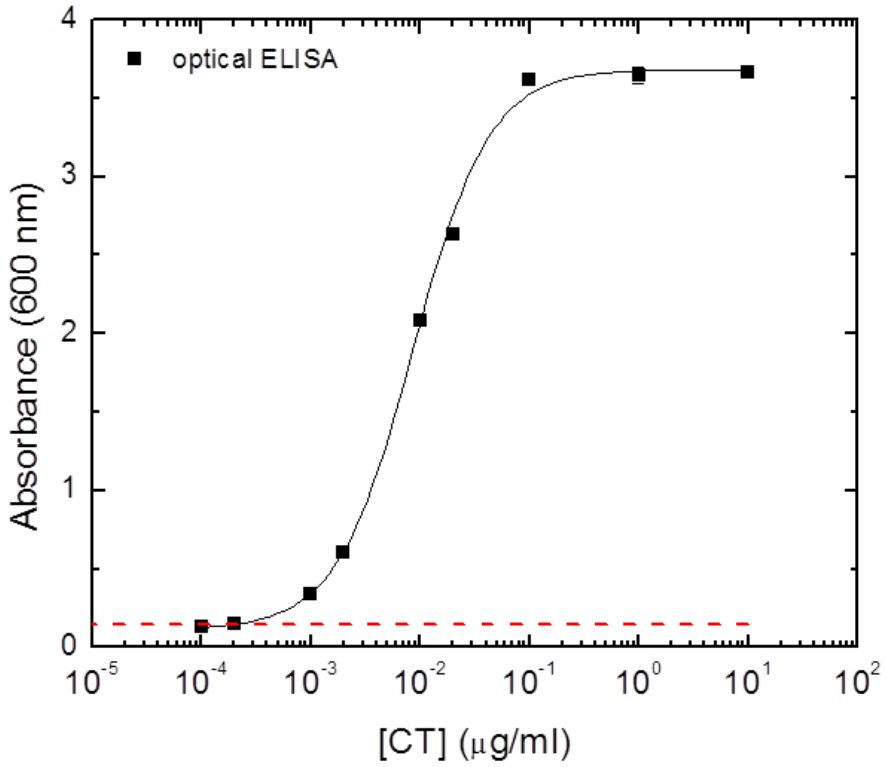

Figure 4.8.3. Detection range of optical CT ELISA. On the y-axis, absorbance at 600 nm is plotted against the log-scale of CT concentration (x-axis). Dashed red line corresponds to average absorbance value of the "No CT" control. Data represent two trials. Error bar represent standard deviation.

4.9 Future directions: biofunctionalization and dendritic ECC sensors

We have demonstrated dendritic electrochemical detection of cholera toxin (CT) with sensitivity comparable to the conventional optical readout. However, to be further developed into a POC device, ELISA antibodies must be conjugated to the dendritic surface in order to move away from the plate-based format towards a portable device. Conjugation of antibody directly to the electrode surface would eliminate diffusion limitations previously observed. Pillar spacing could also be adjusted to a greater pitch (i.e. more space between pillars) to additionally aid in overcoming diffusion issues. Several biofuncationalization strategies have been assessed and characterized for the conjugation of protein to planar gold as well as Au pillar arrays. In the future, these protocols will be applied to functionalizing 3D dendritic arrays with antibodies to produce a dendritic, on-chip electrochemical ELISA.

We have recently utilized DENA to grow dendritic structures onto nanocoaxial structures in an attempt to increase electrochemical detection sensitivity. Extended core coaxes (ECCs) were prepared as previously described in Section 3.6 and resulting ECC structure was verified via SEM (Figure 4.9.1a). DENA was performed with the macro-scale setup on the ECC array, using the inner gold core as the working electrode and an external planar Au chip as the counter electrode. DENA was executed with the same parameters as before, except the duration was reduced from 20 min to 30 s to prevent shorting between the inner and outer ECC electrodes due to overgrowth. An SEM image of the resulting dendritic ECC is shown in Figure 4.9.1b. Dendritic structures grew on the protruding inner core as well as on the outer chrome electrode; growth on the outer

electrode is most likely due to improper grounding of the chrome. However, high resistance measurements (GΩ regime) between the inner and outer electrode indicated that there was no shorting and so the dendritic ECC was used for electrochemical measurements.

To examine the potential of the dendritic ECC architecture for electrochemical sensing, DPVs were performed to detect the oxidation of 1 mM FCA (Fig. 4.9.2). Multiple DPV measurements exhibited similar current signals, with an average peak current of approximately -16 μA; peak current was determined by subtracting the current at 0.1 V from the current at ~2.8 V where the peak appeared. Current densities (*J*) were calculated for the dendritic ECC, the ECC, and the first generation nanocoax to compare electrochemical performance of the three nanoarchitectures (Fig. 4.9.3); a planar Au control was compared as well. Current densities were determined by dividing peak current by array base area. The dendritic ECC array exhibited a current density of 320 $\mu A/mm^2$, whereas the ECC array alone had a current density of 150 $\mu A/mm^2$ and the nanocoaxial array exhibited a current density of 83 $\mu A/mm^2$. Planar Au sensors produced a current density of 5 $\mu A/mm^2$. In this initial study, the dendritic ECC array doubled the current density over the standard ECC array, on an array base area 4x smaller.

The increased current density of the dendritic ECC array could allow for improved sensitivity in the electrochemical detection of biomarkers over the standard ECC array alone. However, more studies must be conducted to corroborate these initial studies.

DENA growth times for fabricating dendritic ECCs need to be examined as well as fabricating structures with properly grounded outer chrome electrodes. Once an optimized and reproducible dendritic ECC structure has been obtained, further studies (ALP dose titrations, ELISAs) with the dendritic ECC arrays will be completed to determine if the increased current density corresponds to improved sensitivity.

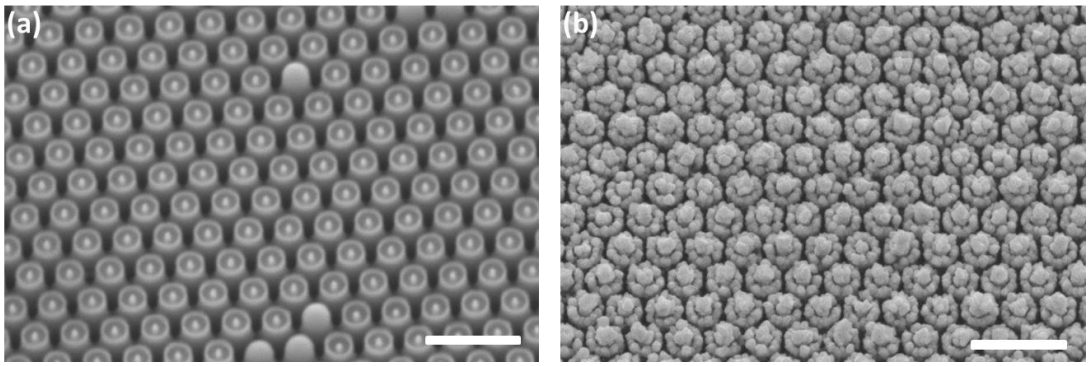

Figure 4.9.1. SEM images of an ECC array (a) before dendritic growth and (b) after DENA has been performed (b). ECCs are composed of an inner Au working electrode and an outer Cr counter electrode. Scale bar represents 2 μm. SEMs taken at 30° tilt.

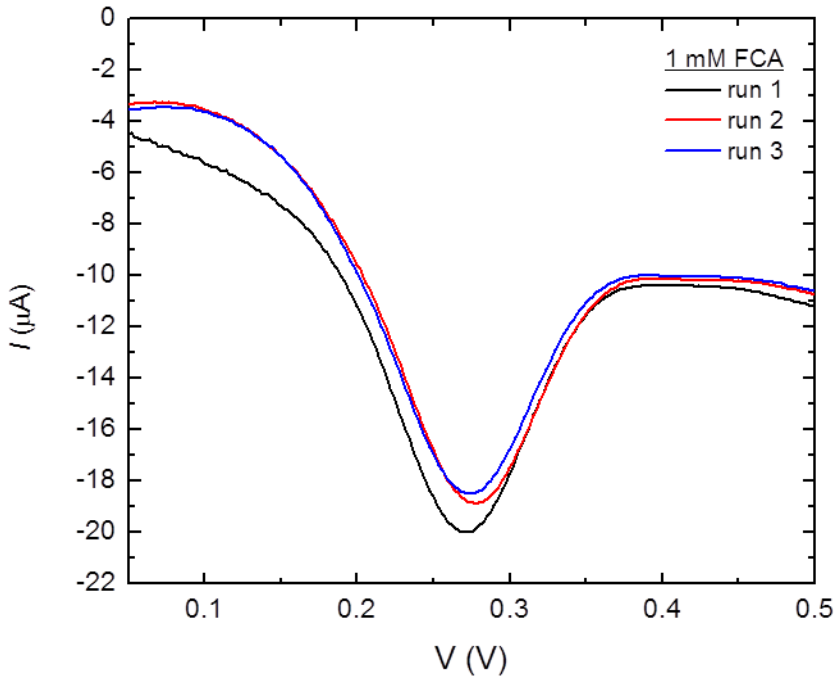

Figure 4.9.2. DPV signals of 1 mM FCA on a dendritic ECC array. DPVs were measured on the same device. X-axis: potential (*V*); y-axis: current (*I*).

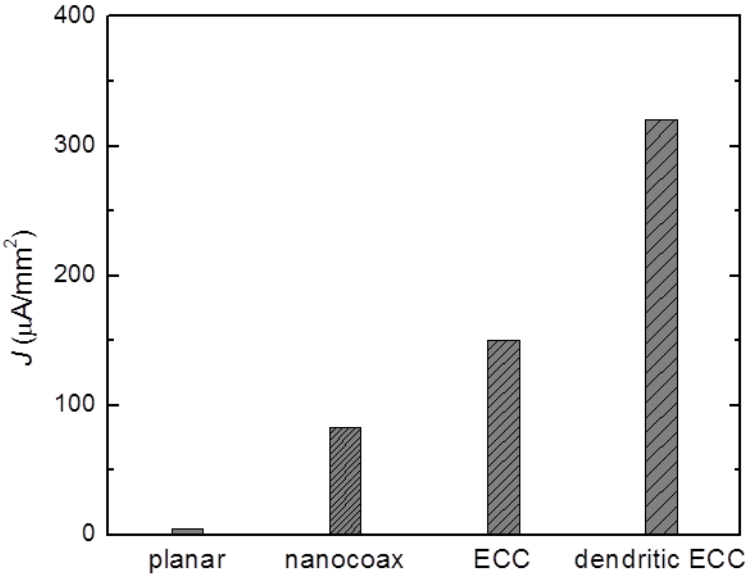

Figure 4.9.3. Current densities (*J*) of planar Au, nanocoax, ECC, and dendritic ECC arrays during the oxidation of 1 mM FCA. Current densities were determined by dividing DPV peak current by each array base area.

Summary

Utilizing directed electrochemical nanowire assembly (DENA), dendritic-based electrochemical arrays have been fabricated and developed on several base substrates. Gold dendrites were fabricated on planar Au and Au pillar arrays to create planar and 3D dendritic structures. These dendritic sensors were tested in their ability to detect CT in an electrochemical ELISA. While planar dendrites exhibited the highest current signal, 3D dendrites demonstrated greater range of detection and lower limits of detection. 3D dendrites were subsequently chosen for further studies into dendritic-based electrochemical sensors. Following 3D dendritic sensors, however, produced dissimilar results due to varying dendritic growth between samples. Therefore, DENA parameters were examined and optimized to allow for reproducible dendritic growth.

3D dendrites were fabricated on photolitographically-patterned chips containing eight individually-addressed arrays. CT ELISAs were then performed on these 3D dendritic sensors, which improved detection over its Au pillar array counterpart by an order of magnitude. Additionally, the 3D dendritic array matched the performance of the standard optical ELISA with regard to dynamic range of detection and limit of detection. Furthermore, these dendritic-based arrays offer advantages over the conventional ELISA. The electrochemical readout of the dendritic array does not require the complex instrumentation or high amount of reagent needed in the optical readout. Dendritic arrays are also easily amenable to multiplexing for the simultaneous detection of disease biomarkers, a highly desired POC option not easily acquired in optical setups. Finally, in the future, the benefit of the close proximity of the nanocoaxial WE–CE distance could

be combined with the dendritic advantage of increased surface area by utilizing DENA on the inner core of the ECC. These future studies hold a promising path to a highly sensitive and robust POC device for infectious disease detection.

References

1. Paneru, G. & Flanders, B. N. Complete reconfiguration of dendritic gold. *Nanoscale* **6,** 833–41 (2014).

2. Sanles-Sobrido, M. Highly catalytic single-crystal dendritic Pt nanostructures supported on carbon nanotubes. *Chem. Mater.* **21,** 1531–1535 (2009).

3. Rashid, M. & Mandal, T. Synthesis and catalytic application of nanostructured silver dendrites. *J. Phys. Chem. C* **111,** 16750–16760 (2007).

4. Hermanson, K., Lumsdon, S. & Williams, J. Dielectrophoretic assembly of electrically functional microwires from nanoparticle suspensions. *Science* **294,** 1082–1086 (2001).

5. Wen, X., Xie, Y., Mak, W. & Cheung, K. Dendritic nanostructures of silver: facile synthesis, structural characterizations, and sensing applications. *Langmuir* **22,** 4836–4842 (2006).

6. Bhimji, A., Zaragoza, A., Live, L. S. & Kelley, S. O. Electrochemical enzyme-linked immunosorbent assay featuring proximal reagent generation: detection of human immunodeficiency virus antibodies in clinical samples. *Anal. Chem.* **85,** 6813–9 (2013).

7. Soleymani, L. *et al.* Hierarchical nanotextured microelectrodes overcome the molecular transport barrier to achieve rapid, direct bacterial detection. *ACS Nano* **5,** 3360–6 (2011).

8. Teng, X. & Yang, H. Synthesis of platinum multipods: an induced anisotropic growth. *Nano Lett.* **5,** 2–8 (2005).

9. Kawasaki, J. & Arnold, C. Synthesis of platinum dendrites and nanowires via directed electrochemical nanowire assembly. *Nano Lett.* **11,** 781–785 (2011).

10. Ozturk, B., Flanders, B. N., Grischkowsky, D. R. & Mishima, T. D. Single-step growth and low resistance interconnecting of gold nanowires. *Nanotechnology* **18,** 175707 (2007).

11. Ozturk, B., Talukdar, I. & Flanders, B. N. Directed growth of diameter-tunable nanowires. *Nanotechnology* **18,** 365302 (2007).

12. Cheng, C., Gonela, R., Gu, Q. & Haynie, D. Self-assembly of metallic nanowires from aqueous solution. *Nano Lett.* **5,** 175–178 (2005).

13. Nerowski, A., Poetschke, M. & Bobeth, M. Dielectrophoretic growth of platinum nanowires: Concentration and temperature dependence of the growth velocity. *Langmuir* **28,** 7498–7504 (2012).

14. Schmädicke, C. *et al.* Copper nanowire synthesis by directed electrochemical nanowire assembly. *RSC Adv.* **4,** 46363–46368 (2014).

15. Talukdar, I., Ozturk, B., Flanders, B. N. & Mishima, T. D. Directed growth of single-crystal indium wires. *Appl. Phys. Lett.* **88,** 221907 (2006).

16. Sage, A. T., Besant, J. D., Lam, B., Sargent, E. H. & Kelley, S. O. Ultrasensitive electrochemical biomolecular detection using nanostructured microelectrodes. *Acc. Chem. Res.* **47,** 2417–2425 (2014).

17. Das, J. & Kelley, S. O. Protein detection using arrayed microsensor chips: tuning sensor footprint to achieve ultrasensitive readout of CA-125 in serum and whole blood. *Anal. Chem.* **83,** 1167–72 (2011).

18. Fang, Z. *et al.* Direct profiling of cancer biomarkers in tumor tissue using a multiplexed nanostructured microelectrode integrated circuit. *ACS Nano* **3,** 3207–3213 (2009).

19. Ricci, F., Adornetto, G. & Palleschi, G. A review of experimental aspects of electrochemical immunosensors. *Electrochim. Acta* **84,** 74–83 (2012).

Chapter 5.

Discussion and concluding remarks

The standard optical enzyme-linked immunosorbent assay (ELISA) is limited in point-of-care (POC) applications due to complex instrumentation, high reagent consumption, cost, and lack of facile multiplexing capabilities. The electrochemical readout of an ELISA with nanocoaxial arrays and dendritic arrays developed in this thesis was shown to match the standard optical ELISA with regards to cholera toxin (CT) detection range and limit of detection (LOD), while overcoming a handful of these limitations. These nanoarchitectures allow for a simple electrical readout while requiring orders of magnitude less reagent. In addition, these architectures allow for facile multiplexing due to the ability to fabricate multiple electrically-independent arrays on a single chip. Therefore, these nanostructures offer advantages over the conventional ELISA that make them attractive candidates for further development towards POC applications.

Nanocoax

In these studies, we utilized the nanocoax as a nanogap sensor in order to take advantage of the nanoscale proximity of the working electrode (WE) and counter electrode (CE) to enhance electrochemical sensitivity. Recently, increased efforts have been made towards the fabrication of nanogap biosensors to allow for large-scale production, easy read-out and high sensitivity[1]. A sensor with a nanometer-scale electrode gap can bring target biomolecules spatially closer to these sensing electrodes, enhancing detection and sensitivity[2]. The biomolecules can be detected through electrical behaviors such as resistance/impedance, capacitance/dielectric response, or field-effect[3], allowing for many label-free detection schemes based on a change in electrical signal upon biomolecule presence or binding.

The majority of nanogap biosensor research has been focused on the detection of DNA oligonucleotides[1,4–7]. Nanogap sensors can be conjugated with a probe oligonucleotide sequence that is complimentary to the target DNA strand. Upon hybridization of the target sequence, a change in the electrical signal is induced. Zaffino et al.[8] demonstrated label-free detection of single point mutations via DNA hybridization with a conductance-based nanogap sensor. Hybridization of complimentary DNA strands resulted in an increase in current; however DNA strands with a single base pair mismatch were discriminated, resulting in high specificity. Several studies have recently applied this concept to the detection of target protein biomarkers[9,10]. For example, Gu et al.[11] utilized a nanogap field-effect transistor for the electrical detection of the anti-avian influenza antibody. Despite high sensitivity achieved with such sensors, only a small number are being further developed towards POC applications due to the high cost and low yield associated with current fabrication methods[12].

The structure of current nanogap biosensors consists of 2D planar and 3D nonplanar architectures, oftentimes in the form of a field-effect transistor. Many planar nanogap biosensors are composed of nanowires arranged horizontally on substrates. 3D nanogap sensors are mainly composed of electrodes parallel to each other (either horizontally or vertically), increasing the electrode area within the nanoscale proximity over the planar nanogap sensors. Our nanocoax is a 3D nanogap structure that provides an additional advantage over most conventional 3D nanogap biosensors. In the coaxial structure for electrochemical detection, the inner WE is circumferentially surrounded by the outer CE, as opposed to other 3D nanogap structures that consist primarily of two parallel

electrodes. This concentric outer CE allows for the radial diffusion of molecules from all sides whereas most 3D nanogap sensors are limited by linear diffusion in a single direction. As a result, the nanocoax allows for increased redox cycling over the conventional parallel electrode setup, and thus an increase in signal.

Furthermore, fabrication of the nanocoax utilizes techniques that are economical and reproducible. The use of nanoimprint lithography provides a reusable, low-cost "master" tool to produce well-ordered templates for nanocoaxial arrays. Additionally, the vast majority of the fabrication costs are associated with labor; the actual cost of materials is negligible in comparison. This fabrication technique also has the ability to allow for high scalability, which would enable the desired low-cost, high-yield characteristic needed for POC device development. While we did encounter electrical conductivity issues (too low resistance, and even shorting) with some batches, the nanocoaxes that displayed high resistance (i.e. $R \geq 1$ GΩ) and that were used for the electrochemical detection of CT exhibited comparable ranges of detection. This would indicate that properly fabricated nanocoaxes are reproducible as electrochemical biosensors, however quality control checks and fabrication protocols between batches need to be standardized to improve yield.

The next generation coax currently under development, the extended core coax (ECC), continues to utilize these fabrication techniques and provides a coaxial architecture more amenable to POC applications. The extended inner core could be functionalized with an ELISA antibody against a target infectious disease biomarker in order to move away

from the plate-base format to a lab-on-chip assay. Furthermore, elimination of the coaxial WE-CE annulus in the ECC could minimize diffusion issues encountered in the first generation coaxes, and would allow for a flow-across device while still maintaining the advantageous nanoscale WE-CE proximity. With this ECC platform, multiplexing the electrically-independent nanocoaxial arrays on a single chip would still be feasible, allowing for the simultaneous detection of multiple infectious disease biomarkers. Previously, array areas as small as 150 μm^2 have been fabricated, containing only ~100 nanocoaxes and requiring only ~10 fl sample volume. Such a chip could be biofuncitonalized with capture antibody and coupled with microfluidics to produce a portable, pre-packaged POC device.

Dendrites

In biosensors lacking the nanoscale WE-CE proximity, an attractive approach to enhancing the sensitivity is to increase the number of biomolecular events at the electrode surface by increasing the 3D surface area. The large footprint of 3D nanostructured electrodes facilitates high levels of collisions with target analytes and promotes higher rates of diffusion[13]. Additionally, the increased surface area enhances the amount of probe molecules on the electrode for target capture. Directed electrochemical nanowire assembly (DENA) is an emerging electrodeposition method that produces highly-textured, 3D nanostructured electrodes[14], and has been recently studied in the fabrication of various metallic dendritic structures[15–19]. Due to the novelty of the technique, most studies to date have focused on the fabrication parameters and morphology of the resulting dendrites. However, one group in particular, the Kelley group at the University

of Toronto, has significantly contributed to the development of dendritic devices towards POC applications.

The Kelley group has fabricated numerous nanostructured microelectrodes (NMEs) for the detection of several disease biomarkers[20]. Those NMEs were formed from the electrodeposition of metal through constricted apertures onto planar gold electrodes[13]. These apertures are within the micron regime, and allow for 3D dendritic structures to grow upward off of the planar electrode. The arrays were functionalized with probe molecules and used in the detection of various target analytes, including nucleic acids[21,22], circulating tumor cells[23], and proteins[24,25]. NMEs have demonstrated sensitive and rapid detection of aM concentrations of nucleic acids[26,27] and pM concentrations of protein biomarkers[28]. While many of these sensors have been used in the detection of cancer biomarkers, the Kelley group has recently utilized these arrays in the detection of infectious diseases such as HIV[28] and rubella[29]. Both arrays were comparable to the standard ELISA in the detection of these infectious disease biomarkers. Additionally, they incorporated NMEs for detection of rubella virus with a digital microfluidic device, allowing for an automated, multiplexed on-chip analysis requiring less than 2 μl of sample. These NMEs have exhibited much potential for further development to POC diagnostic devices; currently, the Kelley group is exploring several low-cost substrate alternatives to silicon for NMEs, while maintaining reproducibility and high electrochemical sensing performance[30].

We have focused on utilizing 3D pillar arrays as our base substrate for dendritic growth, as opposed to the planar substrate used by the Kelley group. Dendritic growth on pillar arrays promotes growth from the pillar tips in a radially upward direction. We would expect to achieve greater surface areas in this manner, whereas planar growth would be limited in the vertical direction. While a direct comparison cannot be made to the performance of NMEs due to different biomarkers tested, both NMEs and our dendritic arrays are comparable in performance to the standard ELISA for the respective biomarkers investigated with regard to detection range and LOD. Additionally, the dendritic arrays achieved this level of detection without any biofunctionalization; it is expected that conjugation of capture antibody to the dendritic surface would enhance sensitivity by eliminating any diffusion limitations.

We have concentrated on 3D pillar arrays as opposed to planar electrodes as our base substrate for two reasons. First, the 3D dendritic arrays outperformed the planar dendritic-based sensors in the detection of a CT ELISA. Second, 3D pillar arrays form the base of the ECC arrays. Therefore, combining the ECC with 3D dendritic growth could be doubly advantageous, and overcome the main limitations of each concept. The ECC enables beneficial nanoscale WE-CE proximity, which is lacking in dendritic sensors whose WE-CE distance is macroscopic. 3D dendritic structures grown on the inner Au core of the ECC would provide an extremely high surface area extending outside of the WE-CE annulus, enhancing the limited electrode surface area in standard ECCs. The combination of these two architectures could allow for increased sensitivity

and detection through coupling redox cycling capabilities with a high surface-area-to-volume working electrode.

The DENA process in the macro-scale setup is well-suited for further development towards POC applications. This set-up allows for high scalability as multiple arrays can be simultaneously fabricated within minutes; fabricating all arrays on a single chip will allow for increased uniformity of dendritic growth, which will allow for reproducible electrochemical sensing applications. Additionally, the one-step fashion of the DENA method allows for timely and cost-effective fabrication of arrays, without the need for significant training.

To be amenable towards POC applications, future dendritic work will need to focus on optimizing and fabricating reproducible dendritic arrays on a single chip. This will allow for biofunctionalization of capture antibody onto the arrays for an on-chip electrochemical ELISA, as well as providing a detection platform with multiplexing capabilities. Currently, the photolithographically patterned chips contain only 8 arrays on a 16x30 mm^2 device. However, in nanocoaxial studies, arrays as small as 150 μm^2 have been routinely fabricated. This array dimension can be applied to the dendritic photolithographic chips to incorporate a significantly greater number of individually-addressed arrays. These smaller arrays would require much less sample and provide a greater number of arrays to multiplex for the detection of numerous biomarkers. Once arrays are reproducibly fabricated and functionalized, microfluidics would need to be incorporated to produce a pre-packaged, portable POC diagnostic device.

Lab-on-chip devices

To be fully realized as a POC device, the detection assay must move away from the plate-based format to a "lab-on-chip" approach in which capture antibody is immobilized directly onto the electrode surface. Integration of biomarker capture and electrochemical detection on the arrays will allow for a portable and pre-packaged device for POC applications. While biofunctionalization is not a feasible option for the first generation nanocoaxial devices due to diffusion issues and inhibited liquid exchange, the extended core of the ECC array provides a promising platform that could overcome these limitations. Photolithographically-patterned dendritic arrays constitute an amenable platform for antibody functionalization, however studies must first be conducted to obtain structurally identical and reproducible dendritic growth on all arrays within the chip.

After further development of the dendritic and nanocoaxial structures, biofunctionalization of antibodies can be incorporated onto these plates, allowing for an on-chip assay towards POC detection. We have established several protocols for the reproducible conjugation of ELISA antibody onto electrode surfaces using well-studied Au-thiol linkage chemistry. We have demonstrated the use of thiolated protein-G to attach antibodies to Au electrode surfaces (e.g. planar, pillar arrays) without insulating the electrode surface, allowing for the nanosensor to transduce electrochemical signal despite the protein layer on the conducting electrode. Additionally, using protein-G conjugation allows the ELISA to be adjusted for any target protein biomarker, as any IgG antibody will bind to protein-G; this is advantageous in producing multiplexed on-chip ELISAs to screen for multiple disease biomarkers. While our ELISA still relies on an

enzymatic label for biomarker detection, a label-free reporter antibody could be developed using quantum dots or gold nanoparticles loaded with a redox reporter molecule.

Biofunctionalization arrays must be coupled with some type of microfluidic device in order to produce a stable and portable POC device that contains required buffer and reagent. Microfluidic packaging allows for portability but also ease of use for untrained personnel in resource limited areas. Microfluidic paper-based analytical devices (μPADs) are a newer class of microfluidics that is being designed specifically with developing countries in mind. μPADs combine the capabilities of conventional microfluidics while maintaining the simplicity of diagnostic test strips[31]; they require no external supporting equipment and are controlled largely by capillary motion, making them inexpensive and easy to use. One well-known application of μPADs is their use for glucose monitoring in diabetic patients[32].

Nanocoaxial and dendritic arrays could be incorporated into μPADs for POC devices. Papers containing conducting carbon or metal fibers are electrically conducting and could be used to create an electrochemical μPAD composed of dendritic or nanocoaxial structures. Electrochemical μPADs have been successfully demonstrated by Dunchai et al.[33] for the detection of glucose, lactate, and uric acid, providing proof-of-concept for such devices. Electrochemical nanostructured μPADs could allow for sensitive and quantitative readout of target biomarkers when used in conjunction with a held-hand potentiostat and a smartphone or tablet. Hand-held potentiostats would allow for a

portable method to quantitate electrochemical reactions on the μPAD, and could transduce this information via USB to visualizing software installed on a smartphone/tablet. An example of a potential POC device is shown below in Figure 5.1.

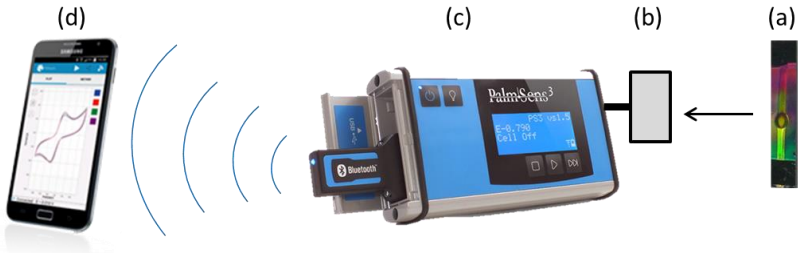

Figure 5.1. POC nanodevice. (a) Test strip based on nanocoax or dendritic architecture (not to scale). (b) Adaptor box in which to insert test strip for readout on the (c) hand-held potentiostat. (d) Hand held potentiostats have bluetooth and USB ports for direct readout on a smart phone, tablet, or computer.

Future scope

To test the true POC capabilities of such a device, it would need to undergo shelf-life stability testing and field testing. Studies would be conducted on the stability of the reagents in the chip and its performance after weeks to months of shelf-life. Additionally, devices would be placed in extreme temperatures, especially heat, over a certain amount of time to mimic the environment of many resource-limited areas in need of POC diagnostics. Specificity and sensitivity profiles of the device would need to be obtained from blind sample testing in order to assess the percentage of false positives and false negatives.

Potential pitfalls in such a device include biofouling and reagent stability. Biofouling is a common issue with electrochemical devices, as the high level of proteins in serum and heterogeneous samples are prone to non-specifically stick to metal electrodes. However, blocking protocols and/or pre-dilution of the sample are robust methods to overcome biofouling. Pre-dilution can even be incorporated into the microfluidic design, automating the process on-chip. Issues with reagent stability in harsh conditions may be encountered. One efficient technique to avoid reagent degradation is to store the reagents in a lyophilized state on the device. Both issues are well-documented and these solutions have been used successfully to circumvent these problems.

With further development and incorporation into a lab-on-chip microfluidic system, our nanoarchitectures could facilitate much-needed quantitative analysis of disease biomarkers in resource-limited areas as opposed to currently available "yes/no" type options. Quantitative analysis would allow for proper monitoring of disease, preventing epidemic outbreaks and providing better care for the patient. Additionally, these multiplexed devices could test for multiple diseases simultaneously. This is extremely beneficial since many diseases exhibit similar symptoms; therefore, a panel of biomarkers could be screened from one sample, providing better patient diagnosis and thus prognosis. Finally, and possibly most importantly, the fabrication techniques used would allow for an economical and cost-effective device, a must-have characteristic in POC diagnostics.

References

1. Chen, X. *et al.* Electrical nanogap devices for biosensing. *Mater. Today* **13,** 28–41 (2010).

2. Li, T., Hu, W. & Zhu, D. Nanogap electrodes. *Adv. Mater.* **22,** 286–300 (2010).

3. Perumal, V. & Hashim, U. Advances in biosensors: Principle, architecture and applications. *J. Appl. Biomed.* **12,** 1–15 (2014).

4. Porath, D., Bezryadin, A., Vries, S. De & Dekker, C. Direct measurement of electrical transport through DNA molecules. *Nature* **403,** 635–638 (2000).

5. Iqbal, S. M., Balasundaram, G., Ghosh, S., Bergstrom, D. E. & Bashir, R. Direct current electrical characterization of ds-DNA in nanogap junctions. *Appl. Phys. Lett.* **86,** 153901 (2005).

6. Hashioka, S., Saito, M., Tamiya, E. & Matsumura, H. Deoxyribonucleic acid sensing device with 40-nm-gap-electrodes fabricated by low-cost conventional techniques. *Appl. Phys. Lett.* **85,** 687 (2004).

7. Fan, Y. *et al.* Detection of microRNAs using target-guided formation of conducting polymer nanowires in nanogaps. *J. Am. Chem. Soc.* 5437–5443 (2007).

8. Zaffino, R. L., Mir, M. & Samitier, J. Label-free detection of DNA hybridization and single point mutations in a nano-gap biosensor. *Nanotechnology* **25,** 105501 (2014).

9. Singh, K. *et al.* Nanoparticle-enhanced sensitivity of a nanogap-interdigitated electrode array impedimetric biosensor. *Langmuir* 13931–13939 (2011).

10. Marcon, L., Melnyk, O. & Stiévenard, D. Current based antibodies detection from human serum enhanced by secondary antibodies labelled with gold nanoparticles immobilized in a nanogap. *Biosens. Bioelectron.* **23,** 1185–8 (2008).

11. Gu, B. *et al.* Nanogap field-effect transistor biosensors for electrical detection of avian influenza. *Small* **5,** 2407–12 (2009).

12. Balakrishnan, S. R. *et al.* A point-of-care immunosensor for human chorionic gonadotropin in clinical urine samples using a cuneated polysilicon nanogap lab-on-chip. *PLoS One* **10,** e0137891 (2015).

13. Zhou, Y., Wan, Y., Sage, A., Poudineh, M. & Kelley, S. Effect of microelectrode structure on electrocatalysis at nucleic acid-modified sensors. *Langmuir* **30,** 14322–14328 (2014).

14. Kawasaki, J. & Arnold, C. Synthesis of platinum dendrites and nanowires via directed electrochemical nanowire assembly. *Nano Lett.* **11,** 781–785 (2011).

15. Paneru, G. & Flanders, B. N. Complete reconfiguration of dendritic gold. *Nanoscale* **6,** 833–41 (2014).

16. Wen, X., Xie, Y., Mak, W. & Cheung, K. Dendritic nanostructures of silver: facile synthesis, structural characterizations, and sensing applications. *Langmuir* **22,** 4836–4842 (2006).

17. Nerowski, A., Poetschke, M. & Bobeth, M. Dielectrophoretic growth of platinum nanowires: Concentration and temperature dependence of the growth velocity. *Langmuir* **28,** 7498–7504 (2012).

18. Schmädicke, C. *et al.* Copper nanowire synthesis by directed electrochemical nanowire assembly. *RSC Adv.* **4,** 46363–46368 (2014).

19. Talukdar, I., Ozturk, B., Flanders, B. N. & Mishima, T. D. Directed growth of single-crystal indium wires. *Appl. Phys. Lett.* **88,** 221907 (2006).

20. Sage, A. T., Besant, J. D., Lam, B., Sargent, E. H. & Kelley, S. O. Ultrasensitive electrochemical biomolecular detection using nanostructured microelectrodes. *Acc. Chem. Res.* **47,** 2417–2425 (2014).

21. Das, J. *et al.* An ultrasensitive universal detector based on neutralizer displacement. *Nat. Chem.* **4,** 642–648 (2012).

22. Soleymani, L. *et al.* Hierarchical nanotextured microelectrodes overcome the molecular transport barrier to achieve rapid, direct bacterial detection. *ACS Nano* **5,** 3360–6 (2011).

23. Mohamadi, R. M. *et al.* Sample-to-answer isolation and mRNA profiling of circulating tumor cells. *Anal. Chem.* **87,** 6258–64 (2015).

24. Das, J. & Kelley, S. Protein detection using arrayed microsensor chips: tuning sensor footprint to achieve ultrasensitive readout of CA-125 in serum and whole blood. *Anal. Chem.* **83,** 1167–1172 (2011).

25. Fang, Z. *et al.* Direct profiling of cancer biomarkers in tumor tissue using a multiplexed nanostructured microelectrode integrated circuit. *ACS Nano* **3,** 3207–3213 (2009).

26. Soleymani, L., Fang, Z., Sargent, E. H. & Kelley, S. O. Programming the detection limits of biosensors through controlled nanostructuring. *Nat. Nanotechnol.* **4,** 844–8 (2009).

27. Soleymani, L. *et al.* Nanostructuring of patterned microelectrodes to enhance the sensitivity of electrochemical nucleic acids detection. *Angew. Chemie* **48,** 8457–60 (2009).

28. Bhimji, A., Zaragoza, A., Live, L. & Kelley, S. Electrochemical enzyme-linked immunosorbent assay featuring proximal reagent generation: detection of human immunodeficiency virus antibodies in clinical. *Anal. Chem.* **84,** 6813–6819 (2013).

29. Rackus, D. *et al.* A digital microfluidic device with integrated nanostructured microelectrodes for electrochemical immunoassays. *Lab Chip* **15,** 3776–3784 (2015).

30. Lam, B. *et al.* Optimized templates for bottom-up growth of high-performance integrated biomolecular detectors. *Lab Chip* **13,** 2569–75 (2013).

31. Martinez, A., Phillips, S. & Whitesides, G. M. Diagnostics for the developing world: microfluidic paper-based analytical devices. *Anal. Chem.* **82,** 3–10 (2009).

32. Nie, Z., Deiss, F., Liu, X., Akbulut, O. & Whitesides, G. M. Integration of paper-based microfluidic devices with commercial electrochemical readers. *Lab Chip* **10,** 3163–9 (2010).

33. Dungchai, W., Chailapakul, O. & Henry, C. Electrochemical detection for paper-based microfluidics. *Anal. Chem.* **81,** 5821–5826 (2009).

Appendix I

Molecular Imprinting

Introduction

Molecular imprinting is a technique that creates tailor-made binding sites to a specific antigen or molecule based on memory of size, shape, and functional group charge of that template molecule[1]. Imprints are formed when the template molecule of choice is mixed with a functional monomer and an excess of cross-linking agent; this solution polymerizes and coats the electrode surface in the presence of current. The template molecule can then be extracted, leaving behind specific recognition sites complementary in shape, size, and chemical functionality (e.g. hydrogen bonds, dipole-dipole, ionic interactions) to the template.

Often known as "artificial antibodies", molecular imprints possess high affinity and selectivity for their target template. Compared to biological probes such as antibodies and nucleic acids, imprints exhibit a higher physical robustness and resistance towards elevated temperatures[2]. Additionally, they are less expensive to synthesize and can be maintained at room temperature for years while maintaining their recognition capacities. While all of these factors place molecular imprint technology at a high advantage over conventional antibody detection in biosensing, one major obstacle remains in the way. Molecular imprinting has been most successful in the detection of small molecules and in mostly non-aqueous media. The application of molecular imprinting towards large molecule, protein detection in aqueous-based solutions has remained somewhat of a challenge; proteins possess high surface complexity, conformational flexibility, and large sizes not encountered in polymer materials typically used in imprinting[3].

We have developed molecular imprint (MIP) devices for the detection of ferritin and human papillomavirus derived E7 protein on carbon-nanotube tips coated in phenol polymer[4]. Using the same polymer and imprinting technique, we are moving toward a simpler platform of planar gold. Carbon nanotubes are expensive and timely to fabricate; planar gold electrodes would allow for a simple substrate on which to fabricate sensitive MIP devices that would provide high yield and lower cost. Previously, planar gold MIP devices were fabricated and characterized using streptavidin as the template protein[5]. Here, we examine preliminary studies on planar gold MIP devices using cholera toxin (CT) as the template protein.

Materials and Methods

Planar Au substrates were prepared with wells as previously described. Electropolymerization was performed on a Reference 600 potentiostat or on a Reference 1000 potentiostat (Gamry Instruments, Warminster, PA) using a three-electrode system. An external Ag/AgCl wire served as the reference electrode and an external Pt wire served as the counter electrode. The Au substrate to be electropolymerized functioned as the working electrode. Immediately before electropolymerization, substrates were cleaned with UV/ozone for 20 min.

Molecular imprinted polymers (MIPs) were formed via electropolymerization of phenol onto Au substrates via cyclic voltammetry (CV). Solution containing 100 μg/ml of template protein and 2.5 mM phenol in PBS, pH 7.4, were pipetted onto the substrate. Using single frequency electrochemical impedance spectroscopy (SEIS), a 300 mV DC voltage was applied for 30 s to attract the template protein to the Au surface. CV was

then immediately carried out to electropolymerize the protein/polyphenol film. CVs were performed with a scan rate of 50 mV/s and a step size of 2 mV for 5 cycles, sweeping between 0 V to 0.9 V. Electropolymerization was confirmed by square wave voltammetry (SWV) measurements with 1 mM FCA in PBS, pH 7.4 with the potential range of 0 V to 0.5 V, a pulse size of 50 mV, and a frequency of 10 Hz.

To remove the template protein and form the resulting MIP, the substrate was incubated with 100 μg/ml proteinase K in 1% SDS/0.1% AcOH overnight at room temperature and then rinsed 3 times with PBS, pH 7.4. Non-imprinted polymers (NIPs) were formed in the exact same manner, except no template protein was incorporated into the phenol solution during electropolymerization.

Re-binding of template protein was performed in PBS, 7.4 with an incubation time of 20 min. The solution was gently pipetted out and no rinses were performed. SWV was performed to analyze binding using 1 mM FCA, PBS 7.4 with the same parameters as described above.

Results

Previously, differential pulse voltammetry (DPV) was the method used for electrochemical measurement in MIP studies. In the following studies, square wave voltammetry (SWV) was the chosen method over DPV. This was due to the presence of a flatter baseline during measurements with SWV over DPV, resulting in more defined, sharper peak currents (Figure A.1). In Figure A.1.a., DPV was used to measure 1 mM FCA in PBS, pH 7.4 on a planar gold MIP device after extraction of template protein (in this case, streptavidin). Here, the baseline current drifts in a significant upward sloping

fashion, making it harder to elucidate the true peak current. The baseline begins ar approximately 1 μA and rises to about 5 μA over the measurement period. In Figure A.1.b., SWV was used to measure 1 mM FCA on a planar gold MIP after streptavidin extraction as well. With the SWV method, the baseline remains noticeably flatter and demonstrates a much smaller upward slope, making the peak current much sharper and not hidden underneath the baseline as with the DPV method. Additionally, the baseline current with SWV increases by less than 1 μA over the entire measurement period. Therefore, SWV was used for the rest of the MIP studies as the method of electrochemical detection.

Preparation of the planar gold sample prior to electropolymerization was also examined. Two planar gold samples were either UV/ozone cleaned for 20 min, while two other planar gold samples were only cleaned with ethanol (did not undergo UV/ozone treatment). One sample from each cleaning group was electropolymerized with template molecule (CT) to form two MIP samples, whereas the other sample from each group was electropolymerized without CT to form the two NIP control samples. All four samples underwent extraction overnight (100 μg/ml proteinase K in 1% SDS/0.1% AcOH) and were rinsed in the morning with PBS. SWV signals of 1 mM FCA on all four resulting samples are shown Figure A.2. In Figure A.2.a, SWV signals are shown for the MIP (black) and NIP (red) samples whose planar gold substrate had undergone UV/ozone cleaning prior to electropolymerization. The NIP sample remains undamaged and intact on the planar gold, indicated by the significantly flat baseline in the SWV signal at the oxidation potential of FCA. The lack of peak current indicates that the electrically insulating polymer layer is in intact and preventing redox reaction at the gold surface.

Significant damage to NIP samples is typically designated by peak currents > 500 nA. The MIP sample demonstrates proper and good extraction of the template protein CT, indicated in the SWV by the well-defined, μA regime peak. The peak current, determined by subtracting the current to baseline at 0.05 V, was approximately 2 μA. Good MIP samples typically demonstrate peak currents of 1 – 3 μA.

The SWV signals for the MIP (black) and NIP (red) samples that did not undergo UV/ozone cleaning are shown in Figure A.2.b. Here, the NIP sample also remains undamaged and intact, indicated by the significantly flat baseline in the SWV signal at the oxidation potential of FCA. The MIP sample, on the other hand, demonstrated less extraction compared to the UV/ozone cleaned sample in Fig. A.2.a. The peak current in this MIP was approximately 0.5 μA, as determined by subtracting the current to baseline at 0.05 V. Therefore, all future planar gold samples were UV/ozone cleaned prior to electropolymerization.

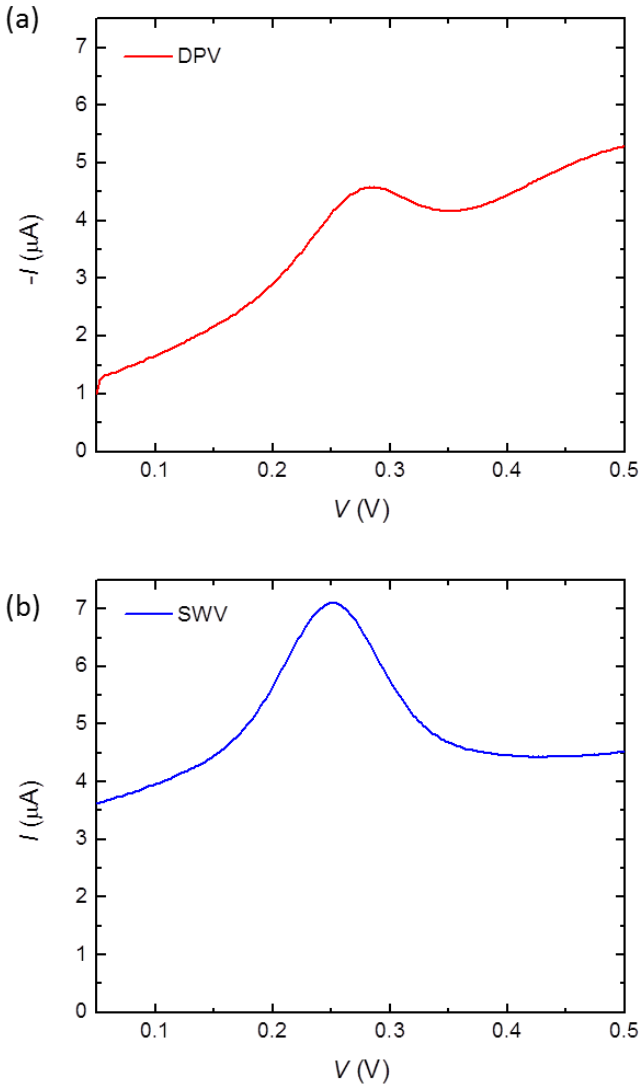

Figure A.1. Current response to the oxidation of 1 mM FCA on a molecularly imprinted polymer (MIP) after template protein (streptavidin) had been extracted. (a) DPV. (b) SWV. X-axis: potential (*V*); y-axis: current (*I*).

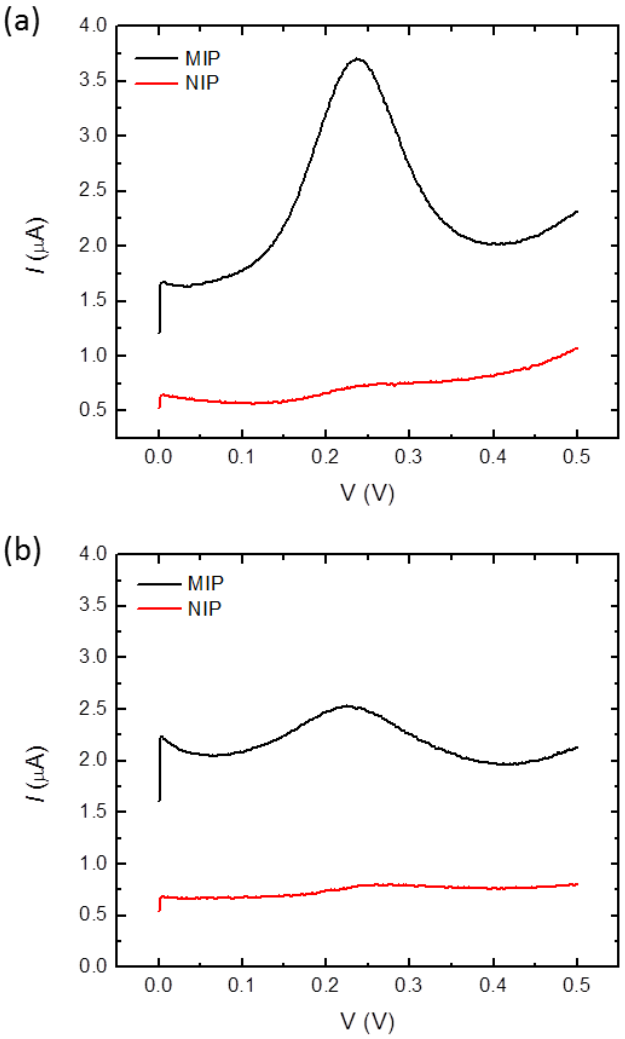

Figure A.2. SWVs of 1 mM FCA on samples with varying preparation technique. MIP samples were electrochemically examined with FCA after template protein streptavidin had been extracted (black). Control NIPs were electrochemically examined as well (shown in red) after exposure to identical extraction conditions. (a) SWVs of MIP and NIP samples that had undergone UV/ozone clean immediately prior to electropolymerization. (b) SWVs of MIP and NIP samples that did not undergo UV/ozone cleaning before electropolymerization.

Typical template protein concentrations in previous studies with ferritin and streptavidin had been 100 μg/ml. We examined this template concentration in CT MIPs, as well as 1 μg/ml due to the fact that the CT beta subunit used was smaller than the previous proteins examined. Two CT MIPs were fabricated using either 100 μg/ml CT or 1 μg/ml CT as the template concentration. A NIP control was also fabricated with no template protein. All three samples underwent extraction overnight, and then underwent rebinding with CT in PBS, pH 7.4. CT concentrations ranging from 1 fg/ml to 10 μg/ml were serially incubated on the samples for 20 min each and SWVs were performed with 1 mM FCA. The resulting SWV signals are shown in Figure A.3. All SWV signals were subtracted to the third data point to determine the peak current.

Range of detection for the two CT MIPs with varying template concentrations is shown in Figure A.4. Peak current (I_p) is plotted against the CT concentration (from rebinding) for the 1 μg/ml template CT MIP (black), 100 μg/ml template CT MIP (red), and the NIP control (blue). The 1 μg/ml template CT MIP does not exhibit a significant concentration-dependent response, indicated by the large error bars (determined by standard deviation). The 100 μg/ml template CT MIP demonstrated a concentration-dependent response, and exhibited tighter error bars overall. Therefore, the 100 μg/ml template concentration will be maintained for CT MIP studies.

Four CT MIP samples were fabricated on planar gold to examine CT rebinding as well as non-specific binding of other proteins of similar size (interleukin-2; IL2) and shape (shiga toxin; Stx). Each of the four CT MIPs were incubated with one of the above proteins over a serial range of 10^{-6} to 10^{3} ng/ml in PBS, pH 7.4 for 20 min at each concentration. After each 20 min incubation, SWVs were taken in 1 mM FCA. The peak currents (I_p)

determined from the SWVs are plotted in Figure A.5 against concentration of each protein. The two CT MIP samples (MIP-1, MIP-2) plotted in black underwent rebinding with CT. The two samples varied in their current magnitude; MIP-2 (dashed black) began with a higher starting peak current of about 4.2 μA whereas MIP-1 (solid black) began with a starting peak current of about 2 μA. This demonstrates variability in the extraction and/or polymerization process that needs to be assessed to fabricate reproducible devices. Both of these MIP samples, despite their different in current magnitudes, appear to demonstrate a concentration-dependent response; as CT concentration increases, current peak decreases. However, the two other MIPs with which IL2 (red) and Stx (blue) were incubated exhibit the same concentration-dependent response; they are even on the same current magnitude scale and slope grade as the CT rebinding on MIP-1 sample. The NIP control sample (magenta) does not exhibit the same current magnitude and has a lower background comparatively, but the same trend can be seen at the smaller current magnitude; the current is decreasing with the NIP sample as more CT is added. Therefore, this dose-dependent response is not specific to the imprint, but suggests non-specific binding of proteins to the polymer surface. However, the presence of imprints aggravates this effect as the imprints may provide more surface area for which the proteins can stick and cause more of an insulating change in the electrochemical response.

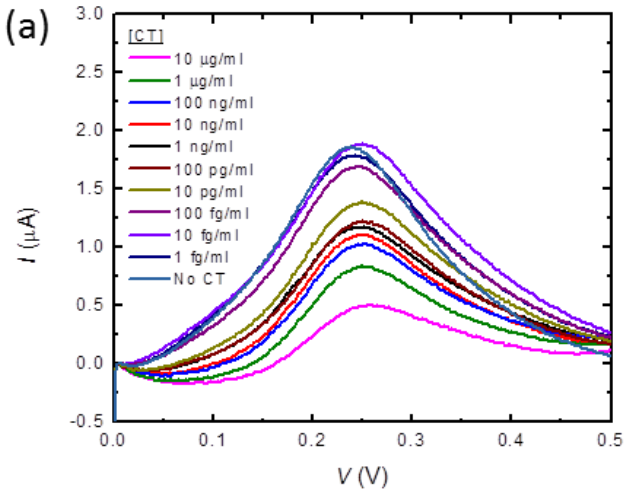
(a)
[CT]
10 µg/ml
1 µg/ml
100 ng/ml
10 ng/ml
1 ng/ml
100 pg/ml
10 pg/ml
100 fg/ml
10 fg/ml
1 fg/ml
No CT
I (µA)
V (V)

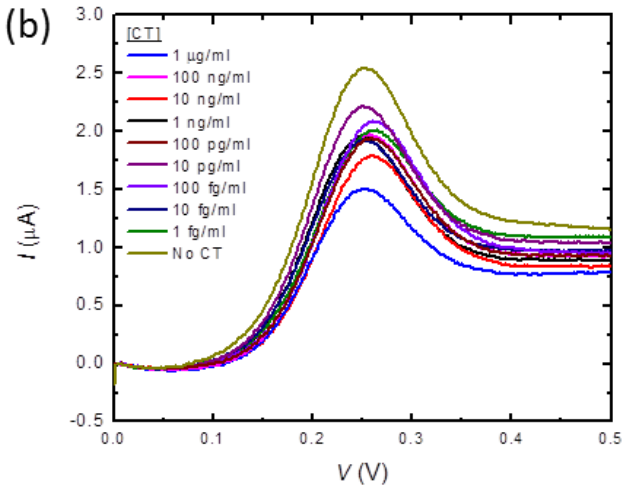
(b)
[CT]
1 µg/ml
100 ng/ml
10 ng/ml
1 ng/ml
100 pg/ml
10 pg/ml
100 fg/ml
10 fg/ml
1 fg/ml
No CT
I (µA)
V (V)

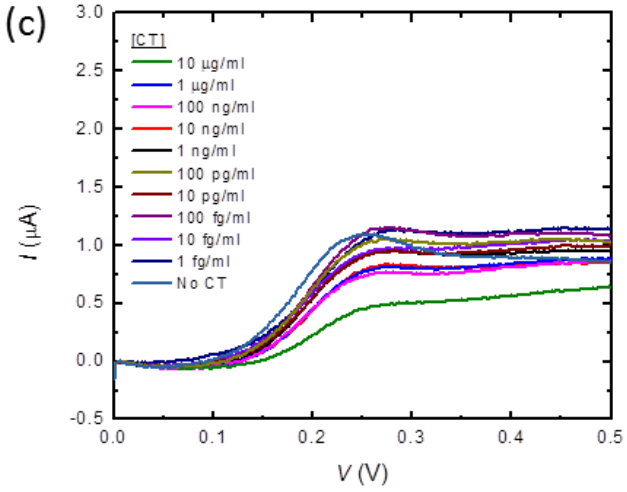
(c)
[CT]
10 µg/ml
1 µg/ml
100 ng/ml
10 ng/ml
1 ng/ml
100 pg/ml
10 pg/ml
100 fg/ml
10 fg/ml
1 fg/ml
No CT
I (µA)
V (V)

Figure A.3. SWVs of CT rebinding on MIPs of varying CT template concentration. SWVs of CT rebinding on MIPs of varying CT template concentration. (a) CT MIP produced using CT template concentration of 100 μg/ml. (b) CT MIP produced from 1 μg/ml CT template concentration. (c) NIP control; no CT template used, polymer only. All SWVs were subtracted to baseline at the third data point to determine peak currents. X-axis: potential (*V*); y-axis: current (*I*).

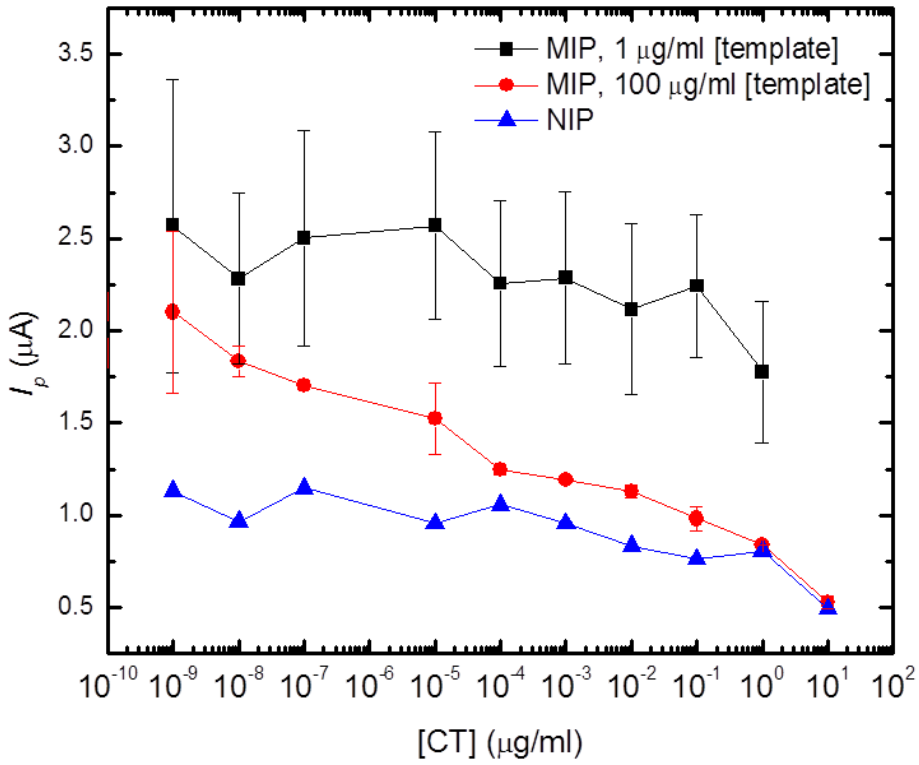

Figure A.4. Detection range of CT rebinding on MIPs of varying template concentration. On the y-axis, peak current (I_p) is plotted against CT concentration on the x-axis. Peak current was determined from the baselined SWV signals from Figure A.3. Rebinding of CT on a CT MIP produced with 100 μg/ml template CT is shown in red. Rebinding of CT on a CT MIP fabricated with 1 μg/ml template CT is shown in black. The NIP control is shown in blue; the same CT concentrations are exposed to the NIP in order to assess non-specific binding. Both CT MIPs represent two trials on the same device whereas the NIP data represents on trial. Error bar shown is standard deviation.

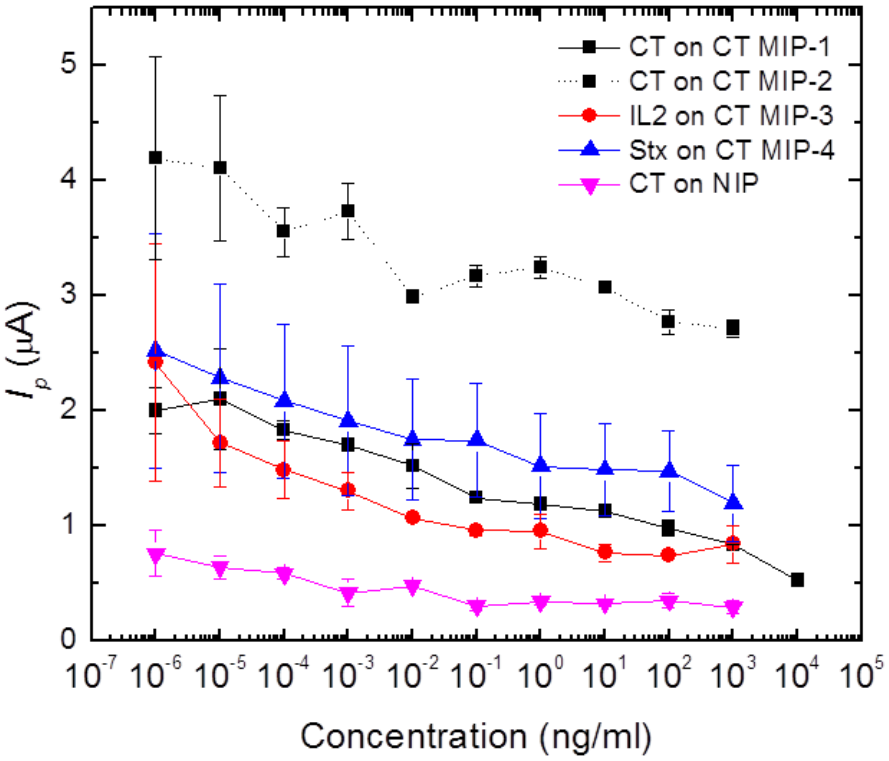

Figure A.5. Rebinding of proteins on CT MIP devices. Four CT MIP devices were fabricated (CT MIP-1, -2, -3, -4) as well as a NIP control. Protein samples of varying concentrations were added to each device and the current was recorded. On the y-axis, the peak current is plotted against the protein concentration added. CT was rebound on two of the MIP devices: CT MIP-1 (black; solid line) and CT MIP-2 (black; dashed line). IL2 was added to CT MIP-3 (red) and Stx was added to CT MIP-4 (blue) to examine non-specific binding of non-template protein on the imprint. CT was additionally added to the NIP control sample (magenta) to examine non-specific binding of protein on polymer without imprints. Each data set represents two trials. Error bar shown is standard deviation. X-axis: concentration (ng/ml); y-axis: peak current (I_p).

References

1. Verheyen, E. *et al.* Challenges for the effective molecular imprinting of proteins. *Biomaterials* **32,** 3008–20 (2011).

2. Chianella, I. *et al.* Direct replacement of antibodies with molecularly imprinted polymer nanoparticles in ELISA--development of a novel assay for vancomycin. *Anal. Chem.* **85,** 8462–8 (2013).

3. Vasapollo, G. *et al.* Molecularly imprinted polymers: present and future prospective. *Int. J. Mol. Sci.* **12,** 5908–45 (2011).

4. Cai, D., Ren, L., Zhao, H., Xu, C. & Zhang, L. A molecular-imprint nanosensor for ultrasensitive detection of proteins. *Nat. nanotechology* **5,** 597–601 (2010).

5. Rizal, B. Nanocoax arrays for sensing devices. 82–87 (2014).